

Electronic Thesis and Dissertation Repository

4-10-2012 12:00 AM

An Experimental Investigation on the Flow Behaviour in a Transpired Air Collector

David Greig
The University of Western Ontario

Supervisor
Dr. Kamran Siddiqui
The University of Western Ontario Joint Supervisor
Co-Supervisor Dr. Karava
The University of Western Ontario

Graduate Program in Mechanical and Materials Engineering
A thesis submitted in partial fulfillment of the requirements for the degree in Master of Engineering Science
© David Greig 2012

Follow this and additional works at: <https://ir.lib.uwo.ca/etd>



Part of the [Heat Transfer, Combustion Commons](#)

Recommended Citation

Greig, David, "An Experimental Investigation on the Flow Behaviour in a Transpired Air Collector" (2012). *Electronic Thesis and Dissertation Repository*. 434.
<https://ir.lib.uwo.ca/etd/434>

This Dissertation/Thesis is brought to you for free and open access by Scholarship@Western. It has been accepted for inclusion in Electronic Thesis and Dissertation Repository by an authorized administrator of Scholarship@Western. For more information, please contact wlsadmin@uwo.ca.

AN EXPERIMENTAL INVESTIGATION ON THE FLOW BEHAVIOUR IN A
TRANSPIRED AIR COLLECTOR

(Spine title: The Flow Behaviour in a Transpired Air Collector)

(Thesis format: Integrated Article)

by

David Greig

Graduate Program in Engineering Science,
Department of Mechanical and Materials Engineering

A thesis submitted in partial fulfillment
of the requirements for the degree of
Master of Engineering Science

The School of Graduate and Postdoctoral Studies
The University of Western Ontario
London, Ontario, Canada

© David Greig 2012

THE UNIVERSITY OF WESTERN ONTARIO
School of Graduate and Postdoctoral Studies

CERTIFICATE OF EXAMINATION

Co-Supervisor

Dr. Kamran Siddiqui

Co-Supervisor

Dr. Panagiota Karava

Supervisory Committee

Dr. Anthony G. Straatman

Examiners

Dr. Eric Savory

Dr. Jun Yang

Dr. Gregory Kopp

The thesis by

David Greig

entitled:

**An Experimental Investigation on the Flow Behaviour in a Transpired Air
Collector**

is accepted in partial fulfillment of the
requirements for the degree of
Master of Engineering Science

Date

Chair of the Thesis Examination Board

Abstract

An experimental investigation of the flow dynamics in a transpired air collector channel with a corrugated surface is presented. Particle image velocimetry (PIV) was used to obtain two-dimensional velocity fields to compare the effects of surface heating on the flow for five flow rates. Mean velocity and turbulent property profiles are presented and compared. Proper orthogonal decomposition and wavenumber spectrum analyses were also conducted to investigate the underlying interactions between the turbulent structures that comprise the complex flow behaviour observed in corrugated flows. Results show that the corrugated waveform was the primary source of turbulence at all flow rates and heating conditions, which produced enhanced turbulent properties in its vicinity. However, under an applied heat flux, the flow at the lowest flow rate the flow was primarily buoyancy driven, where buoyancy induced stabilities and heating effects were strongest.

Keywords

Particle Image Velocimetry (PIV), turbulent channel flow, corrugated surface, solar air collector, proper orthogonal decomposition, spectral analysis.

Co-Authorship Statement

I hereby declare co-authorship in the following chapters:

Chapter 2 is the journal article submitted and in review by the International Journal of Heat and Fluid Flow. The complete reference is D. Greig, K. Siddiqui, and P. Karava, An experimental investigation of the flow structure over a corrugated waveform in a transpired air collector, Int. J. Heat and Fluid Flow (2012), Unpublished results.

Chapter 3 is the journal article submitted and in review by the International Journal of Heat and Mass Transfer. The complete reference is D. Greig, K. Siddiqui, and P. Karava, The influence of surface heating on the flow dynamics within a transpired air collector, Int. J. Heat and Mass Transfer (2012), Unpublished results.

Chapter 4 will be submitted for publication under the co-authorship of D. Greig, K. Siddiqui, and P. Karava.

Acknowledgements

I would like to extend my thanks and gratitude to my supervisors and friends Kamran Siddiqui and Panagiota Karava for their insight and assistance, and for providing me with opportunities to expand my experiences from the University of Western Ontario. Furthermore, I would like to thank my co-workers who have offered their wisdom and assistance in the early stages of my project.

Table of Contents

Certificate of Examination.....	ii
Abstract.....	iii
Co-Authorship Statement.....	iv
Acknowledgments.....	v
Table of Contents.....	vi
List of Tables.....	ix
List of Figures.....	x
Chapter 1: Introduction	1
1.1 Introduction.....	1
1.2 Motivation.....	4
1.3 Objectives	4
1.4 Thesis Layout.....	5
1.5 References.....	6
Chapter 2: An experimental investigation of the flow structure over a corrugated waveform in a transpired air collector.....	7
2.1 Abstract.....	7
2.2 Introduction.....	8
2.3 Experimental Setup.....	11
2.4 Results.....	16
2.5 Discussion.....	24

2.6 Conclusion	31
2.7 Acknowledgements.....	33
2.8 References.....	33
2.9 Figures.....	35
Chapter 3: The influence of surface heating on the flow dynamics within a transpired air collector.....	52
3.1 Abstract.....	52
3.2 Introduction.....	53
3.3 Experimental Setup.....	57
3.4 Results.....	62
3.5 Discussion.....	71
3.6 Conclusion	79
3.7 Acknowledgements.....	80
3.8 References.....	80
3.9 Tables	83
3.10 Figures.....	84
Chapter 4: Investigation of fundamental flow mechanisms over a corrugated waveform using properorthogonal decomposition and spectral analyses	103
4.1 Abstract.....	103
4.2 Introduction.....	104
4.3 Experimental Setup.....	106

4.3.1 Proper Orthogonal Decomposition Scheme.....	108
4.4 Results and Discussion	109
4.4.2 Proper Orthogonal Decomposition (POD) Analysis	109
4.4.1 Spectral Analysis.....	116
4.5 Conclusions.....	120
4.6 Acknowledgements.....	121
4.7 References.....	121
4.8 Figures.....	123
Chapter 5: Conclusions	141
5.1 Discussion Summary and Conclusion	141
5.2 Significance of Findings	145
5.3 Future Recommendation.....	146
APPENDIX 1: PIV Error Calculation	148
Curriculum Vitae	151

List of Tables

Table 3-1: Position and time averaged temperatures for the solar wall system in degrees Celsius.....	83
Table 3-2. Calculated heat transfer values within the solar wall system.....	83

List of Figures

2-1: Schematic of the experimental setup.....	36
2-2: Snapshots of instantaneous velocity fields at the middle channel height ($X/L = 0.57$) in (a) the trough section; (b) the crest section, at $Re = 2675$. \square = corrugation wavelength; h = corrugation wave height. The resolution of the velocity field is reduced in the plots for the better illustration of the flow dynamics.....	37
2-3: Snapshots of the turbulent velocity vector fields at various locations along the channel at different Reynolds numbers. (a) The crest section at $X/L = 0.57$, $Re = 2675$; (b) the trough section at $X/L = 0.18$, $Re = 4140$; (c) the trough section at $X/L = 0.57$, $Re = 4140$. The resolution of the velocity field is reduced in the plots for the better illustration of the flow dynamics.....	39
2-4: Mean velocity profiles at various locations over the corrugation waveform normalized by the bulk velocity (U_B); (a) at the middle height of the channel ($X/L = 0.57$) at various Reynolds numbers. (Δ), $Re = 530$; (\circ), $Re = 2030$; (\square), $Re = 2675$; (\diamond) $Re = 4140$; (\times), $Re = 6650$. (b) At various heights along the channel length for $Re = 2675$. (Δ), $X/L = 0.18$; (\circ), $X/L = 0.57$; (\square), $X/L = 0.8$	42
2-5: Profiles of the RMS streamwise turbulent velocity at various locations over the corrugation waveform normalized by U_B ; (a) at the middle height of the channel ($X/L = 0.57$) at various Reynolds numbers. (Δ), $Re = 530$; (\circ), $Re = 2030$; (\square), $Re = 2675$; (\diamond) $Re = 4140$; (\times), $Re = 6650$. (b) At various heights along the channel length for $Re = 2675$. (Δ), $X/L = 0.18$; (\circ), $X/L = 0.57$; (\square), $X/L = 0.8$	44
2-6: Profiles of the RMS cross-stream turbulent velocity at various locations over the corrugation waveform normalized by U_B ; (a) at the middle height of the channel ($X/L = 0.57$) at various Reynolds numbers. (Δ), $Re = 530$; (\circ), $Re = 2030$; (\square), $Re = 2675$; (\diamond) $Re = 4140$; (\times), $Re = 6650$. (b) At various heights along the channel length for $Re = 2675$. (Δ), $X/L = 0.18$; (\circ), $X/L = 0.57$; (\square), $X/L = 0.8$	46
2-7: Profiles of Reynolds Stress ($-\overline{u'v'}$) at various locations over the corrugation form normalized by U_B ; (a) at the middle height of the channel ($X/L = 0.57$) at various Reynolds numbers. (Δ), $Re = 530$; (\circ), $Re = 2030$; (\square), $Re = 2675$; (\diamond) $Re = 4140$; (\times),	

	Re = 6650. (b) At various heights along the channel length for Re = 2675. (Δ), $X/L = 0.18$; (\circ), $X/L = 0.57$; (\square), $X/L = 0.8$	48
2-8:	Profiles of the turbulent kinetic energy production (P) normalized by U_B and the channel height H ; (a) at the middle height of the channel ($X/L = 0.57$) at various Reynolds numbers. (Δ), Re = 530; (\circ), Re = 2030; (\square), Re = 2675; (\diamond) Re = 4140; (\times), Re = 6650. (b) At various heights along the channel length for Re = 2675. (Δ), $X/L = 0.18$; (\circ), $X/L = 0.57$; (\square), $X/L = 0.8$	50
3-1:	Schematic of experimental setup.....	84
3-2:	Turbulent velocity vector fields with reduced resolution at the middle section of the channel ($X/L = 0.57$) at the lowest flow rate (Case I) for the high heating condition (a) over the trough section; (b) over the crest section.....	85
3-3:	Mean velocity profiles at over the corrugation waveform at the middle height of the channel ($X/L = 0.57$) (a) at various flow rates normalized by the bulk velocity (U_B) at the high heating condition (Δ), Case I; (\circ), Case II; (\square), Case III; (\diamond) Case IV; (\times), Case V; (b) comparing profiles for different heat conditions at the lowest flow rate (Case I), (Δ), unheated; (\circ), low heating $q_{in} = 530W$; (\square), high heating $q_{in} = 793W$; (c) comparing profiles for different heat conditions at the highest flow rate (Case V), (Δ), unheated; (\circ), low heating $q_{in} = 530W$; (\square), high heating $q_{in} = 793W$	87
3-4:	Profiles of the streamwise (u) RMS turbulent velocity over the corrugation waveform the middle height of the channel ($X/L = 0.57$), (a) at various flow rates normalized by U_B (Δ), Case I; (\circ), Case II; (\square), Case III; (\diamond) Case IV; (\times), Case V; (b) comparing profiles for different heat conditions at the lowest flow rate (Case I), (Δ), unheated; (\circ), low heating $q_{in} = 530W$; (\square), high heating $q_{in} = 793W$; (c) comparing profiles for different heat conditions at the highest flow rate (Case V), (Δ), unheated; (\circ), low heating $q_{in} = 530W$; (\square), high heating $q_{in} = 793W$	91

3-5: Profiles of the cross-stream (v) RMS turbulent velocity over the corrugation waveform the middle height of the channel ($X/L = 0.57$), (a) at various flow rates normalized by U_B (Δ), Case I; (\circ), Case II; (\square), Case III; (\diamond) Case IV; (\times), Case V; (b) comparing profiles for different heat conditions at the lowest flow rate (Case I), (Δ), unheated; (\circ), low heating $q_{in} = 530W$; (\square), high heating $q_{in} = 793W$; (c) comparing profiles for different heat conditions at the highest flow rate (Case V), (Δ), unheated; (\circ), low heating $q_{in} = 530W$; (\square), high heating $q_{in} = 793W$95

3-6: Profiles of the Reynolds stress ($-\overline{u'v'}$) over the corrugation waveform the middle height of the channel ($X/L = 0.57$), (a) at various flow rates normalized by U_B (Δ), Case I; (\circ), Case II; (\square), Case III; (\diamond) Case IV; (\times), Case V; (b) comparing profiles for different heat conditions at the lowest flow rate (Case I), (Δ), unheated; (\circ), low heating $q_{in} = 530W$; (\square), high heating $q_{in} = 793W$; (c) comparing profiles for different heat conditions at the highest flow rate (Case V), (Δ), unheated; (\circ), low heating $q_{in} = 530W$; (\square), high heating $q_{in} = 793W$99

4-1 Schematic of setup.....122

4-2 a) Turbulent velocity vector field of frame 47 at the crest in the middle of the channel ($X/H = 0.57$) at half resolution to clearly visualize the directions of the vectors at higher quality; b) Reconstructed POD energy vector field up to mode 47 at the crest in the middle of the channel ($X/H = 0.57$) at half resolution to clearly visualize the directions of the vectors at higher quality.....124

4-3 POD fractional energy (λ_n/E) distribution across all modes for the lowest flow rate, unheated (Green \blacktriangle); highest flow rate, unheated (Black \bullet); highest flow rate, heated (Blue \bullet); and lowest flow rate, heated (Red \blacktriangle) cases.....126

4-4	POD crest turbulent flow energy vector fields at the middle of the channel ($X/H = 0.57$) for the highest flow rate at a) mode 1, half vector resolution; b) mode 5, half vector resolution c) mode 10, half vector resolution d) mode 20, half vector resolution, e) mode 50, full vector resolution f) mode 80, full vector resolution g) mode 150, full vector resolution.	130
4-5	POD turbulent flow energy vector fields at the middle of the channel ($X/H = 0.57$) for the highest flow rate at mode 25 using full vector resolution in the a) trough section; b) crest section.....	131
4-6	POD turbulent flow energy vector fields comparing heat and no heat at the middle of the channel ($X/H = 0.57$) at the highest flow rate; a) POD mode 12 for the unheated condition; b) POD mode 12 for the heated condition; c) POD mode 70 for the unheated condition; d) POD mode 70 for the heated condition.....	133
4-7	POD turbulent flow energy vector fields comparing heat and no heat at the middle of the channel ($X/H = 0.57$) at the lowest flow rate; a) mode 15, unheated; b) mode 15, heated; c) mode 78, unheated; d) mode 78, heated.....	136
4-8	Wave number spectrum plots for the development of energy across a waveform located in the middle of the channel ($X/H = 0.57$) over the crest for the unheated condition a) at the lowest flow rate; b) at the highest flow rate.....	136
4-9	Wave number spectrum plots comparing the energy transfer located in the middle of the channel ($X/H = 0.57$) for the low and high flow rates at both heated and unheated conditions; a) streamwise energies located over the crest section; b) streamwise energies over the trough section; c) cross-stream energies located over the crest section; d) cross-stream energies located over the trough section.....	139

Chapter 1

1.1 Introduction

A study conducted by the International Energy Agency (IEA) shows that there was a 23% increase in global energy use between the years of 1990 and 2005 [1]. And recent estimates state the global energy demand is expected further increase by 35% between the years 2008 and 2035 [1]. In cold climates like Canada, heating requires a significant portion of the total energy demand for a large part of the year. According to National Resources Canada (NRCAN), as of 2008 the average commercial building consumes about 50% of its total heating requirement on space heating, which is primarily supplied through fossil fuels. Due to the limited reserves of conventional fossil fuels and their harmful effects on the environment, it is crucial to explore renewable energy alternatives to meet this growing energy demand. Solar energy has been found to have the largest potential among these systems to meet the global energy demand for generations to come. The sun is the largest known energy source that is available to the world. It has been estimated that the amount of solar irradiation incident on the earth in one year is approximately 15 000 times the world's total energy use [2]. The major difficulty has been to find an effective means of extracting the energy in a useable form. It is considered most economical to use the sun's energy directly as heat where a temperature increase is desired. This can be accomplished by implementing an emerging technology known as a transpired air collector or passive solar collector. This is a unique type of corrugated and perforated sheet metal installed in front of a building to absorb incident sunlight and preheat the incoming air for spatial heating. The sheet is designed to be as close to a blackbody as possible with a high thermal conductivity. By installing the transpired air collector in front of a building façade, an approximately two dimensional channel is created for ambient air to flow. Incident solar

radiation on the collector is transferred to the air in the channel that is then drawn into the building Heating Ventilation and Air Conditioning (HVAC) system to reduce the total load required to heat spatial supply air. Although solar energy technologies for water heating have been developed and commercialized, renewable energy technologies for space heating are not well recognized. The air can be driven either by forced or natural convection. Advantages of using a transpired air collector include its relatively low installation cost, and minimal energy required to run the system if forced convection is used. They can be installed on both commercial and residential buildings and could be included in the new design and construction, or retrofitted onto an existing façade. The benefits of fuel and monetary savings outweigh the energy cost of creating and operating the solar wall system, and these savings increase with the size of the solar collector.

Piao [3] has shown that for corrugated solar air collector systems under natural convection, heat transfer is larger for smaller channel depths contrary to smooth channels because of strong wall interactions. It was also reported that mixed convection systems of natural and forced air flows produce marginally increased convection heat transfer. However, the local heat transfer coefficient generally varies in the direction of the flow and is evident to be periodic along the sinusoidal corrugated waveform [3].

Corrugated surfaces are widely used in heat transfer systems as a passive means to enhance heat transfer by increasing the surface area and mixing. Not only is the corrugation geometry of the transpired air collector unconventional, but the presence of slit perforations creates a unique form of surface roughness resulting in a complex flow structure. There are two general flow regimes for the air flow over a corrugated surface in a two dimensional channel: the bulk flow above the corrugation height, and the local flow within the corrugation trough. The bulk flow separates off

each crest, creating a region of low velocity in the corrugation troughs. The interaction between these two flow regimes creates a shear layer where vortices are generated [4, 5]. However, in a heated channel, there are thermal plumes of accelerated parcels of air near the heated surface. The interface between the heated and unheated flows creates a shear layer and rolls of vortices are produced. Inside the solar air collector channel, there is a combination of both the affects of the flow over a wavy surface, as well as a heated flow in a duct. There have been no recorded studies on the interactions between these flows in a transpired air collector and it is important to determine these characteristics in order to determine the optimal configurations to maximize heat transfer from the heated collector to the air.

Studies have reported many thermal performance ranges for different types of collectors and their configuration. The manufacturer technical specifications for a cross-corrugated solar collector gives a maximum thermal efficiency of 75% for the largest flow rate, while field tests for the same system provide efficiencies of 50% [6]. Natural convection in a flat plate solar air collector produced maximum thermal efficiencies between 50% and 60% [7]. Leon and Kumar [8] mathematically modelled the forced heat transfer characteristics for a perforated flat plate collector and determined it is desirable to have low emissivity and high absorptivity solar collectors and obtained maximum collector efficiencies of approximately 75%. Njomo and Dagenet [9] numerically model and simulate the heat transfer in 4 different horizontal flat plate solar air collectors for a vast amount of parameters. A variety of maximum thermal efficiencies were obtained depending on variables such as flow rate, gap depth, and irradiance.

1.2 Motivation

Currently, there are no standardized design methods for installing the transpired air collector. Each new development is based on the experience gained from previous projects and reports. The solar collector system has yet to be optimized in areas such as air gap thickness, collector material and porosity, corrugation geometry, and air flow rate. The studies show that not only are there many different types of collectors commercially available each with different methods for installation, but that there is a primary focus on thermal efficiencies both experimentally and numerically. Furthermore, there are inconsistencies on the thermal efficiencies that can be obtained by some of these systems. There have been very few studies that investigate the basic air flow within these systems.

The performance of a transpired air collector predominantly relies on the airflow behaviour in the channel, which in turn influences the heat transfer from the corrugated wall. Therefore, it is important to understand not only the dynamics of the flow over the corrugation waveform, but the underlying physical processes as well, in order to improve heat transfer from the corrugated surface.

1.3 Objectives

The objectives of this research is to:

- I. Characterize the turbulent flow of air within the unheated and heated transpired solar air collector for various flow rates.
- II. Explore the underlying physical processes and interactions of turbulence within the solar air collector channel.

The scope of this study focuses on improving the understanding of the thermo-fluid interactions in the transpired air collector channel. A full-scale transpired air collector experimental system was constructed in a laboratory environment to conduct experiments to determine the mean and turbulent air flow structures and interactions. Detailed two-dimensional instantaneous velocities were obtained using Particle Image Velocimetry (PIV). These results are beneficial for current commercial solar collector installations as well as for general air heat transfer systems employing a corrugated surface. The end goal is to develop methods that will encourage heat transfer from the collector to the air in order to maximize the system efficiency to help meet the future energy demand.

1.4 Thesis Layout

The first chapter introduced the need for alternative energy systems to be developed and the gaps within current reports on the development of solar air collectors. The purpose and objectives for the present report were given. The second chapter focuses on the fundamental air flow behaviour within a transpired air collector across laminar to turbulent Reynolds numbers without any heating in order to establish a control case. The third chapter compares the mean and turbulent properties of a heated and unheated flow in the transpired air collector and factors that lead to enhanced heat transfer. The thermal efficiencies were also determined. The fourth chapter of the thesis is an in depth analysis of the underlying physical interactions of the heated and unheated flows using Proper Orthogonal Decomposition (POD) and a Wavenumber Spectrum analysis. These techniques will contribute to the understanding of the associated energies and transfer between turbulent structures such as vortices. The final chapter brings the key conclusions from each of the preceding chapters together to create a better understanding on the factors that affect the heat transfer within the solar air heater.

1.5 References

- [1] Organisation for Economic Co-operation and Development/International Energy Association. 2011. World Energy Outlook 2011.
- [2] Berman, A., Karn, R.K., and Epstein, M. 2006. A New Catalyst System for High-Temperature Solar Reforming of Methane. *Energy Fuels* 20 (2). 455–462.
- [3] Paio, Y. 1992. Natural, forced and mixed convection in a vertical cross-corrugated channel, Master's thesis, Faculty of Mechanical Engineering, University of British Columbia.
- [4] Breuer, M., Peller, N., Rapp, Ch., and Manhart, M. 2009. Flow over periodic hills – Numerical and experimental study in a wide range of Reynolds numbers. *Computers and Fluids* 38, 433-457.
- [5] Kuzan, J. D., Hanratty T. J., and Adrian, R. J. 1989. Turbulent flows with incipient separation over solid waves. *Exp Fluids* 7, 88-98.
- [6] Athienitis, A.K., Bambara, J., O'Neill, B. Faille, J. 2011. A prototype photovoltaic/thermal system integrated with transpired collector. *Solar Energy* 85. 139–153
- [7] Hatami, N. and Bahadorinejad, M. 2008. Experimental determination of natural convection heat transfer coefficient in a vertical flat-plate solar air heater. *Solar Energy* 82. 903–910
- [8] Augustus Leon, M.A. and Kumar, S. 2007. Mathematical modeling and thermal performance analysis of unglazed transpired solar collectors. *Solar Energy* 81. 62–75
- [9] Njomo, D. and Daguinet, M. 2006. Sensitivity analysis of thermal performances of flat plate solar air heaters. *Heat Mass Transfer* 42. 1065–1081

Chapter 2

An experimental investigation of the flow structure over a corrugated waveform in a transpired air collector

2.1 Abstract

An experimental investigation of the flow dynamics in a channel with a corrugated surface is presented. Particle image velocimetry was used to obtain two-dimensional velocity fields at three different locations along the channel length, over a range of Reynolds numbers. The results show a significant impact on the corrugation waveform with regards to the mean and turbulent flow structure inside the channel. Vortex shedding off the crests combined with rolls from the shear layer were observed. Their interactions created a complex three-dimensional flow structure extended over almost the entire channel. The mean velocity profiles indicate a strong diffusion of shear. The profiles of various turbulent properties show the enhancement of turbulence in the vicinity of the waveform. It was found that the turbulence in the channel was almost entirely produced in this region above the corrugation trough. Significant momentum transfer from the corrugation wall by the turbulent velocity field was also observed. The mean and turbulent flow behaviour was found to be periodic with respect to the waveform over most of the channel length. The results show the presence of strong turbulence even at the Reynolds number that falls within the conventional laminar range for duct flows.

2.2. Introduction

Corrugated surfaces are widely used in heat transfer systems as passive means to increase heat transfer by increasing the surface area and mixing. Recently a new application with a corrugated metal plate used as a solar collector, also known as *transpired solar wall*, has begun to emerge. The basic function of the solar wall is to preheat the ambient air to reduce the heating load of conventional Heating, Ventilating and Air Conditioning (HVAC) systems during winter months. Its simple design concept includes the installation of a corrugated metal plate with rough slit perforations in front of the façade of a building to create a channel for ambient air to flow through. The solar wall is heated up by absorbing the sunlight and this heat is transferred to the ambient air as it flows through an approximately two-dimensional channel bounded by the corrugated solar wall and the smooth construction wall. Not only is the corrugation geometry unconventional, but the presence of slit perforations creates a unique form of surface roughness, resulting in a complex flow structure. When the air flows over a corrugated surface in a two dimensional channel it experiences flow separation over the crest of the corrugation and reattachment in the trough region [1-3]. There are two primary flow regimes; the bulk flow above the corrugation height, and the local flow within the corrugation trough. The interaction between these two flow regimes creates a complex three-dimensional flow.

The performance of a solar wall depends largely on the airflow behaviour in the channel, which in turn influences the heat transfer from the corrugated wall. Therefore, it is important to understand the physical behaviour of the flow over the corrugation waveform in particular and within the channel in general, in order to improve heat transfer from the corrugated surface.

Traditionally, in turbulent channel flows, the peak magnitudes of turbulent properties are observed in the near-wall regions, while the mean streamwise velocity peaks at the centre of the channel [4-5]. Changing the surface roughness for these channel flows has been found to have a strong influence on the turbulent properties [6]. A number of studies focused on the turbulent behaviour in channel flows with different types of surface geometries either on one or opposing channel walls. A common observation in these studies was deviating trends of flow behaviour from that of the conventional flat channel flows, in which the maximum mean velocity was shifted towards the flat wall. The common types of corrugated geometries previously investigated were continuous sinusoidal waves [3,7-11], saw-tooth (V corrugations) [12], and square-wave [13].

Breuer *et al.*[1] conducted a numerical and experimental study to understand the flow behaviour over a series of hills for a range of Reynolds numbers. They observed that the flow changes from steady and two-dimensional to three-dimensional even at relatively low Reynolds number. They also found that the flow separates off the top of a hill and reattached on the windward side of the following hill. The reattachment point varied non-monotonously as a function of Reynolds number, which was attributed to the recirculation on the windward side. Several studies investigated the flow over sinusoidal waves in turbulent channel flows [1-3,8-10]. A common observation in all these studies was the enhancement of turbulent properties in the separation region above troughs. Furthermore, the peak magnitudes of turbulent properties were typically observed over the trough at the distance approximately equal to the wave height.

Hudson *et al.*[9] reported the turbulent properties over sinusoidal waves. In addition to the above observations they also concluded that the mechanism of turbulent kinetic energy production above a wavy surface is different from that above a flat wall. They showed that the

turbulent kinetic energy is primarily produced along the streamline of the detached shear layer and expands downstream half way into both the trough and bulk flow. They proposed that the large streamwise fluctuations in the separation region over the trough create turbulent structures that increase cross stream fluctuations slightly downstream. Kruse *et al.*[10] studied the turbulent flow behaviour over sinusoidal waves in a channel flow using particle image velocimetry (PIV). Three different amplitude-to-wavelength ratios were considered in their study. They concluded that the surface roughness does not have a significant impact on Reynolds stress and energy production at a reasonable distance (approximately one wavelength) from the wall. They also observed asymmetry in the mean velocity profiles where the location of the maximum mean velocity shifted towards the plane wall. Shaikh and Siddiqui [3] investigated the impact of surface configuration on the turbulent flow characteristics using PIV. They considered smooth and wavy solid and water surfaces and found that the turbulent behaviour over water and solid surfaces is similar, however, the magnitude was dependent on the surface type. They also reported that the water surface yielded the largest normalized magnitudes of turbulent properties while, the sinusoidal solid surface yielded the smallest magnitudes. For the flow over the solid sinusoidal waves, the turbulent flow behaviour was similar that observed by other studies [9,10]. Nakagawa and Hanratty [11] used PIV to study the turbulence behaviour above a low-amplitude sinusoidal surface and found that the Reynolds stresses were strongly affected by large velocity structures that were as large as half the channel height.

Yang and Chen [12] performed a detailed numerical study on the heat transfer process in a channel flow between two sawtooth corrugated surfaces by changing the corrugation angle at various Reynolds numbers. They observed that an increase in the corrugation angle produced

more fluid recirculation in the corrugation troughs and with a higher Nusselt number. Stel et al. [13] investigated the flow over square wave corrugations in a pipe flow with the specific focus on the impact of wavelength on flow losses, turbulent kinetic energy and Reynolds stress. They observed that the turbulence and the momentum exchange between the local and bulk flows increased with the wavelength and Reynolds number, and the peak turbulent kinetic energy was located above the reattachment point on the windward crest corner of the square wave.

As the literature review shows, there are limited studies on different types of simple corrugations. To the best of our knowledge, there is no reported work in the literature investigating the flow dynamics in the presence of the complex corrugation and surface roughness as in the transpired air collector. This complex surface configuration also makes this problem unique from fluid dynamical perspective. We have conducted a detailed experimental study to characterize the flow behaviour over this corrugated geometry for a range of Reynolds numbers. The outcome will not only further advance the development of transpired solar air collectors to make the technology more efficient but also contributes to the fundamental fluid dynamics research.

2.3 Experimental Setup

Experiments were conducted in a laboratory setting. A construction wall using the same standards as for a residential house was built with dimensions 1.83 m long, 1.22 m wide and 0.1 m deep. A 1.3 cm thick plywood board was fixed to one face of the construction wall, and a 1 cm drywall was attached to the opposite face with hinges, enabling access to inside the construction wall. The corrugated and perforated solar collector 1.83 m \times 1.22 m in size was made of 18 gauge sheet metal. The material and geometry of the collector is the same as that used in real transpired air collector applications. The corrugation amplitude and wavelength (λ)

are 3.5 cm and 15 cm, respectively. The surface of the sheet has triangular shaped (1.4 mm amplitude) perforations spaced 2.2 cm apart from the centre (approximately 1.5% porosity). This transpired collector was mounted across the construction wall to create a channel. The height of the channel (H) based on the distance from the mean corrugation height to the construction wall is 10.95 cm. The length of the channel (L) is 1.83 m (see Fig 2-1). The channel was sealed with Plexiglas sheets to allow optical access for measurement. The complete assembly was attached to a modular frame of dexion metal square tubing. This allowed the system to be flexible for changes in inclination angle and channel height positioning for future experiments. The air flow through the channel was from the bottom to the top in the suction mode drawn by a 3hp centrifugal fan (New York Blower Company). The flow rate of the fan was controlled by a variable frequency drive.

Two dimensional instantaneous velocity fields over a complete waveform were obtained using Particle Imaging Velocimetry (PIV) at three locations along the channel length, $X/L = 0.18, 0.57, 0.80$, where X is measured from the inlet of the channel (see Fig 2-1). In order to keep high resolution of the velocity field, measurements in the crest and following trough regions were taken separately. The crest region was defined as the region bounded between $x/\lambda = 0$ and 0.5 , while the trough region was bounded between $x/\lambda = 0.5$ and 1.0 , where, x is measured from the base of the windward face of the corrugation (see inset in Fig 2-1). The camera field of view was set in a way that there was an overlap of the measurement domain in the crest and trough sections to ensure that no location along the corrugation waveform was missed. The overlap region covered about 20% of the waveform (see inset in Fig 2-1). For each position, measurements were taken in the mid cross plane. For each experimental run, the data were collected 30 minutes after setting the desired flow rate allowing the flow to reach steady state.

The PIV system comprised of a 120 mJ Nd:YAG laser (SoloPIV 120XT) as the light source. A 1 cm slot was cut along the length of the construction wall and fitted with Plexiglas strips on both sides of the construction wall to allow optical access for the laser light sheet to reach measurement locations. A four megapixel CCD camera (Flare, IO Industries) with the resolution of 2336×1752 pixels was used to image the flow. The camera was mounted horizontally viewing the measurement plane from the Plexiglas wall on the side of the channel (see figure 2-1) i.e. 2336 pixels in horizontal and 1752 pixels in vertical. The field of view of the camera was about $15.3 \text{ cm} \times 11.5 \text{ cm}$. Eight-bit images were acquired using an image acquisition system (CoreView, IO Industries) at a rate of 30 Hz. A four channel delay generator synchronized with the camera was used to control the timing of the laser pulses.

Olive oil droplets with an average diameter of $1 \mu\text{m}$ were used as the tracer particles for the PIV measurements. The particles were introduced via a LaVision flow seeder using pressurized air. The homogeneous distribution of tracer particles is very crucial for the flow velocity computation using PIV. To generate homogeneous particle distribution in the flow, a 1-1/2 inch PVC pipe 110 cm in length was used as the particle distributor. Both ends of the pipe were sealed and 8 holes 0.5 cm in diameter were drilled alternating on a line drawn across its length. The pipe was placed inside a cylindrical plenum with the holes facing down to decay particle velocity. That is, the particles were drawn into the channel due to the fan suction. It also ensured an evenly distributed seed particles and well mixed with air before entering the channel. The cylindrical plenum was located 5 cm underneath the channel inlet (see Fig 2-1).

At each measurement location (i.e. crest and trough positions at each height), data were collected for five flow rates. For each case, 3000 images were acquired, which provided 1500 velocity fields. It was observed that the difference in the bulk mean streamwise velocities between the

top and middle sections was almost negligible, while the values of the bulk mean streamwise velocity at the bottom section were lower than that at the middle and the top sections. As will be discussed later, the inlet conditions were responsible for this difference. Hence, the bulk mean streamwise velocity in the middle section ($X/L = 0.57$) was considered as the reference velocity scale (U_B). The Reynolds number was defined based on U_B and the channel height (H). The Reynolds numbers corresponding to the five flow rates were 530, 2030, 2675, 4140, and 6650.

Images were captured with a small aperture setting to minimize the noise from the reflected light in the recordings. The image brightness and contrast was thus needed to be adjusted to improve the signal-to-noise ratio (SNR) to improve the accuracy of the velocity vector computation using PIV technique. It was noticed that the brightness was not uniform throughout the image but rather the regions near the construction wall were brighter than the rest of the image due to the laser light reflection. Therefore, the rescaling of the gray values by a constant factor to improve the SNR in the bulk image would result in an almost white background near the construction wall and hence, reliable velocity vectors could not be computed in that region. Thus, to overcome this issue, a novel approach was used to improve the SNR throughout the image. In this approach, the gray values were rescaled by a constant factor in the region away from the construction wall, while in the near construction wall region, the rescaling factor was linearly decreased to zero at the wall. This allowed an improved and almost uniform contrast between the particles and the background.

The PIV velocity fields were calculated by cross-correlating interrogation windows (48×48 pixels in size) in the first image of an image pair, with the corresponding search windows (96×96 pixels in size) in the second image of the image pair. A 50% overlap of interrogation windows was used, which provided a spatial resolution of 24×24 pixels, corresponding to a $1.6\text{mm} \times$

1.6mm spatial resolution of the velocity field. The erroneous velocity vectors were detected and corrected using a local median scheme based on the eight surrounding vectors [14]. It was noticed that in certain circumstances the above scheme could not detect and correct spurious velocity vectors. This corresponds to the situation where a group of spurious vectors exists within the flow domain. These vectors, if not eliminated, could bias the computed flow characteristics. Thus, a second scheme was developed to detect and eliminate these groups of bad vectors. Two criteria were set in this scheme to detect these vectors. The first criterion checks the deviation of each instantaneous velocity vector relative to the time averaged mean velocity at the same grid point, and removes that vector if the deviation is larger than a set percentage. The second criterion checks the direction of both components of the velocity vector relative to the global velocity direction and removes the vector if its angular deviation is larger than a set value. After their removal, the local median scheme was applied again to re-correct the good vectors that were affected by these spurious vector groups in the first correction scheme.

The total error in a PIV measurement is the sum of the errors from the seed particle diameter, seed density, velocity gradients, out of plane motion, the dynamic range, peak locking, and Adaptive Gaussian Window interpolation [15]. The uncertainty in the PIV velocity measurements was estimated based on the criteria and data presented in Cowen and Monismith [15] and Prasad *et al.*[16]. The uncertainty was computed at the highest flow rate as the errors are expected to be the largest in this case. The uncertainty in the PIV velocity measurements is estimated to be ± 0.22 cm/s which is less than 1% of the bulk flow velocity. Detailed error calculations are given in Appendix 1.

2.4 Results

To illustrate the general flow behaviour, instantaneous velocity fields in the trough and crest sections at the middle location ($X/L = 0.57$) are presented in Figure 2-2 at $Re = 2675$. For simplification, the trough region was defined as the sections between $y/h = 0$ and 1, where y is the lateral distance measured from the trough (see Fig 2-1). The plots show different features observed in the flow, in particular the effect of the waveform on the instantaneous flow behaviour. The bulk flow is relatively uniform, however the flow is dynamic in the trough region (see Figure 2-2a), which is due to the flow separation off the crest (see Figure 2-2b). The vortices generated by the flow separation appear to be advecting downstream and interacting with the bulk flow at $y/h \sim 1$. Figure 2-2a also shows multiple vortices present in the trough region. The low flow in the trough and bulk flow created a mixing layer (shear layer) which was one of the sources of vortex generation along the separation region. The flow separation seen in figure 2-2b was observed at all Reynolds numbers for all three measurement locations, which implies that every crest in the waveform induced flow separation. The current reports of a flow over a wavy surface describe the flow separating off the crest and reattaching on the windward side of the following crest (for example, see Shaikh and Siddiqui [3]). As mentioned earlier, in the present case, the vortices generated in the trough region due to the flow separation are dynamic. As a result, it was observed that the flow reattachment point is not at a fixed location on the windward side of the next crest but rather changes depending on the position of the advecting vortices in the trough relative to the windward face of the next crest similar to that observed by Breuer *et al.* [1] For example, in figure 2-2b, the reattachment point is visible at $y/h = 0.8$, as no vortex is present between $0.8 < y/h < 1$. A vortex in the trough region is visible in the plot. Whereas in figure 2-2a, no reattachment point on the windward face of the next crest is evident. This is due to the reason that the vortices in the trough blocked the bulk flow from

reaching the windward face of the next crest. The visual inspection of the instantaneous velocity fields has shown that due to this effect, the shear layer at the boundary of the bulk and separated flows oscillates in time, which in turn affects the size and strength of separation vortices. This oscillation also led to a stronger local interaction between the bulk and separated flows, and extends such interaction above the waveform height into the bulk flow region as evident in figure 2-2 in the region $1 < y/h < 1.5$. It also serves as an additional source of turbulence in the bulk flow region. It is observed that the mode of this oscillation varies with the flow rate. At low flow rates ($Re = 530$ and 2030) the bulk flow appears to be very uniform and the shear layer oscillates at a slower rate, resulting in a weak flow in the trough region with minimal interaction of the bulk and separated flows. The frequency and amplitude of shear layer oscillations increased with the Reynolds number resulting in a stronger bulk and separated flow interaction, which extends deeper into the bulk flow.

Turbulent velocities were computed by subtracting the time averaged mean velocity from the instantaneous velocity at each grid point. The visual inspection of turbulent velocity fields revealed the presence of very strong and dynamic turbulent flow. Three-dimensional effects were also observed in the flow. The data revealed very interesting and dynamical features in the turbulent flow which provide a deeper insight into the underlying physical processes. A representative set of turbulent velocity fields from different experimental runs is presented in figure 2-3 to illustrate these dynamical features. Figure 2-3a presents the turbulent velocity field corresponding to the instantaneous field shown in figure 2-2b. The plot shows a turbulent vortex on the leeward side of the crest. It also displays the interaction of the bursting flow from the trough and the sweeping flow from the bulk domain. In the present report, bursting is generalized as the turbulent motion of a fluid that is ejected away from a surface, while sweeping

is the movement of fluid towards a surface. The two flow regimes formed a diagonal line of interaction originating from the crest. Both the bursting and sweeping flows appear to accelerate in the core region of the bulk flow. Comparison of the instantaneous and turbulent velocity fields in figures 2-2b and 2-3a indicate that the line of interaction of the bursting and sweeping flows coincides with the shear layer. As the bursting and sweeping processes are intermittent¹⁷ it is likely that the oscillatory behaviour of the shear layer observed in the instantaneous velocity fields is due to the intermittent interaction of the bursting flow originating from the trough and the sweeping flow originating from the bulk flow region. An interesting feature observed in the plot is the presence of the spanwise turbulent velocity component. The flow structure at $y/h = 1$ and $x/\lambda = 0.13$ shows a flow source such that the flow is emerging from a source perpendicular to the measurement plane and dispersing in the measurement plane. This flow source is the spanwise turbulent velocity component indicating that the turbulent flow in the channel is three-dimensional. A vortex is also observed near this flow source which appears to be bursting from the construction wall.

Figure 2-3b also shows a similar three-dimensional pattern near the trough. Initial visual inspection of the data showed that the occurrence of the three-dimensional turbulent patterns is random. It is likely that these three-dimensional patterns are formed due to the complex interaction of separated and bulk flows that contain turbulent vortices, bursts and sweeps. The bursting of the flow from the trough is prominent in the figure. Another interesting feature is observed close to $y/h = 2.5$ and $x/\lambda = 0.5$. The flow seems to be going around a region centred at this location. As there is no physical obstruction that could cause such diversion, the plausible explanation for this effect is that the flow in this region has a strong spanwise velocity

component, which forces the flow in the perpendicular plane to go around it. Another such feature is observed at $y/h = 3$ and $x/\lambda = 0.8$ in figure 2-3b.

Another interesting feature highlighted in figure 2-3c is the shedding of turbulent vortices off the crest, which then advect into the bulk domain. The bursting is still visible from the trough region. In classical channel flows, the strongest turbulent motions are observed near the wall and the turbulence decays towards the channel core [4,5]. However, the turbulent velocity plots in figure 2-3 show that the strong bursting flow from the trough and the vortex shedding off the crest along with the three-dimensional interactions generated strong turbulent motions in the bulk region of the channel as well. The vortex shedding observed is referred to as the separation of vortices off the crest of the corrugation. A careful inspection of these plots also shows that the magnitude of turbulent velocity components in the bulk region is comparable to that observed within the waveform height. That is, the turbulence generated by the waveform is transported throughout the flow domain. This indicates the presence of strong turbulent momentum transfer.

Mean velocity field for each case was computed by time-averaging the instantaneous velocities at each grid point. The mean velocity fields in the crest and trough sections at a given position are superimposed to depict the mean velocity behaviour over the complete waveform of the corrugation. The mean velocity profiles at various axial locations (x/λ) along the corrugation waveform in the middle section of the channel ($X/L = 0.57$) are plotted in figure 2-4a at different Reynolds numbers. Note that velocities were normalized by the mean bulk axial velocity (U_B) since the friction velocity at the corrugation cannot be computed due to the large variation in the trends of the near-wall mean velocity profiles along the corrugation waveform, particularly in the trough region (see figure 2-4a) and experimental limitations to resolve the mean velocity gradients at the wall. Breuer *et al.* [1] have also used bulk velocity as the normalization

parameter for the flow over sinusoidal wavy surface. The plot shows a relatively uniform flow in the bulk region ($1.5 < y/h < 3.2$) with the mean velocities slightly increased towards the construction wall. This is likely due to the lesser drag and lower flow losses on the construction wall side compared the corrugation waveform side. The plot also shows that the mean velocity behaviour changed significantly as it approached the waveform, particularly in the trough region. The mean velocity magnitude started to decrease at $y/h \sim 1.5$ and reached almost negligible magnitude relative to the bulk flow. Mean velocities then decreased sharply after the leeward face, but slowly started to recover towards the windward side, although the mean velocity magnitude remained close to zero in the close vicinity of the corrugation in the trough section. The results also show that the profiles at all Reynolds numbers collapsed into a narrow band at all locations except at the lowest Reynolds number of 530. At this Reynolds number, the mean velocity magnitude relative to the bulk flow is lower in the region near the construction wall but higher in the trough region compared to that at all other Reynolds numbers. On average, the normalized mean velocities in the trough at this Reynolds number are 75% higher than that at other cases.

Figure 2-4b compares the mean velocities at different channel heights at $Re = 2675$. The mean velocity behaviour is almost identical at different locations along the entire waveform at the middle and top sections of the channel indicating that the flow is periodic over those sections of the channel, in other words, the flow structure and velocities repeat themselves over each complete waveform. At the bottom section, $X/L = 0.18$, the mean velocity behaviour in the bulk region was similar to that at the other heights. The reason the mean velocity at the bottom section does not completely collapse with the other data sets, is that the mean velocity magnitude in this section are lower than that at other heights. In the trough section, in the vicinity of $y/h = 1$,

the mean velocity in the bottom section is higher relative to the other heights. As will be discussed in the discussion section, the inlet effects are responsible for this deviation.

The calculation of turbulent velocity fields was described earlier. The root-mean-square (RMS) values of the streamwise and cross-stream components of the turbulent velocity were computed at each grid point. The profiles of the RMS streamwise turbulent velocities at different locations along the waveform of the corrugation in the middle section of the channel are presented in figure 2-5a at different Reynolds numbers. The plot shows that the streamwise turbulent intensity in general, was enhanced in the region $1 < y/h < 1.5$ but then decreased towards the bulk region and then slightly increased as it approached the construction wall. This trend is somewhat similar to that in a classical channel flow but the magnitudes of turbulent intensity are relatively high. This could likely be due to the turbulent enhancement by the corrugation which is then advected into the bulk region as observed in figure 2-3. In the trough region, the streamwise turbulent intensity decreased relatively fast up to $y/h \sim 0.75$ and then stayed almost constant with a very low magnitude. The decrease in the streamwise turbulent intensity in the region $0.75 < y/h < 1$ is sharpest at the location immediately downstream of the leeward face of the corrugation, which became gradual towards the windward face of the next crest. Comparison of the turbulent intensity profiles at different Reynolds numbers shows that except at the two lowest Reynolds numbers, the streamwise turbulent intensity profiles have similar behaviour. The turbulent intensity profiles at $Re = 2030$ showed a relatively higher magnitude in the bulk region above the crest while, higher turbulent intensity was observed at $Re = 530$ above the trough.

Figure 2-5b compares the RMS streamwise turbulent intensity profiles at the three channel heights at the Reynolds number of 2675. Similar to the observations in figure 2-4b, the

streamwise turbulent intensity profiles at the middle and top sections of the channel have comparable behaviour. At the bottom section, the turbulent intensity profiles show a relatively different behaviour. Above the crest, the turbulent intensity magnitude remained almost constant throughout the channel height, while above the trough, except very close to the trough base, the magnitude of turbulent intensity did not change significantly. Visual observations of the oil particle movement at the channel inlet indicated that the flow there was predominantly three-dimensional, therefore, the trends observed in this section could likely be due to inlet effects creating large flow three-dimensionality.

The profiles of the RMS cross-stream turbulent velocity component at different locations along the waveform of the corrugation in the middle section of the channel are presented in figure 2-6a at different Reynolds numbers. The plot shows in general, relatively high cross-stream turbulent intensity above the crest ($1 < y/h < 1.5$) which gradually decreased towards both boundaries. The magnitude of turbulent intensity is quite comparable at four higher Reynolds numbers. Deviations particularly in the trough region, are observed at the lowest Reynolds number (will be discussed later). The behaviour of the RMS cross-stream turbulent intensity at different channel heights is shown in figure 2-6b at $Re = 2675$. Similar to the streamwise turbulent intensity, the cross-stream turbulent intensity profiles show similar behaviour at the middle and top sections of the channel while a relatively uniform distribution of the cross-stream turbulent intensity across the channel width is observed at the bottom section. This is likely due to the three-dimensional behaviour of the flow at that section as mentioned earlier. Comparison of the streamwise and cross-stream turbulent intensity magnitudes (figures 2-5 and 2-6) show that overall the streamwise turbulent intensity is approximately 50% higher than the cross-stream turbulent

intensity. Whereas, the peak streamwise turbulent intensity is 70% higher than the peak cross-stream turbulent intensity.

The profiles of the Reynolds stress ($-\overline{u'v'}$) at the middle section of the channel along the waveform are presented in figure 2-7a at different Reynolds numbers. The plot shows that along the waveform, the Reynolds stress peaks between $y/h = 1$ and 1.5 for all Reynolds numbers and then decreases to zero towards the boundaries. The plot also shows that overall the Reynolds stress magnitude is significantly higher in the vicinity of the corrugation as compared to the construction wall. In fact, the Reynolds stress magnitude near the construction wall is almost negligible. The plot in figure 2-7a demonstrates that the turbulence produced by the corrugation dominates the entire channel. The results also show lower magnitudes of Reynolds stress at the lowest Reynolds number.

The Reynolds stress profiles at different sections along the channel length are shown in figure 2-7b. Similar to the previous results, the behaviour of the Reynolds stress at the middle and top sections is similar while in the bottom section, the Reynolds stress magnitude does not change significantly in the region $1 < y/h < 3.5$. In fact, no enhancement of Reynolds stress is observed above the crest in the bottom section. The enhancement of Reynolds stress is observed in the trough region, where the peak magnitude is comparable with that at the other heights. However, the location of the peak Reynolds stress changed with the axial distance from $y/h \sim 1$ at the leeward side of the corrugation to $y/h \sim 0.5$ at the windward side of the following corrugation. The reason for this trend could also be caused by inlet effects as mentioned earlier.

The rate of turbulent energy production was calculated using,

$$P = -\overline{u'v'} \frac{dU}{dy} \quad \text{Eq. 2.1}$$

where $-\overline{u'v'}$ is the Reynolds stress and $\frac{dU}{dy}$ is the mean velocity gradient [18]. The profiles of the rate of turbulent energy production (P) over the corrugation waveform at the middle section of the channel are shown in figure 2-8a at different Reynolds numbers. The plot shows that the energy production is mainly restricted to the region $0.75 < y/h < 1.5$. There is also a very small magnitude of energy production in the vicinity of the construction wall over a crest ($0 < x/\lambda < 0.5$) but it is almost negligible as compared to that in the vicinity of the corrugation. The comparison of the peak production at the corrugation wall and the construction wall shows that for all Reynolds numbers, the turbulence produced by the corrugation is about 10 orders of magnitude higher than that produced by the plane wall. The comparison of the turbulent kinetic energy production at different sections along the channel length (figure 2-8b) shows similar trends as observed for the Reynolds stress.

2.5 Discussion

The results presented in the preceding section describe the mean and turbulent flow structure in a channel bounded between a plane construction wall and a transpired corrugated wall at various Reynolds numbers. The mean velocity profiles (see figure 2-4a) show very weak mean flow in the separation zone in the trough region and the velocity gradually increased with height up to almost 1.5 times the corrugation wave height and then remained relatively constant with a slight increase towards the construction wall. The velocity then drops off again at the construction wall boundary layer with the thickness of almost one-third of the corrugation wave height. Some previous studies on the flow over a sinusoidal wavy wall reported significant mean velocity gradients throughout the channel and the location of the maximum mean velocity was shifted closer to the opposite plane wall [9,10]. They also observed very strong mean velocity gradients

in the region almost equal to the wave height. However, in the present study, the mean velocity gradients in this region were modest, and almost negligible mean velocity gradients were observed in the bulk region. One reason for this difference could be that in these studies the wave height was 5% [9] and 5-10% [10] of the total channel height, whereas, in the present case, the wave height was 27% of the total channel height. Therefore, in those studies the effect of the strong shear produced by the wave was experienced locally although it influenced the bulk domain by shifting the velocity maxima towards the opposite wall. In the present case, due to the smaller dimension of the channel relative to the wave, the shear generated by the corrugation wave was well mixed and diffused throughout the channel above the wave (see figure 2-2) and thus, the mean flow was relatively uniform. This indicates that the wave height relative to the channel height plays an important role in the diffusion of the shear. The shear generated by the present corrugation wave was stronger than that by a sinusoidal wave due to the more abrupt waveform as well as the transpired pores that formed additional roughness on the corrugation surface.

Results in figure 2-4a also show that the mechanism of shear generation at the corrugation wave was almost independent of the flow rate, the only exception being the lowest flow rate at $Re = 530$. The differences at this Reynolds number are likely due to the fact this Reynolds number is well within the laminar flow regime in a plane channel. In the present study, the shear generated by the wall induced instabilities in the flow. Such instabilities were strong enough to generate turbulence in the flow, which is evident in the plots of turbulent properties at this Reynolds number. Therefore, the influence of the shear, particularly in the region of high shear generation ($0.5 < y/h < 1.5$), was more dominant on the mean flow for low Reynolds numbers than that at higher Reynolds numbers in the classical transition or turbulent regimes.

The results in figure 2-4b show that the behaviour of mean velocity at different locations along the waveform is almost identical at the middle and top locations along the channel length. This indicates the flow is periodic over each waveform for most of the channel length. In the region near the inlet, there is some deviation from the behaviour observed downstream that could be due to the inlet effects, which as mentioned earlier, are three-dimensional in nature. As mentioned in the experimental setup section, the corrugated wall also has small perforations which could allow outside air to enter into the channel through perforations. However, almost equal magnitudes of the mean velocity at the middle and top sections along the channel length indicate that the air flow rate through these perforations is almost negligible. This could be due to the reason that the pores were very small (of the order of 100 microns) and therefore, the flow resistance through these pores was substantially higher as compared to that through the open inlet at the bottom of the channel. Although the mean streamwise velocity magnitude was lower at the bottom section as discussed earlier, it could be due to the distribution of the bulk flow among the three velocity components originating from the presence of flow three-dimensionality. This would result in the relatively lower magnitude of the streamwise velocity components. This hypothesis was confirmed by the presence of the larger magnitude of mean cross-stream component compared to that at the middle section. Therefore it can be concluded that in the presence of an open inlet at the bottom, these pores do not play any active role in drawing the air into the channel and may not be needed. Their role could be significant if the bottom inlet is kept closed and the air is forced to be drawn through these pores. In this case however, strong suction pressure is needed to overcome the flow resistance through these pores.

The comparison of various turbulent characteristics over the corrugation waveform show a similar trend that the turbulence is enhanced in the region $1 < y/h < 1.5$. However, this

enhancement of turbulence is more profound in the trough region as compared to that above the crest. The results show that the turbulence in the channel was almost entirely produced in this region above the trough (see figure 2-8). Previous studies on the flow over a sinusoidal wave also observed the enhancement of turbulent kinetic energy production in this region [3,9,10]. They also observe a significant drop of the production magnitude to almost zero outside this region. Kruse *et al.*[10] observed that the turbulent kinetic energy production magnitudes near the opposite smooth wall were still measureable in relation to that near the sinusoidal wave. Whereas in the present study, the production magnitudes near the plane construction wall are almost negligible as compared to that near the corrugation wall. The plausible reasons for this difference are the shape of the waves and the wave height-to-channel height ratio, which are significantly different in both studies.

The Reynolds stress profiles show that the Reynolds stress magnitudes and the thickness of the enhanced Reynolds stress layer within this region increased from the crest and reached the maximum magnitude and thickness in the middle of the trough ($x/\lambda = 0.75$) and then gradually decreased to the next crest. Breuer *et al.* [1], and Hudson *et al.* [9] also observed a similar trend over sinusoidal waves. In a classical case of plane channel, the Reynolds stress approaches zero at the channel core [18], however, in the presence of a wavy wall, the location of the zero Reynolds stress extended beyond the channel centerline towards the plane wall as demonstrated in figure 2-7 and also supported by Hudson *et al.* [9] and Kruse *et al.*[10]. The results also show that overall the Reynolds stress magnitude is significantly higher in the vicinity of the corrugation wall as compared to the construction wall. In fact, the Reynolds stress magnitude near the construction wall is almost negligible as compared to that near the corrugation which is consistent with Breuer *et al.* [1] and Kruse *et al.*[10]

Breuer *et al.*, [1] Hudson *et al.*, [9] and Kruse *et al.* [10] observed a significant reduction in the Reynolds stress magnitude from the peak value at the wave height to the zero location. In the present study, this reduction is more gradual resulting with the location of the zero Reynolds stress being closer to the construction wall. The Reynolds stress quantifies the momentum transfer by the turbulent velocity field [18]. The larger magnitude of Reynolds stress in the vicinity of the corrugation wave implies a significant momentum transfer from the corrugation wall by the turbulent velocity field. Thus, the location of the zero Reynolds stress indicates the extent of this enhanced momentum transfer. It can be argued that the corrugation waveform generates strong turbulence which is transported more effectively over a wider region. Such an argument is consistent with the dynamics of the turbulent velocity fields in figure 2-3, where the momentum transport from the corrugation waveform towards the bulk flow domain in the form of bursting flow and vortex advection is clearly evident. The plots of turbulent properties demonstrate that the turbulence produced by the corrugation waveform dominates the entire channel.

The profiles of turbulent properties at different channel locations along its length showed that the mechanisms of turbulence production and diffusion are quite periodic. The trends however, are somewhat different at the bottom section compared to the middle and top sections. The differences in the structure of the turbulent flow at the bottom section with that at the middle and top sections are more profound in the trough region. Almost all profiles of various turbulent properties show that the location of the peak magnitude of turbulence in the crest region at the bottom section is closer to that at other heights. However, moving along the waveform towards the trough, the peak location starts to shift closer to the trough wall at the bottom section. Conversely at higher sections, the peak remains consistently located around the wave height

($y/h \sim 1$). As discussed earlier, these differences are likely due to the three-dimensional nature of the flow in the inlet region, which affected the turbulence production and diffusion mechanisms in the bottom section of the channel. Results from the present study do not provide any precise information about the distance from the channel inlet up to which the inlet flow dynamics influence the turbulent flow structure in the channel.

In the present study, five Reynolds numbers are considered. Based on the standard smooth channel configuration, the top two Reynolds number ($Re = 4140, 6650$) lie within a fully turbulent regime, while the two next lower Reynolds numbers ($Re = 2030, 2675$), lie within or closer to the transition regime. The lowest Reynolds number ($Re = 530$) falls well within the laminar regime. The results show that the structure of turbulent flow was similar at the four higher Reynolds numbers while significantly different, particularly in the trough region, at the lowest Reynolds number. In laminar flows at relatively low Reynolds numbers, the viscous effects are strong enough to dissipate any instability generated in the flow. In such case, the amplitude and hence the energy of the instability is typically small. However, in the present case, results show that the flow at this Reynolds number was turbulent. This indicates that the instabilities introduced by the present waveform were strong enough to overcome the viscous effects and thereby becoming sustained, which led to the flow transformation into turbulence. This is only possible when the magnitude of such instabilities is significantly high. Since the source of instabilities in the present case is the waveform; the strongest instabilities are expected to be generated in the vicinity of the waveform, particularly in the trough region. Away from the waveform, the magnitude of these instabilities is expected to be low. At low Reynolds numbers, the magnitude of the mean streamwise velocity is also low. In other words, in the classical laminar flow regime, for the transition to turbulence, the ratio of the instability magnitude to the

mean velocity magnitude should be significantly high as compared to that in the conventional transitional or turbulent regimes. Therefore, when normalized by the respective bulk velocity, the magnitudes of normalized turbulent properties are expected to be high at low Reynolds numbers (which are well within the conventional laminar regime) in the regions where the instabilities are strong while considerably lower in the region where the instabilities are weak. The results at the lowest Reynolds number show this behaviour with higher magnitudes of normalized turbulent properties in the trough region and lower magnitudes of normalized turbulent properties in the bulk domain as compared to that at the higher Reynolds numbers.

In the classical case of forced convection heat transfer from a heated wall to the adjacent flowing fluid, the heat is first transferred from the wall into the fluid thermal boundary layer and then this heat diffuses into the bulk flow. For a given fluid, the effectiveness of this heat transfer lies on the thickness of the thermal boundary layer and the dynamics of the bulk flow. The main resistance to heat transfer lies within the thermal boundary layer where the heat is transferred via conduction. The strong turbulent vortices generated near the wall enhance the heat transfer via two mechanisms: first they either disrupt or reduce the thickness of this boundary layer (i.e. reducing the conductive resistance) and second, they carry the hot fluid parcels from the wall towards the bulk flow enhancing the heat diffusion.

The main objective of the transpired air collector configuration is to effectively transfer heat from the corrugation wall (exposed to sun) to the air flowing through the channel. The results presented in this study provide the first qualitative and quantitative assessment of the mean and turbulent flow structure in such a configuration. Present results show that the corrugation waveform not only significantly enhances turbulence but also effectively diffuse it throughout the channel. That is, strong turbulent vortices and bursts are generated near the wavy wall,

which are then advected into the bulk domain. These turbulent structures thus enhance heat transfer from the wall into the air flow via the two mechanisms discussed earlier. In solar energy systems, the flow rates are typically kept low in order to increase the fluid temperature. The present results show that this corrugation waveform generates turbulence at relatively low flow rates, which implies an effectively heat transfer even at low flow rates compared to that at a plane wall. Thus, such a corrugation waveform would enhance the thermal performance of a transpired air collector.

2.6 Conclusions

Results are reported from an experimental study conducted to investigate the air flow behaviour in a vertical channel bounded by a transpired air collector corrugated surface and a plane construction wall. PIV measurements obtained two dimensional velocity fields at three channel positions and five Reynolds numbers. The results show that the corrugation waveform substantially modified both mean and turbulent flow structure inside the channel. The instantaneous velocity fields showed that the shear layer at the boundary of the bulk and separated flows oscillates in time, which in turn affects the size and strength of separation vortices. The rate and amplitude of shear layer oscillations increased with the Reynolds number resulting in a stronger bulk and separated flow interaction, which extends deeper into the bulk flow. The turbulent flow field was comprised of strong bursting flow originating from the trough, sweeping flow from the bulk region, and a combination of the vortex shedding off the crest with the mixing layer in the separation region. Their interactions created a complex three-dimensional flow structure extended over almost the entire channel.

Mean velocity profiles show very weak mean flow in the separation zone and relatively uniform flow in the bulk region. The mean velocity gradients near the corrugation wave height were modest, and almost negligible in the bulk region indicating a strong diffusion of the shear. It was found that the mechanism of shear generation at the corrugation wave was almost independent of the flow rate. The turbulent characteristics over the corrugation waveform show a similar trend that the turbulence is enhanced in the region $1 < y/h < 1.5$. However, this enhancement of turbulence is more profound in the trough region as compared to that above the crest. The results also show that the turbulence in the channel was almost entirely produced in this region above the trough. The profiles of the Reynolds stress indicated a significant momentum transfer from the corrugation wall by the turbulent velocity field and the extent of this enhanced momentum transfer. The results demonstrate that the turbulence produced by the corrugation waveform dominates the entire channel.

The comparison of the flow behaviour at different heights along the channel length indicates that the mean flow and associated shear generation, and the production and diffusion of turbulence are periodic with respect to the waveform in the channel with the exception at the bottom section of the channel. This discrepancy was attributed to the inlet effects causing strong three-dimensionality in the flow. The Reynolds numbers considered in the present study covered the classical range of laminar, transition and turbulent flow regimes. The results show the presence of strong turbulence even at the Reynolds number that falls within the laminar range. However, the structure of turbulent flow at this Reynolds number was different from the other cases. It was argued that the corrugation waveform induced strong instabilities in the flow that led to the transformation of flow into turbulence. It can be concluded that the strong production of turbulence by the corrugation waveform and its effective diffusion throughout the channel would

significantly enhance the heat transfer from the corrugation wall and hence would enhance the thermal performance of a transpired air collector.

2.7 Acknowledgements

Authors would like to acknowledge Natural Sciences and Engineering Research Council of Canada (NSERC), the Canadian Solar Buildings Research Network (SBRN) and the University of Western Ontario for providing the support.

2.8 References

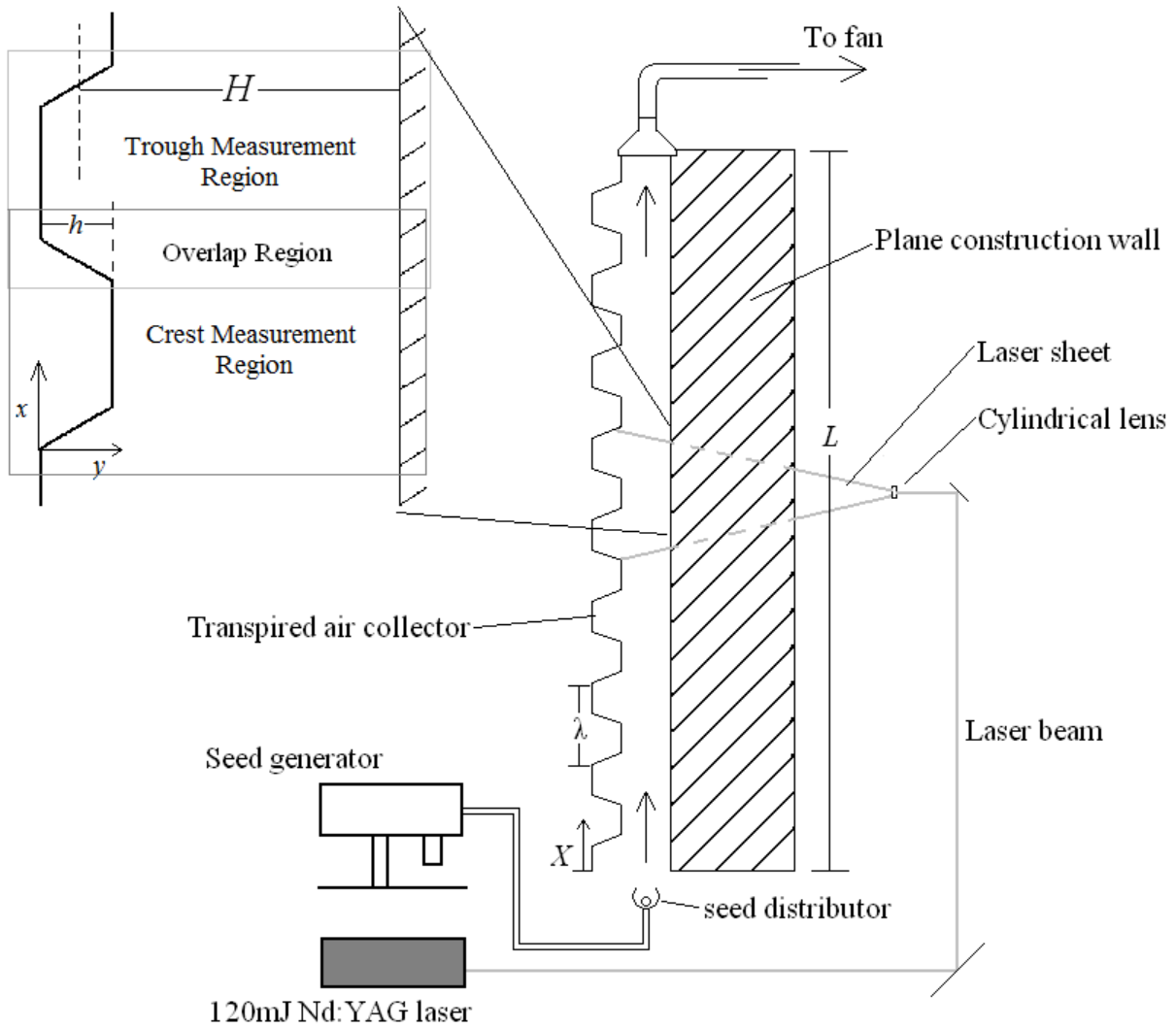
- [1] M. Breuer, N. Peller, Ch. Rapp, and M. Manhart, Flow over periodic hills – Numerical and experimental study in a wide range of Reynolds numbers, *Computers and Fluids* 38, (2009) 433-457.
- [2] J. D. Kuzan, T. J. Hanratty and R. J. Adrian, Turbulent flows with incipient separation over solid waves *Exp Fluids* 7, (1989) 88-98.
- [3] N. Shaikh and K. Siddiqui, An experimental investigation of the near surface flow over air-water and air-solid interfaces, *Phys. Fluids*. 22, 025103 (2010).
- [4] M.A. Niederschulte, R.J. Adrian, T.J. Hanratty, Measurements of turbulent flow in a channel at low Reynolds numbers, *Exp. Fluids* 9, (1990) 222-230.
- [5] A. E. Perry, K. L. Lim, and S. M. Henbest, An experimental study of the turbulence structure in smooth- and rough-wall boundary layers, *J. Fluid Mech.* 177, (1987) 437-466.
- [6] P.-A. Krogstad, R. A. Antonia, Surface roughness effects in turbulent boundary layers, *Exp. Fluids* 27, (1999) 450-460.
- [7] J. Buckles, T.J. Hanratty and R.J. Adrian, Turbulent flow over large-amplitude wavy surfaces, *J. Fluid Mech.* 140, (1984) 27-44.

- [8] R. J. Calhoun and R. L. Street, Turbulent flow over a wavy surface' Neutral case, J. Geophys. Res. 106, (2001) 9277-9293.
- [9] J. D. Hudson, L. Dykhno, and T. J. Hanratty, Turbulence production in flow over a wavy wall, Exp. Fluids 20, (1996) 257-265.
- [10] N. Kruse, S. Kuhn, and P. R. V. Rohr, Wavy wall effects on turbulence production and large-scale modes, J. Turbul. 7, N31 (2006).
- [11] S. Nakagawa, and T.J. Hanratty, Particle image velocimetry measurements of flow over a wavy wall, Phys. of Fluids 13, N11 (2001).
- [12] Y.-T Yang, and P.-J Chen, Numerical simulation of fluid flow and heat transfer characteristics in channel with V corrugated plates, Heat Mass Transf. 46, (2010) 437-445.
- [13] H. Stel, R.E.M. Morales, A.T. Franco, S.L.M. Junqueira, R.H. Erthal, M.A.L. Gonçalves, Numerical and Experimental Analysis of Turbulent Flow in Corrugated Pipes, J. Fluids Eng. 132, (2010) 071203.
- [14] M. H. K. Siddiqui, M. R. Leowen, C. Richardson, W. E. Asher, and A. T. Jessup, Simultaneous particle image velocimetry and infrared imagery of micro-scale breaking waves, Phys. Fluids 13, (2001) 1891.
- [15] E. A. Cowen, S. G. Monismith, A hybrid digital particle tracking velocimetry technique, Exp. Fluids 22, (1997) 199.
- [16] A. K. Prasad, R. J. Adrian, C.C. Landreth, and P. W. Offutt, Effect of resolution on the speed and accuracy of particle image velocimetry interrogation, Exp. Fluids 13, (1992) 105.
- [17] W. W. Willmarth and S. S. Lu, Structure of the Reynolds stress near the wall, J. Fluid Mech. 55, (1972) 65-92.
- [18] S. B. Pope, Turbulent Flows, Cambridge University Press, 2000.

[19] H. Tennekes, J.L Lumley, A first course in turbulence, The Massachusetts Institute of Technology, 1972.

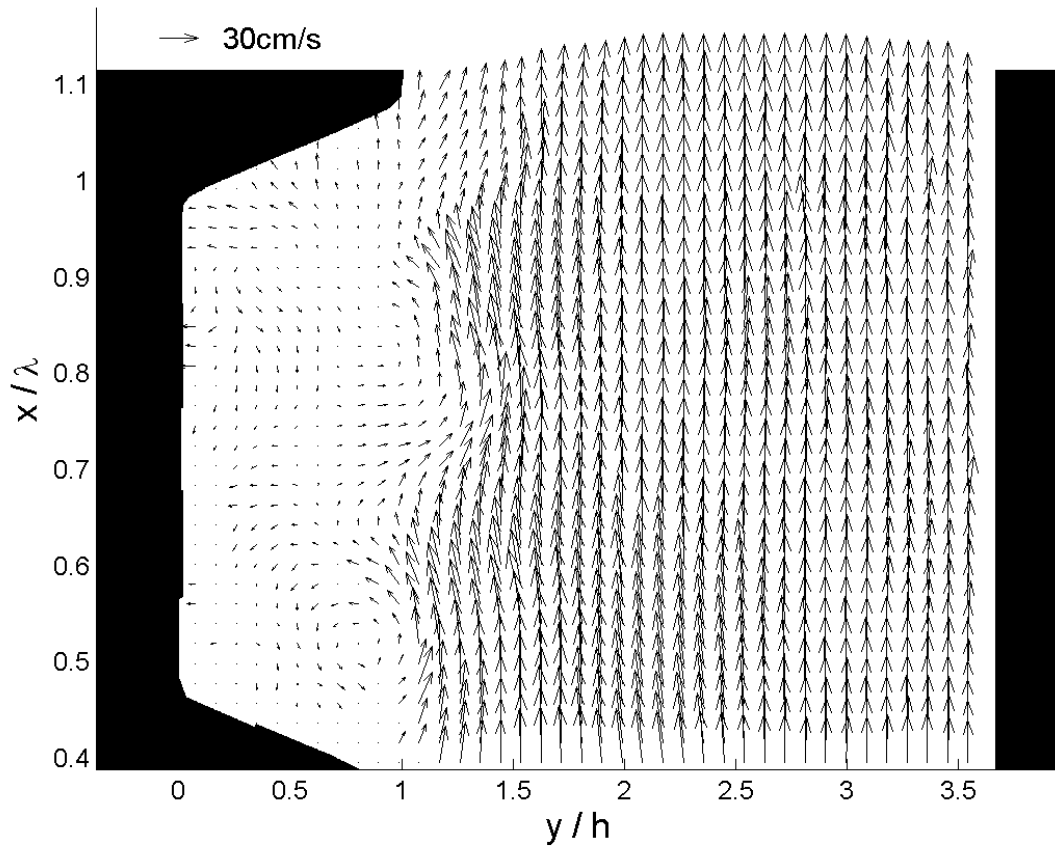
2.9 Figures

Figure 2-1

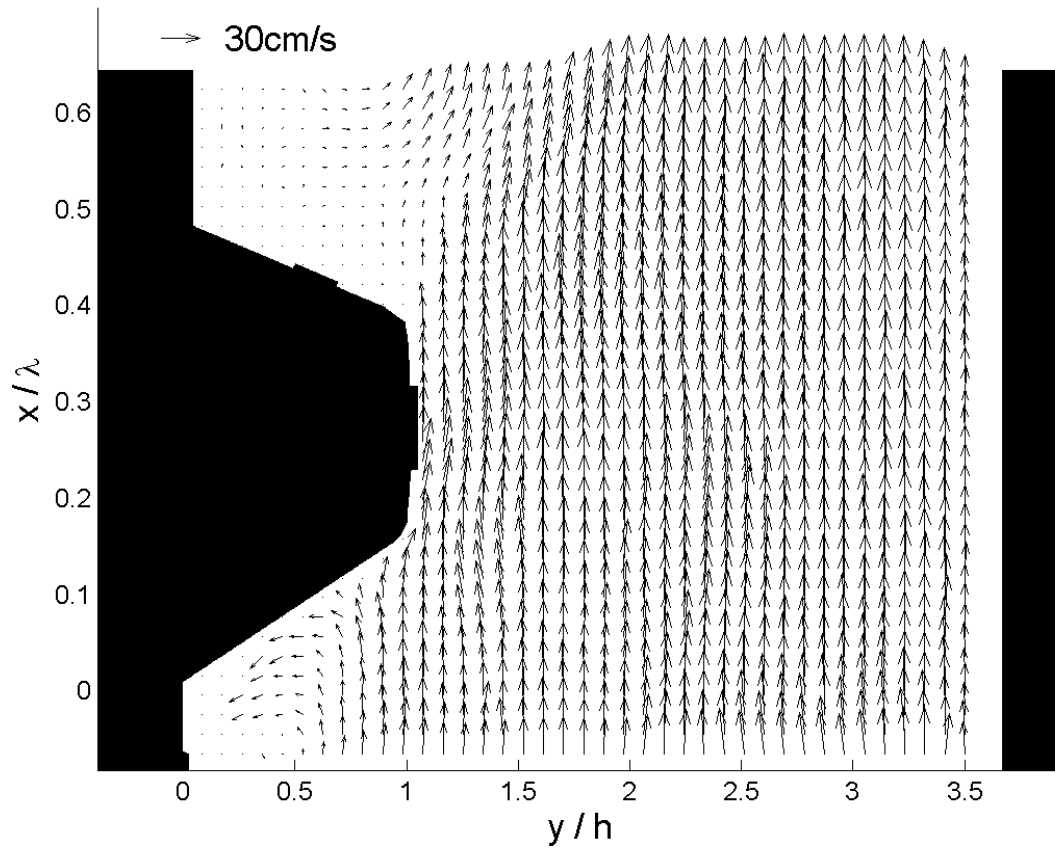


2-1: Schematic of the experimental setup.

Figure 2-2



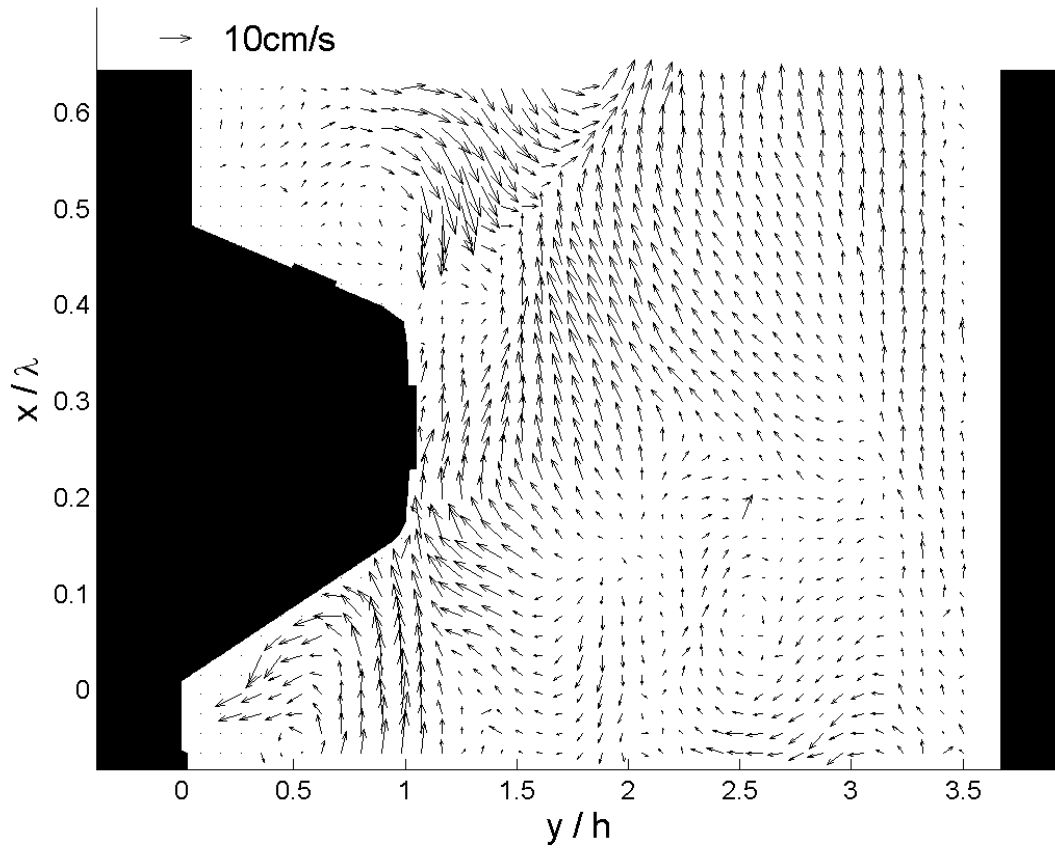
a)



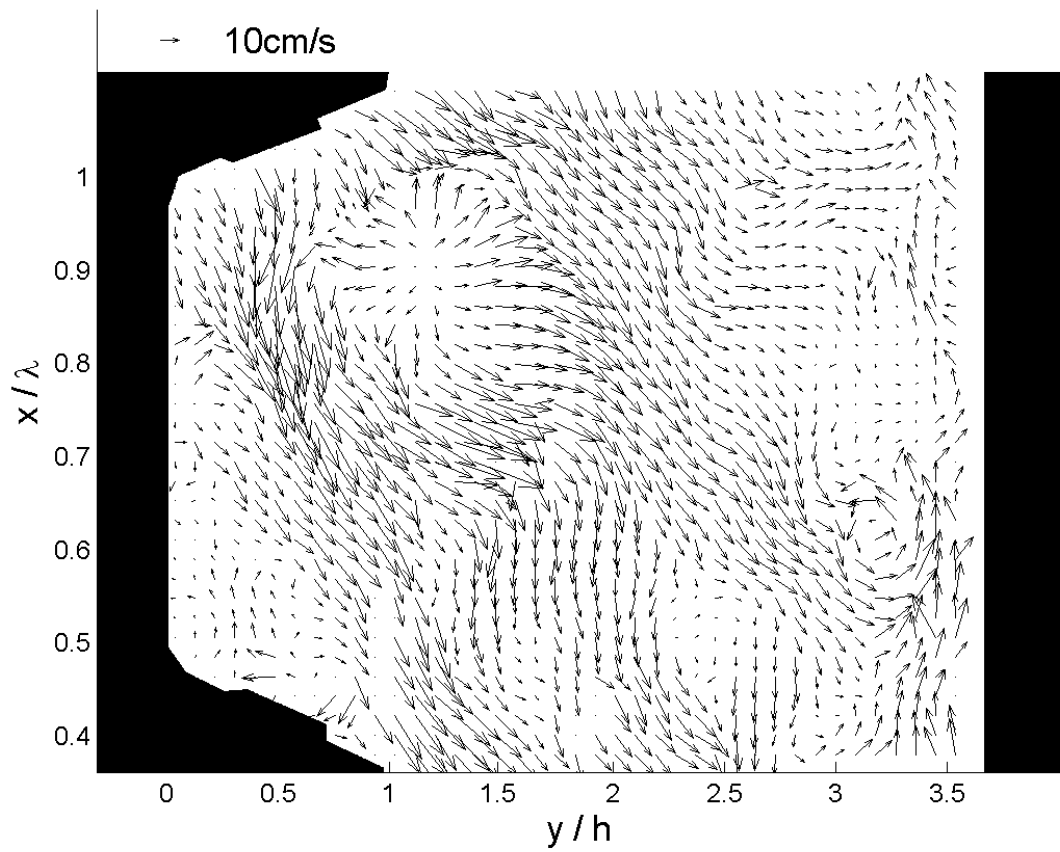
b)

2-2: Snapshots of instantaneous velocity fields at the middle channel height ($X/L = 0.57$) in (a) the trough section; (b) the crest section, at $Re = 2675$. $\lambda =$ corrugation wavelength; $h =$ corrugation wave height. The resolution of the velocity field is reduced in the plots for the better illustration of the flow dynamics.

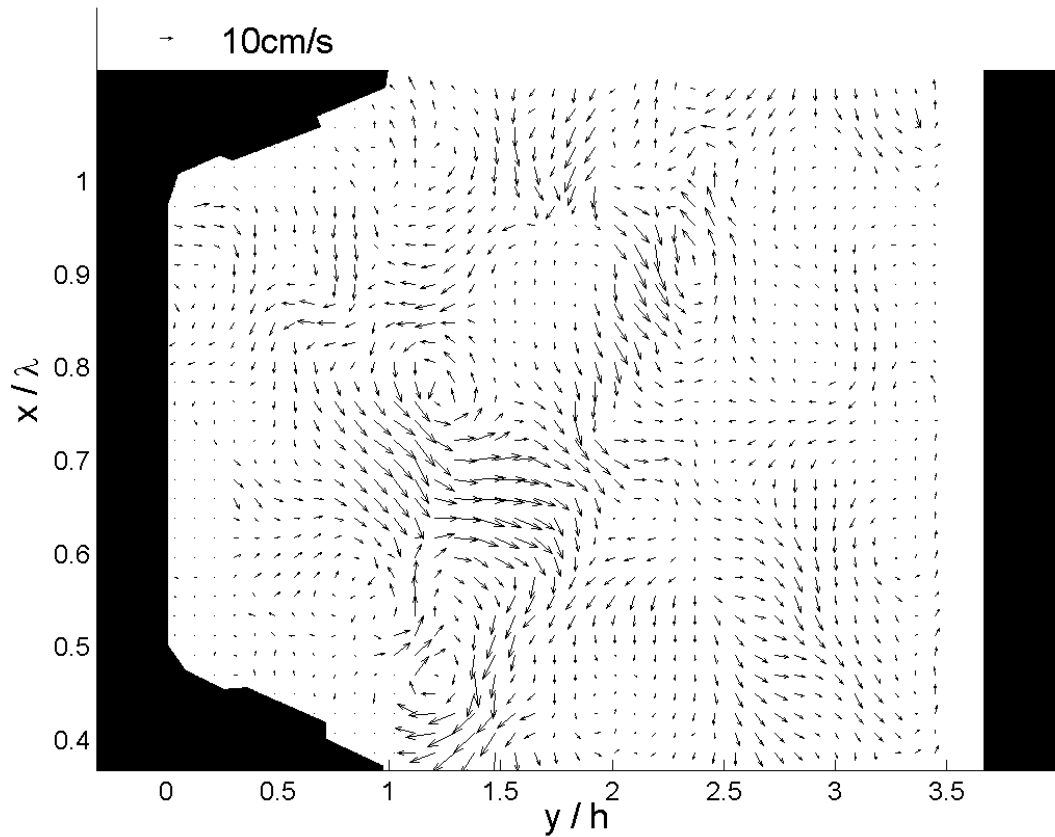
Figure 2-3



a)



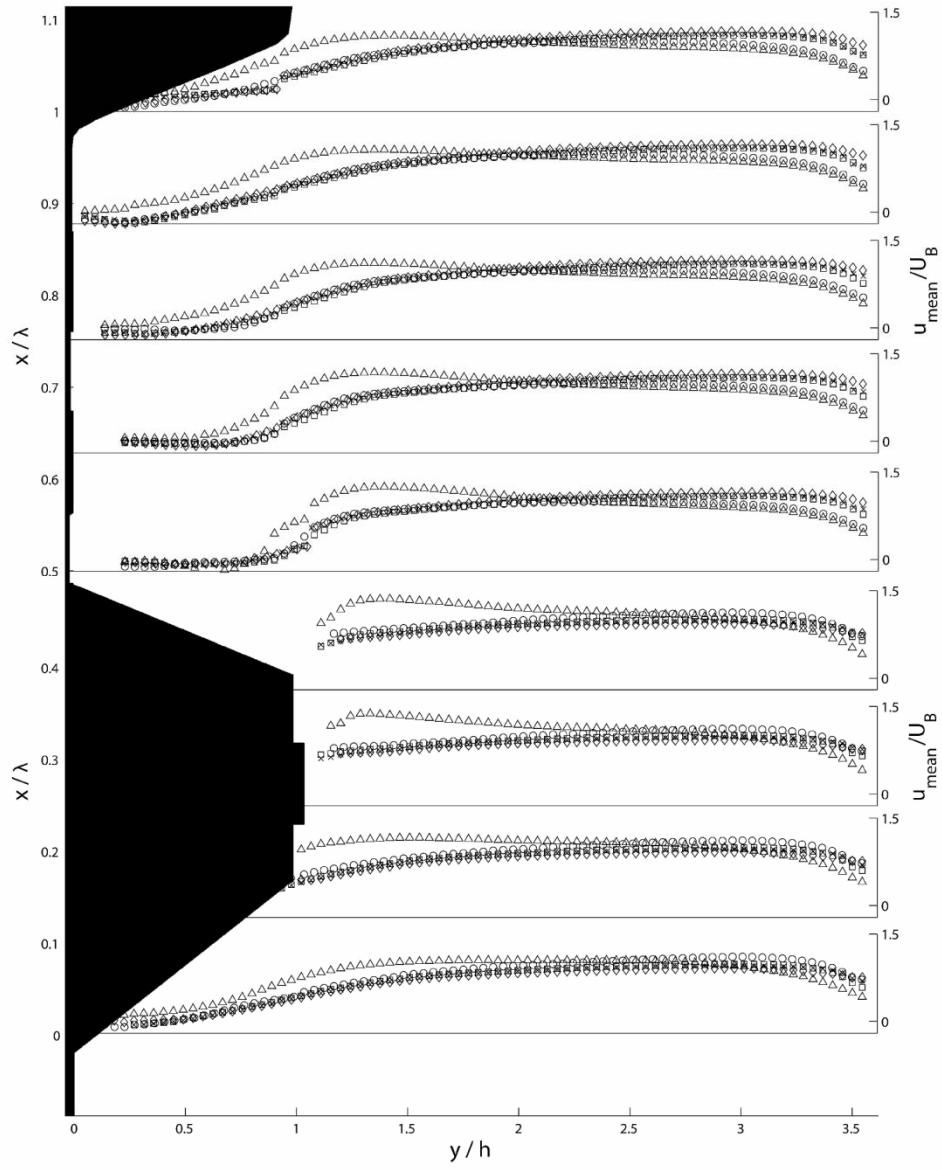
b)



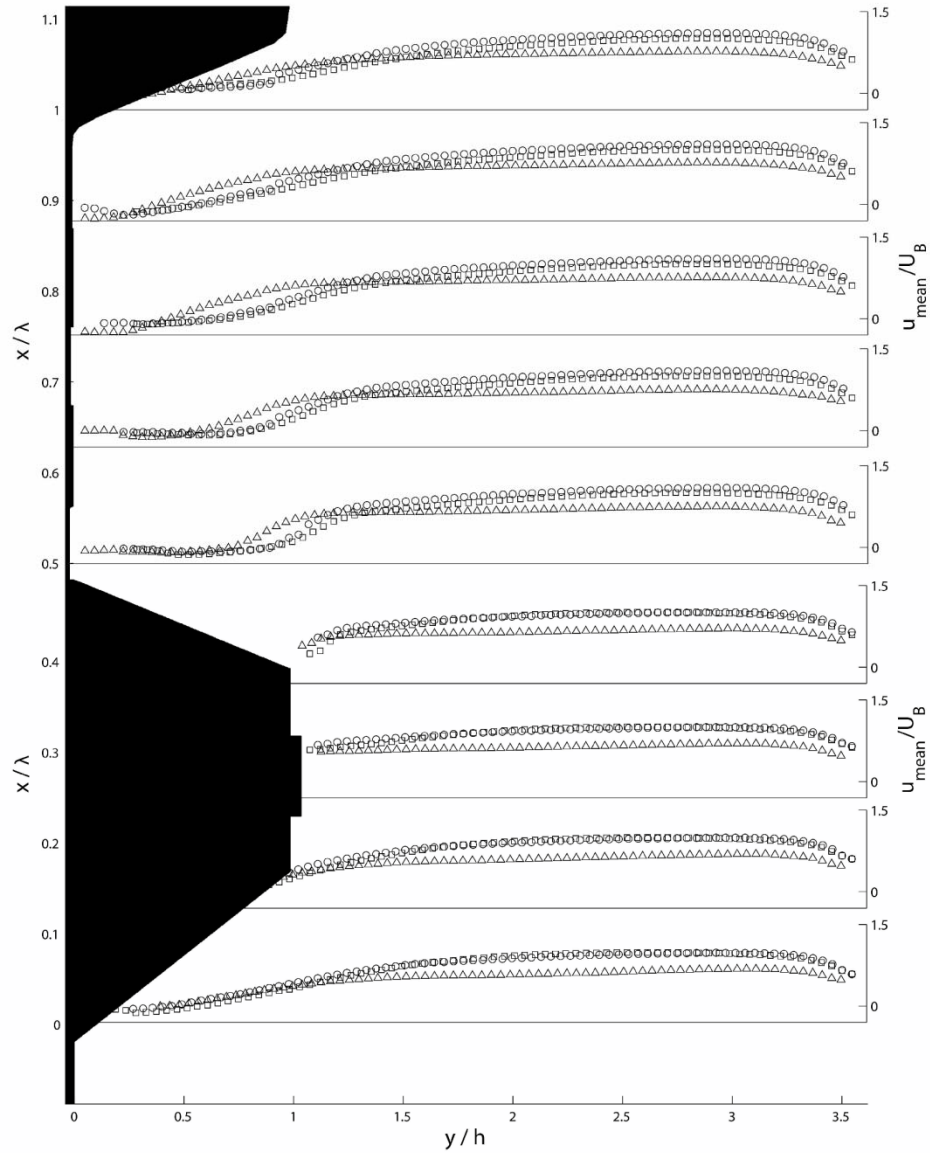
c)

2-3: Snapshots of the turbulent velocity vector fields at various locations along the channel at different Reynolds numbers. (a) The crest section at $X/L = 0.57$, $Re = 2675$; (b) the trough section at $X/L = 0.18$, $Re = 4140$; (c) the trough section at $X/L = 0.57$, $Re = 4140$. The resolution of the velocity field is reduced in the plots for the better illustration of the flow dynamics.

Figure 2-4



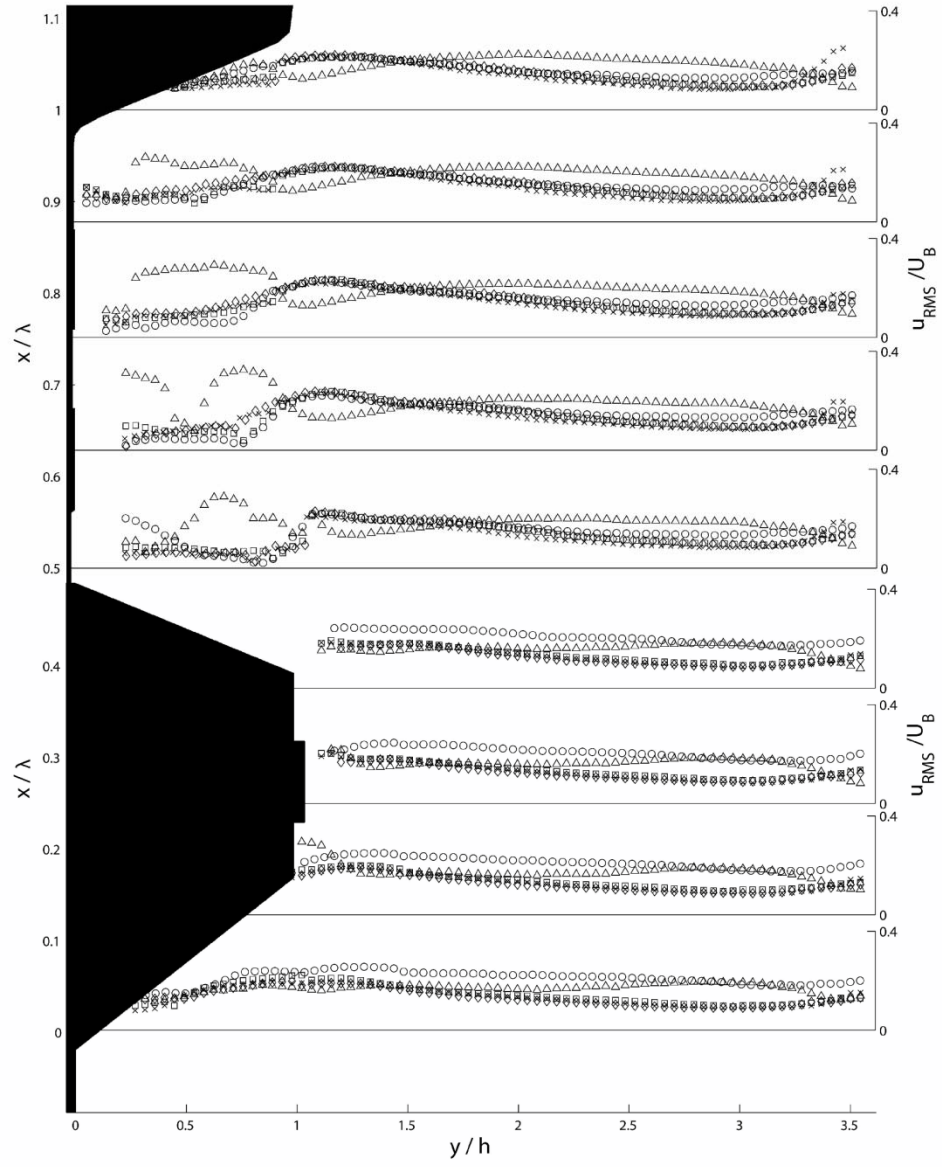
a)



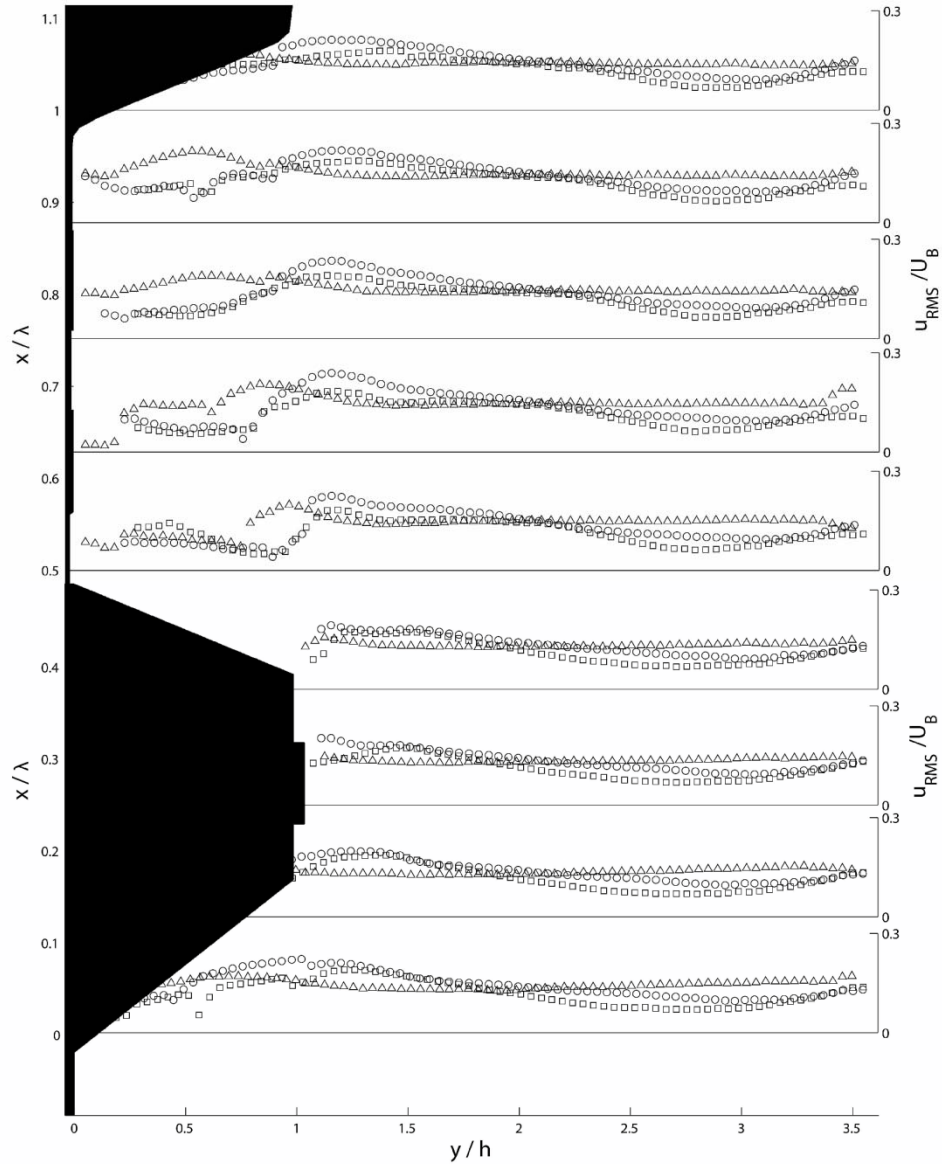
b)

2-4: Mean velocity profiles at various locations over the corrugation waveform normalized by the bulk velocity (U_B); (a) at the middle height of the channel ($X/L = 0.57$) at various Reynolds numbers. (Δ), $Re = 530$; (\circ), $Re = 2030$; (\square), $Re = 2675$; (\diamond), $Re = 4140$; (\times), $Re = 6650$. (b) At various heights along the channel length for $Re = 2675$. (Δ), $X/L = 0.18$; (\circ), $X/L = 0.57$; (\square), $X/L = 0.8$.

Figure 2-5



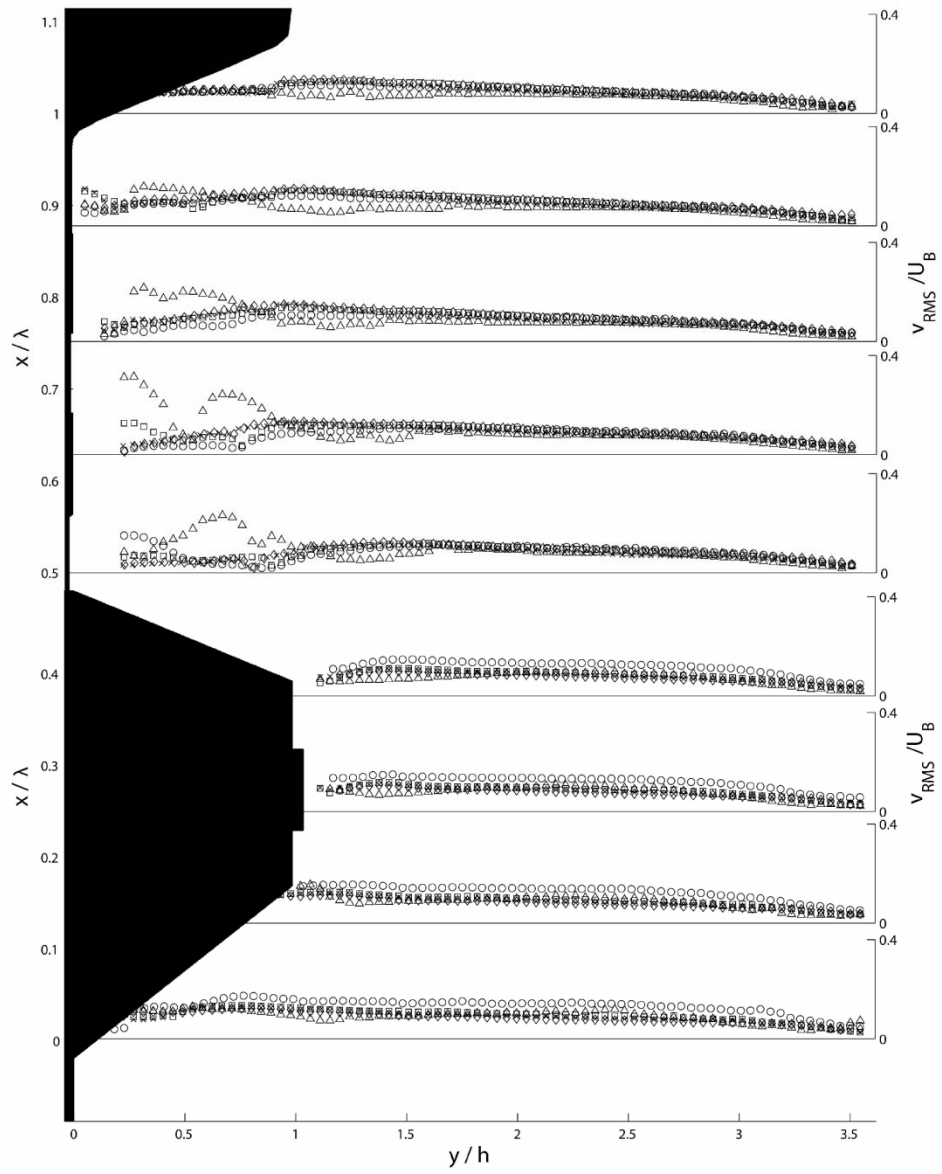
a)



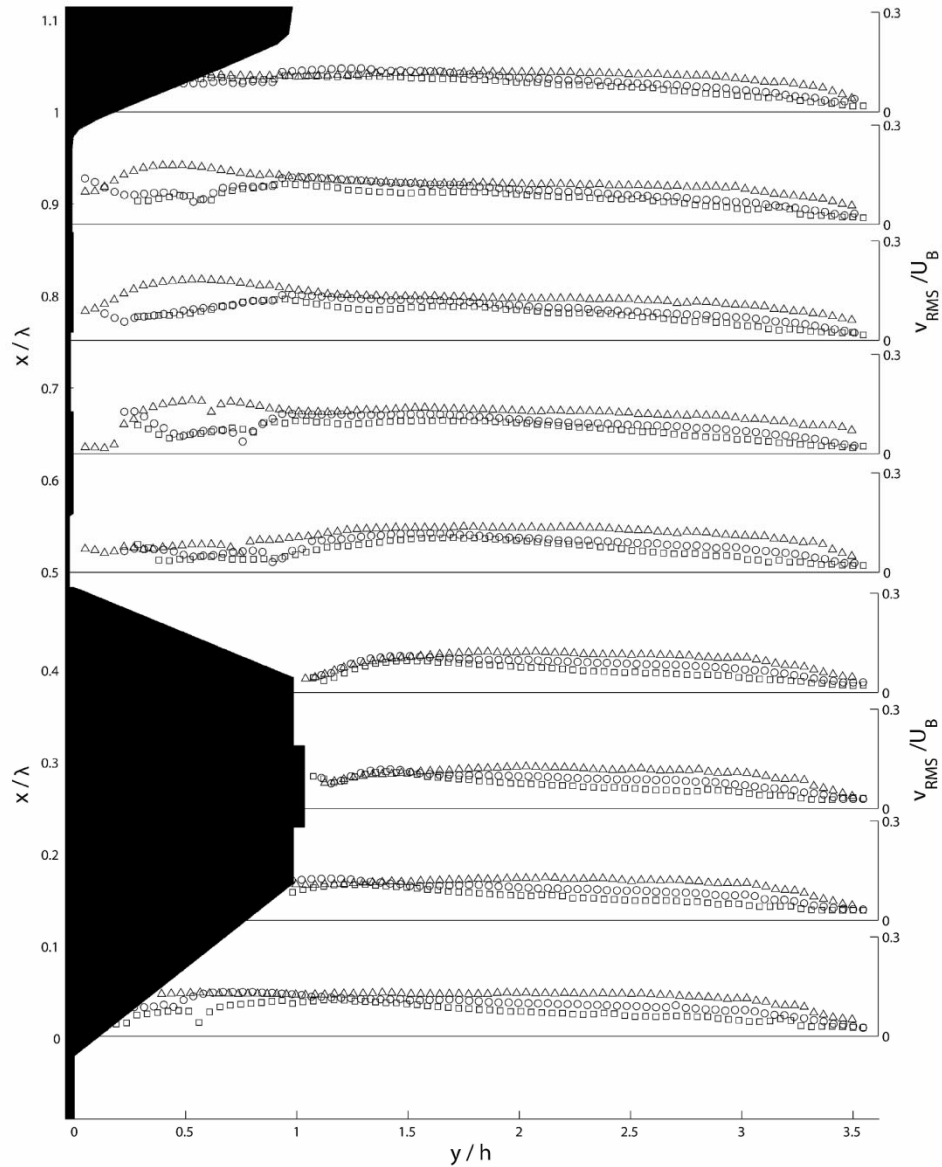
b)

2-5: Profiles of the RMS streamwise turbulent velocity at various locations over the corrugation waveform normalized by U_B ; (a) at the middle height of the channel ($X/L = 0.57$) at various Reynolds numbers. (Δ), $Re = 530$; (\circ), $Re = 2030$; (\square), $Re = 2675$; (\diamond) $Re = 4140$; (\times), $Re = 6650$. (b) At various heights along the channel length for $Re = 2675$. (Δ), $X/L = 0.18$; (\circ), $X/L = 0.57$; (\square), $X/L = 0.8$.

Figure 2-6



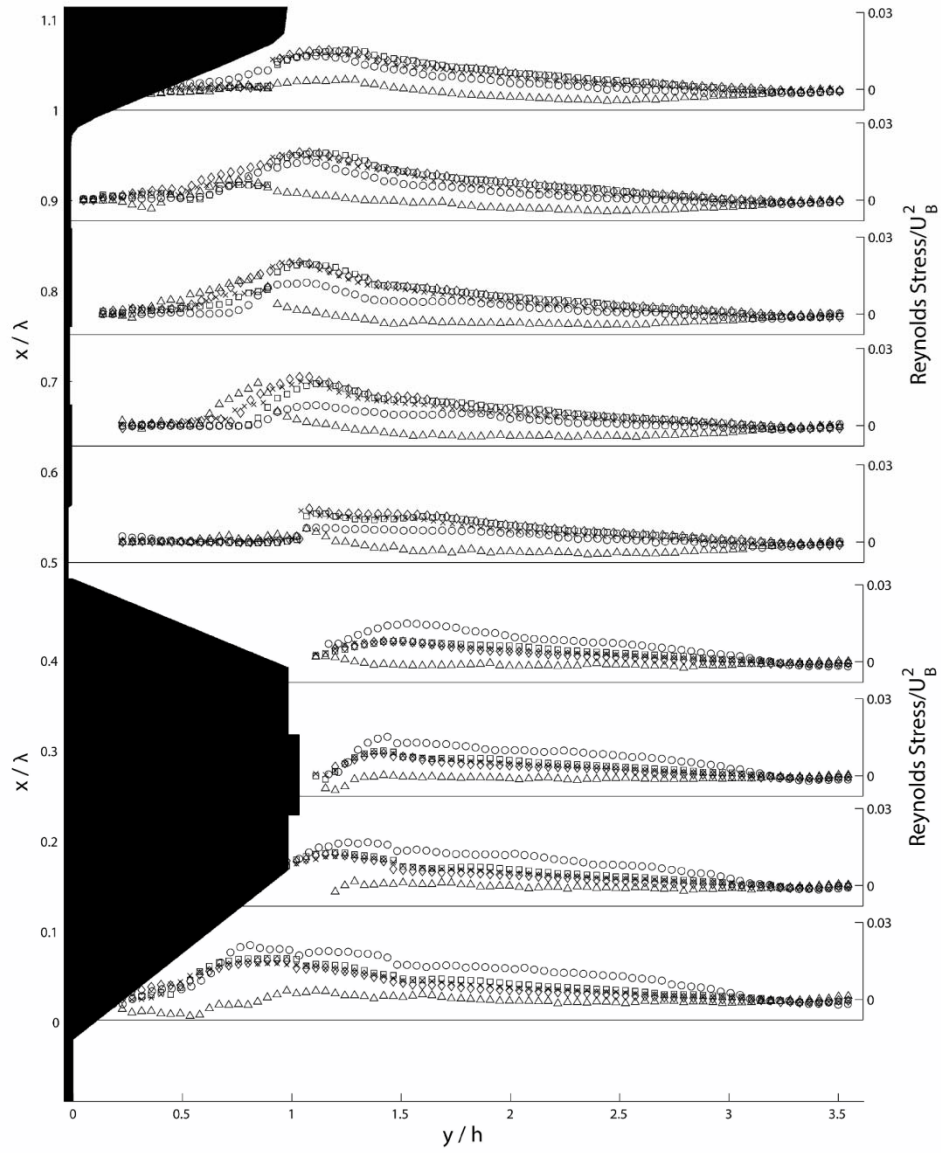
a)



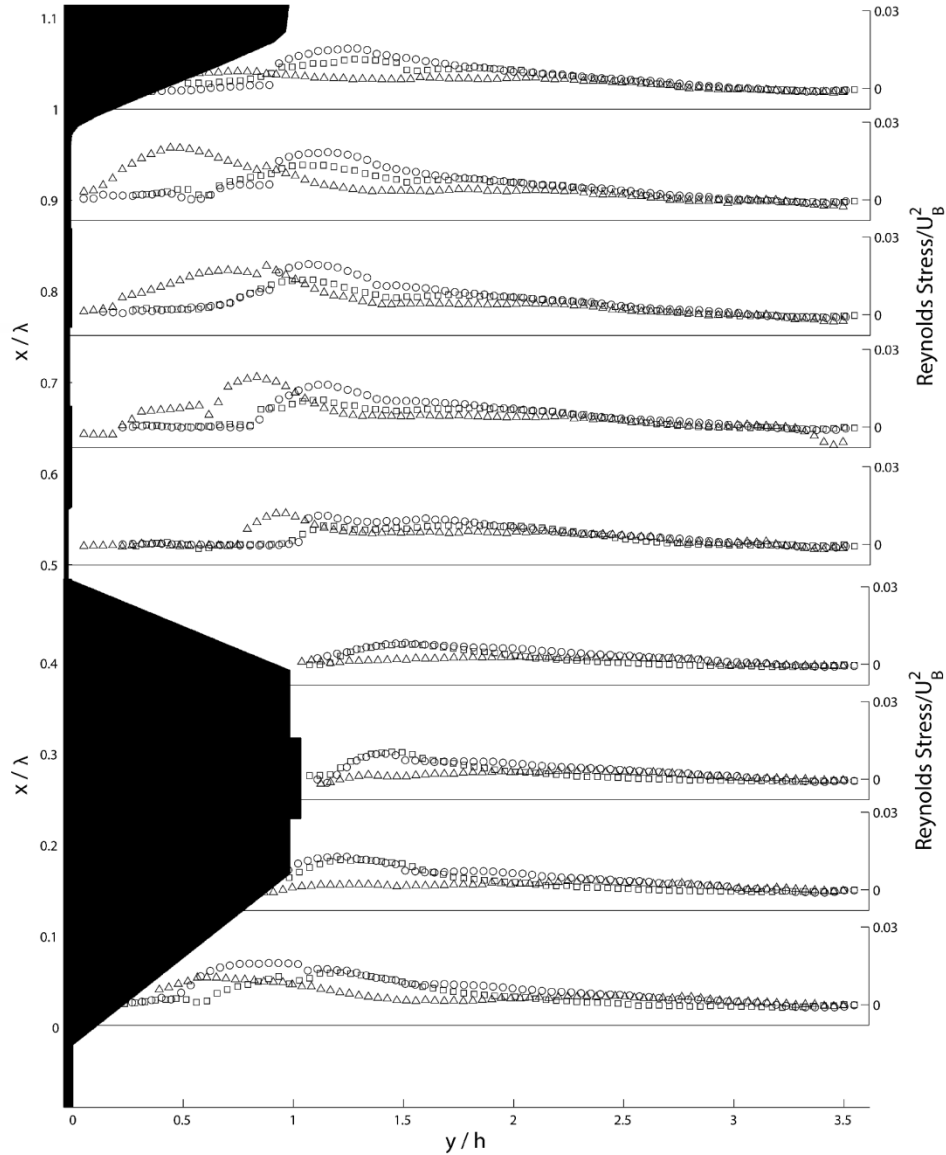
b)

2-6: Profiles of the RMS cross-stream turbulent velocity at various locations over the corrugation waveform normalized by U_B ; (a) at the middle height of the channel ($X/L = 0.57$) at various Reynolds numbers. (Δ), $Re = 530$; (\circ), $Re = 2030$; (\square), $Re = 2675$; (\diamond) $Re = 4140$; (\times), $Re = 6650$. (b) At various heights along the channel length for $Re = 2675$. (Δ), $X/L = 0.18$; (\circ), $X/L = 0.57$; (\square), $X/L = 0.8$.

Figure 2-7



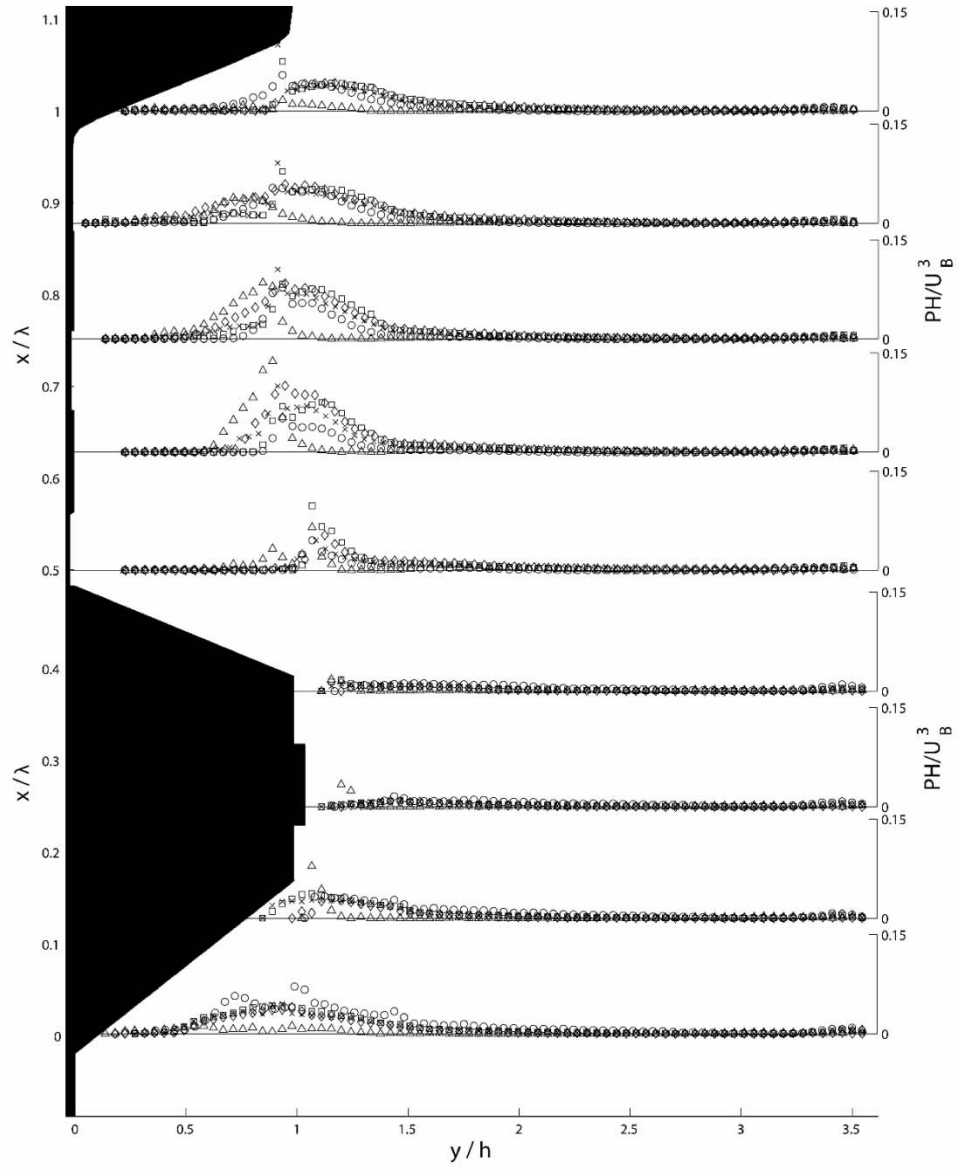
a)



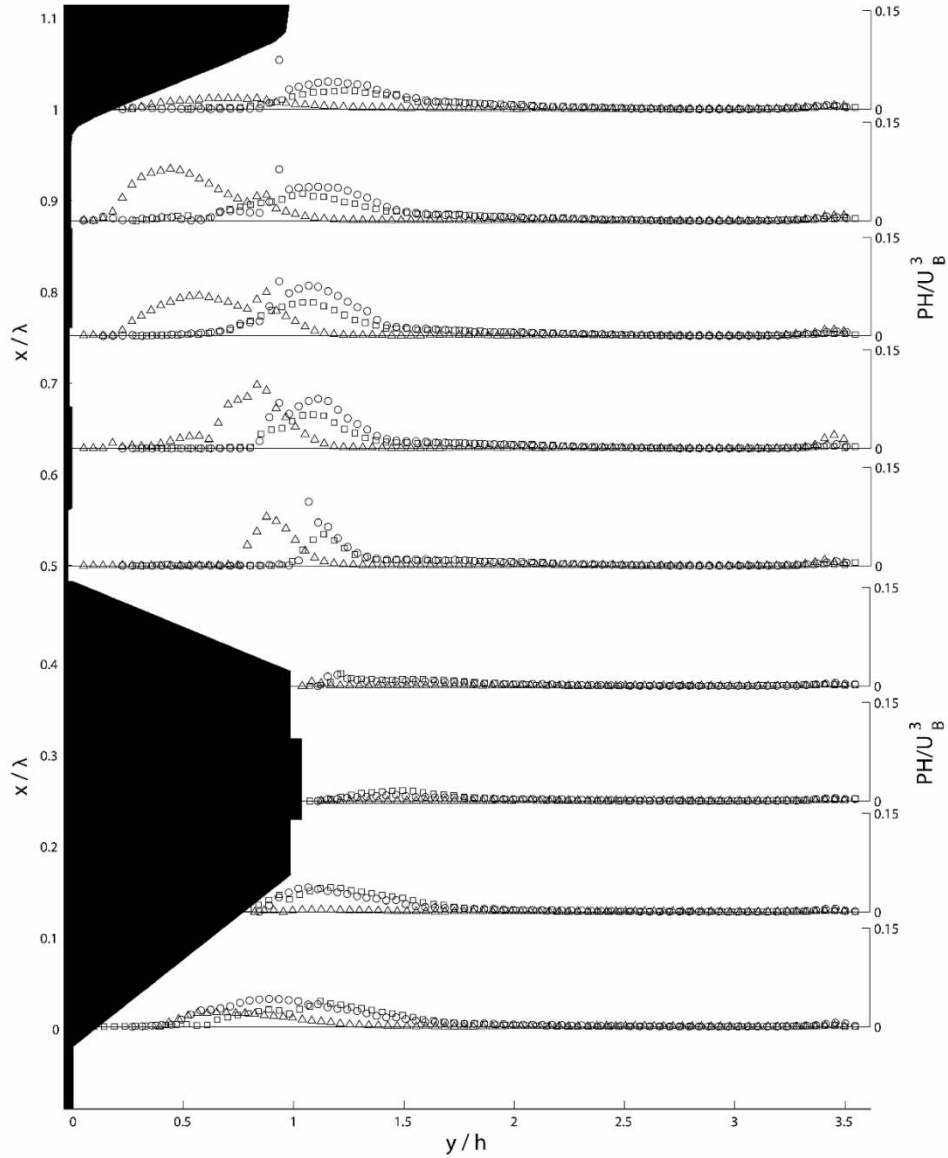
b)

2-7: Profiles of Reynolds Stress ($-\overline{u'v'}$) at various locations over the corrugation form normalized by U_B ; (a) at the middle height of the channel ($X/L = 0.57$) at various Reynolds numbers. (Δ), $Re = 530$; (\circ), $Re = 2030$; (\square), $Re = 2675$; (\diamond) $Re = 4140$; (\times), $Re = 6650$. (b) At various heights along the channel length for $Re = 2675$. (Δ), $X/L = 0.18$; (\circ), $X/L = 0.57$; (\square), $X/L = 0.8$.

Figure 2-8



a)



b)

2-8: Profiles of the turbulent kinetic energy production (P) normalized by U_B and the channel height H ; (a) at the middle height of the channel ($X/L = 0.57$) at various Reynolds numbers. (Δ), $Re = 530$; (\circ), $Re = 2030$; (\square), $Re = 2675$; (\diamond) $Re = 4140$; (\times), $Re = 6650$. (b) At various heights along the channel length for $Re = 2675$. (Δ), $X/L = 0.18$; (\circ), $X/L = 0.57$; (\square), $X/L = 0.8$.

Chapter 3

The influence of surface heating on the flow dynamics within a transpired air collector

3.1 Abstract

An experimental study was conducted to examine the air flow behaviour in the channel of a transpired air collector under different heating conditions. Velocity fields were measured using Particle Image Velocimetry (PIV). Mean velocities and turbulent properties were computed and evaluated. At high flow rates, the flow is dominated by forced convection while at the lowest flow rate the flow is primarily buoyancy driven, where buoyancy induced stabilities and heating effects are strongest. It was observed that the buoyancy-induced instabilities enhanced the magnitude and modified the structure of mean and turbulent properties as compared to the unheated flow. The flow rate influenced the relative magnitudes of the normalized mean and turbulent velocities that were enhanced with a decrease in the flow rate at a given heating condition. Collector efficiencies up to 70% were observed, which could be attributed to the corrugation surface geometry that enhanced turbulence and provided a larger heat transfer surface area.

Keywords:

Turbulent flow, Particle Image Velocimetry, transpired solar collector, corrugated surface, constant heat flux.

3.2 Introduction

A recent estimate from the International Energy Agency (IEA) states the global energy demand is expected increase by 35% between the years 2008 and 2035 [1]. Due to the limited reserves of conventional fossil fuels and their harmful effects on the environment, it is crucial to explore renewable energy alternatives to meet this growing energy demand. The IEA has also projected that more than 13% of the increase in energy demand over this period is expected to be provided by renewable energy sources [1]. In cold climates like Canada, heating requires a significant portion of the total energy demand. According to National Resources Canada (NRCAN), as of 2008 the average commercial building consumes about 50% of its total heating requirement on space heating, which is primarily supplied through fossil fuels. Therefore, there is need to develop efficient and cost effective renewable energy systems for building heating applications. One emerging technology is the transpired solar air collector. It has a simple design concept that consists of installing a perforated, flat, or corrugated sheet metal in front of a building façade to create an approximately two dimensional channel for ambient air to flow. Incident sunlight on the wall causes it to heat up; this heat is transferred to ambient air in the channel that is then drawn into the building Heating Ventilation and Air Conditioning (HVAC) system to reduce the total load required to heat the supply air.

Solar air collectors of different geometries have been studied experimentally and numerically. Most of these studies were focused on the investigation of the thermal performance of flat plate solar air collectors with different configurations at various flow rates and solar irradiance to estimate the overall system efficiency [2-10]. These studies concluded that the overall performance was strongly dependent on many system variables including collector material [11], perforation size and spacing [2,3] flow rate [12], wind speed [4], channel depth [13], and

irradiation [5]. An asymmetry in the mean velocity profile across the channel has been reported [6-8], which was argued to enhance heat transfer [6]. There is also an agreement that the overall heat removal efficiency improves at higher flow rates [4,8,9]. These studies are all focused on evaluating the thermal performance of flat plate solar air collectors based on bulk parameters, which do not provide sufficient details on the underlying physical processes, which are essential for understanding the energy transfer efficiency of the system. The only experiment for corrugated plates was conducted by Gawlik [14] and this research was focused on the flow separation phenomena with sinusoidal shaped geometry.

Although there have been several studies describing the flow over a heated flat wall from the fundamental perspective, the flow dynamics and hence the associated heat transfer in the transpired air collector with a corrugated waveform is more complex than that over a flat surface. There are some studies describing the flow behaviour over a wavy wall however, they were conducted in the absence of wall heating. To the best of authors' knowledge there is no reported investigation of the flow behaviour in a channel with heating from the wavy wall. As the present study is focused on investigating the flow behaviour over a heated corrugation waveform, the literature review is split into two components: turbulent flows over wavy surfaces and channel flows over a heated surface.

Several studies investigated turbulent flow over smooth wavy surfaces in a 2D channel [15-20]. A common observation in all these studies was that the mean velocity profile was asymmetric with the peak velocity shifted away from the center towards the opposite flat wall. Another common observation was the enhancement of turbulent properties in the trough region due to the flow separation off the crest. The flow reattachment point was observed to vary non-monotonically with Reynolds number on the windward side of each wave [15]. The peak

production of turbulent kinetic energy occurred above the trough at a distance equal to the wave height [16,17].

In a 2D channel over a square waveform, a similar velocity profile was observed as flows over a sinusoidal surface. The momentum exchange between the local and bulk flows was seen to increase with both wavelength and Reynolds number. Maximum turbulent kinetic energies were observed above the reattachment point on the windward corner of the square wave [21,22].

Significant work has been done on forced and natural convection in differentially heated channels. It has been observed that the peak mean velocity shifted towards the heated wall [23-25], which is consistent with that observed in flat plate solar air collectors [7,8]. The wall heating induces buoyancy-driven secondary flow which increases mixing and thereby enhances the heat transfer to the fluid near the heated wall. For channel flow with one side wall heated and the opposite wall cooled, there is agreement that heat transfer is increased for large Grashof numbers [23, 26] where natural convection is the dominant mode of heat transfer. Radiation generated from the heated wall surface creates thermal instability between the fluid and the top and bottom channel walls and enhances heat transfer [26]. After the flow reaches its maximum kinetic energy ratio, it gradually decreases as the temperature of the flow grows and buoyancy forces decrease. The heat generated from the side walls rises and accumulates in the top of the channel creating a stratification that dampens the buoyancy [23]. A numerical study was conducted of a 2D vertical cavity with one side heated wall with buoyancy driven flow. Emitted radiation from the heated wall increases the temperature of the opposite insulated surface for laminar and turbulent buoyancy driven flows, but this only visibly affects the flow at laminar Reynolds numbers with the existence of two peak streamwise velocities near the boundaries [27]. Yilmaz and Fraser [28] conducted a numerical and experimental investigation measuring mean

velocities and turbulent kinetic energies of a turbulent natural convection in a vertical channel with one wall at constant temperature. Numerical and experimental results showed an increasing maximum mean velocity shifted towards the heated wall as the flow developed downstream. The turbulent kinetic energy profile is very erratic towards the inlet of the channel; the maximum magnitude not only decreases rapidly from the inlet and then steadily increases again to the end of the channel, but the location of the maximum turbulent kinetic energy shifts from the unheated wall at the inlet to the heated wall halfway down the channel, and then gradually moves to the core of the flow. Gajusingh and Siddiqui [25] studied the impact of wall heating on the initially turbulent and laminar channel flows. They reported that the addition of heat transitions a laminar flow into turbulent due to the buoyancy-induced turbulence. Conversely, in an initially turbulent flow, the addition of heat reduces the magnitude of turbulent properties due to the dampening of shear-produced turbulence as it interacts with the buoyancy forces.

As the literature review shows, there is a scarcity of studies investigating the influence of a heated waveform and the associated flow structure on convection. For the corrugated geometry of the transpired air collector considered in the present study, there are some studies that investigated its bulk thermal performance in practical applications [14, 29]. Belusko et al. [29] predicted the thermal efficiency increased of jet impingement on the channel flow moving parallel to the corrugations in a perforated corrugated air collector. The study showed the additional pressure losses required to produce an air jet through the perforations into the channel are a small factor for an increase in thermal performance. They also commented that it was necessary to determine the flow distribution in the air channel for local convection coefficients. Gogakis [30] conducted experiments on the commercial corrugated transpired air collector in the field with the collector corrugations mounted parallel with the air flow. The collector and air

temperatures were measured to calculate heat exchanger efficiency between the panel and the bulk air, and total energy savings. General results showed an increase in efficiency with air flow rate and incident irradiance with a maximum heat exchanger efficiency of 21%.

These studies have shown the promising potential of corrugated transpired air collectors, however there is no detailed study on the fundamental thermo-fluid interaction between the heated corrugation wall and airflow in the channel. Such understanding of these interactions and the flow characterization is vital to optimize the collector performance. We have recently conducted a detailed investigation of the flow structure in the corrugated transpired air collector to characterize the mean and turbulent flow behaviour in the absence of wall heating [31]. The results have shown that the corrugation waveform significantly alters both the mean and turbulent flow fields in the collector channel. The flow was observed to be oscillatory with respect to the waveform throughout most of the channel length. Turbulent property profiles show the enhancement of turbulence around the height of one waveform, in particular over the trough sections [31]. This presented study is the continuation of this work with the focus on the influence of corrugation wall heating on the mean and turbulent flow fields in the collector channel. Results can not only be applied to the implementation of transpired air collectors to optimize their performance, but also contribute to the understanding of the fundamental physical processes involved.

3.3 Experimental Setup

A full scale transpired air collector system was built for experiments to be conducted in a laboratory environment. A residential construction wall was built with dimensions 1.83 m long, 1.22 m wide and 0.1 m deep which was well insulated with R20 insulation and a vapor barrier.

A 1.3 cm thick plywood board was fixed to the external face of the construction wall, and a 1 cm drywall was attached to the opposite face. A commercial corrugated and perforated solar collector made of 18 gauge sheet metal of size 1.83 m \times 1.22 m was used. The material and geometry of the collector was the same as that used in real transpired air collector applications [30]. The corrugation amplitude (h) and wavelength (λ) are 3.5 cm and 15 cm, respectively. The surface of the sheet metal has triangular shaped (1.4 mm amplitude) perforations spaced 2.2 cm apart from their center (approximately 1.5% porosity). This transpired collector was mounted across the construction wall to create a channel with the corrugation waveform normal to the flow direction. The height of the channel (H) was defined as the distance from the mean corrugation height to the construction wall, which was 10.95 cm. The length of the channel (L) was 1.83 m (see Fig 3-1). The channel sides were sealed with Plexiglas sheets to allow optical access for measurement. The complete assembly was attached to a frame of dexion metal square tubing, which allowed the system to be modular to vary inclination angle and channel height for future experiments. The air flow through the channel was from the bottom to the top in the suction mode drawn by a 3 hp centrifugal fan (New York Blower Company) and controlled by a variable frequency drive.

Radiation heat was supplied to the solar collector by an array of 6 \times 6 60W Sylvania halogen light bulbs spaced evenly 20 cm apart. The temperature distribution was inspected using an infrared camera (FLIR SC4000); the exterior surface of the solar air collector was reasonably uniform with a maximum temperature variation within $\pm 1^\circ\text{C}$. The influence of side walls on the corrugation wall temperature uniformity was minimal and mainly restricted near the edges. The lighting array was mounted on a stand that allowed adjustment of the vertical position and angle the light could be directed. The lighting array was placed 70 cm from the solar air collector. A

voltage controller was used to vary the power input to the array. The experiments were conducted for two heating cases: 1450W and 2200W electrical power supply, which will be referred to as low (q_L) and high (q_H) heating conditions respectively.

For each heating case the lighting system was left active for several hours before measurements to reach steady state. During experiments, the external surface temperature of the corrugation wall was monitored and measured with the FLIR Infrared Camera. T-type thermocouples with the accuracy $\pm 0.5\%$ were placed throughout the channel to measure the bulk air inlet temperature, bulk temperatures immediately upstream and downstream of the measurement field, construction wall temperature in the measurement plane, and the outlet air temperature. The thermocouple data was acquired using NI-9211 data acquisition cards with LabVIEW software at a sampling rate of 2 Hz. The uniformity of the air temperature inside the channel at the given height was relatively constant ($\pm 0.8^\circ\text{C}$) over 90% of the channel depth. This confirmed the two dimensional nature of the flow.

Two dimensional instantaneous velocity fields over a complete waveform were obtained using Particle Imaging Velocimetry (PIV) at three locations along the channel length, $X/L = 0.41, 0.57, 0.80$, where X was measured from the inlet of the channel (see Fig 3-1). Measurements in the crest and following trough regions were taken separately to maintain high velocity field resolution. The crest region was defined between $x/\lambda = 0$ and 0.5 , while the trough region was bounded between $x/\lambda = 0.5$ and 1.0 , where x is the local coordinate measured from the base of the windward face of the corrugation (see inset in Fig 3-1). There was about a 20% overlap of the measurement domains for both the crest and trough. For each position, measurements were taken in the mid cross plane where the flow was two-dimensional. For each experimental run,

the data were collected 30 minutes after setting the desired flow rate allowing the flow and temperatures to reach steady state.

The PIV system comprised of a 120 mJ Nd:YAG pulse laser (SoloPIV 120XT) as the light source. A 1 cm slot was cut along the length of the construction wall and fitted with Plexiglas strips on both sides of the construction wall to allow optical access for the laser light sheet to reach measurement locations. A four megapixel CCD camera (Flare, IO Industries) with the resolution of 2336×1752 pixels was mounted horizontally to image the flow through the Plexiglas side wall. The field of view of the camera was about $15.3 \text{ cm} \times 11.5 \text{ cm}$. Eight-bit images were acquired using an image acquisition system (CoreView, IO Industries) at a rate of 30 Hz. A four channel delay generator synchronized with the camera was used to control the timing of the laser pulses.

Olive oil droplets with an average diameter of $1 \mu\text{m}$ were used as the tracer particles for the PIV measurements. The particles were introduced via a LaVision flow seeder using pressurized air. The homogeneous distribution of tracer particles is very crucial for the flow velocity computation using PIV. To generate homogeneous particle distribution in the flow, a 1-1/2 inch PVC pipe 110 cm in length was used as the particle distributor (see Greig et al. (2012)). The cylindrical plenum was located 5 cm underneath the channel inlet (Fig 3-1).

Data were collected for five flow rates at each measurement position along the axial length of the channel for both heating cases. For each case, 3000 images were acquired, which provided 1500 velocity fields. It was observed that the differences in the bulk mean streamwise velocities between the top, middle and bottom sections for each heating condition was very small. Thus the

bulk mean streamwise velocity in the middle section ($X/L = 0.57$) was considered as the reference velocity scale (U_B) for normalizing its corresponding heating condition.

Since the air density and viscosity varies with temperature, for a given fan RPM the Reynolds number differed for each heating condition. Therefore, Reynolds number cannot be used as the reference parameter when comparing different cases. The reference parameter that was consistent for heated and unheated cases was the fan RPM. Thus, the five flow rates which correspond to five fan RPM settings will be referred to as Cases, I, II, III, IV and V; where Case I represents the lowest flow rate while Case V represents the highest flow rate. As a reference range, an estimate of the Reynolds number range for the five cases at the unheated condition based on U_B and the channel height (h), are 530, 2030, 2675, 4140, and 6650.

Images were captured with a small aperture setting to minimize the noise from the reflected light for PIV data processing. Consequently, image brightness and contrast needed to be adjusted to improve the signal-to-noise ratio (SNR) and to improve the accuracy of the velocity vector computation using PIV technique. Thus an approach was used to rescale the gray values by a constant factor in the region away from the construction wall, while in both near wall regions the rescaling factor was linearly decreased to zero. This allowed an improved and almost uniform contrast between the particles and the background (see Greig et al. [31]).

The PIV velocity fields were calculated by cross-correlating interrogation windows (48×48 pixels in size) in the first image of an image pair, with the corresponding search windows (96×96 pixels in size) in the second image of the image pair. A 50% overlap interrogation windows was used, which provided a spatial resolution of 24×24 pixels, corresponding to a $1.6\text{mm} \times 1.6\text{mm}$ spatial resolution of the velocity field. The erroneous velocity vectors were detected and

corrected using a local median scheme based on the eight surrounding vectors [32] and a secondary scheme based on the time-averaged mean velocity and the relative to the global velocity direction (see Greig et al. [31]).

The total error in a PIV measurement is the sum of the errors from the seed particle diameter, seed density, velocity gradients, out of plane motion, the dynamic range, peak locking, and Adaptive Gaussian Window interpolation [33]. The uncertainty in the PIV velocity measurements was estimated based on the criteria and data presented in Cowen and Monismith [33] and Prasad et al. [34]. The uncertainty was computed at the highest flow rate and the high heat case, which has the largest velocity gradients of all cases. Thus, the errors are expected to be the largest in this case. The uncertainty in the PIV velocity measurements is estimated to be ± 0.29 cm/s which is less than 1% of the bulk flow velocity. Example error calculations are given in Appendix 1.

3.4 Results

For each case, temperatures were recorded for the entire duration of PIV velocity measurements. The temperatures of the transpired air collector (referred to as corrugation wall), bulk flow and construction wall were averaged in time and as well as over the channel length, which are presented in Table 1 for both heating conditions. As expected, all these temperatures were highest at the lowest air flow rate and decreased as the air flow rate increased. An interesting observation in the data is that the temperatures of the construction wall surface were higher than the bulk fluid temperature. This implies that the radiation heat transfer from the corrugation wall to the construction wall is significant. Furthermore, another contribution to the raise in temperature was due to the nearly adiabatic conditions created at the construction wall side from

the insulation. Therefore this temperature difference between the construction wall and the bulk fluid contributed to the convection heat transfer to the airflow. This phenomenon was also reported by Liao et al. [8]; they observed higher inner wall temperatures compared to the bulk flow temperatures in a vertical channel heated from an outer plane wall. The results in Table 1 also show that these temperatures increase with an increase in the incident radiant heat flux, as expected. The contribution of the heated construction wall to the total convection heat removed by air was estimated based on the heat transfer correlation for the convection adjacent to a plane vertical heated wall [35]. The results are presented in Table 2, which show that heat transfer from the construction wall constitutes 15-25% of the total heat gain by the airflow.

The largest percent increase in corrugation wall external temperature from the low heating to the high heating condition was comparable for the two lowest flow rates (Case I and II), which was approximately 18%. Additionally, the largest percent increase in average bulk flow temperature was also observed at the lowest flow rate (Case I), which was 13.5%. It was the construction wall that experienced the largest percent increase in temperature between the two heating conditions. For flow rate Cases I, II and III, the inner channel temperature of the construction wall increased 19-20%.

The total incident radiant heat flux on the transpired air collector was estimated based on the radiation incident on an infinite flat plane from a point source, which could theoretically absorb half of the radiation emitted by the point source [36]. Due to the finite size of the corrugation wall, a conservative estimate of 60% of the theoretical maximum of half the energy from the source was assumed as absorbed. This results with a final estimate of 30% of the radiation emitted by the array of bulbs was incident on the corrugation wall. The values of the approximated incident radiation on the corrugation wall are also presented in Table 1. The losses

from the corrugation wall to ambient air through convection and radiation were calculated and found to be less than 14.5W, which was considered to be negligible compared to the total incident radiation. The total heat transfer to air over the entire length of the channel was also computed and the values are presented in Table 2.

Instantaneous velocity fields were obtained using PIV. Mean velocity field for each case was computed by time-averaging the instantaneous velocity data at each grid point. Turbulent velocity fields were obtained by subtracting the time-averaged velocity from the instantaneous velocity at each grid point. Snapshots of the turbulent velocity fields in the crest and trough regions for Case I at the high heating condition are shown in figure 3-2. The plots show that the turbulent velocity fields are very dynamic and complex. The bulk flow separates off each crest and sheds vortices that move into both the downstream trough section and bulk flow. There also is an oscillatory behaviour in the flow which results in a non-monotonic reattachment point of the flow on the windward edge of each crest. It is apparent that there are several small-scale turbulent structures (vortices), originating from the trough and advecting downstream and interacting with the vortices in the channel core as well as the turbulent structures that originated off the construction wall. Such interactions resulted in an overall complex turbulent flow structure throughout the channel.

A detailed inspection of the turbulent velocity fields at unheated and both heated conditions show that the turbulent flow structure was quite similar for Cases III-V although the velocity magnitudes were dependent on the heat flux. The turbulence intensity increased with an increase in the wall heat flux. At the two lower flow rates (Cases I and II), the structure in turbulent flow was different near the corrugation wall in the presence and absence of heating. It was observed that heating induced stronger velocities and velocity gradients close to the corrugation wall side

of the channel. Turbulence enhances mixing and hence the transport of heat. Thus, the enhancement of turbulence by the corrugation wall further contributed to the effective transfer of heat from the wall to the air flow.

The streamwise (u) time-averaged velocity data across the channel height was plotted at different wave phases for all flow rates in figure 3-3a at the high heat flux condition. The plot shows that in general the normalized mean velocity magnitudes are comparable in the bulk flow region of the channel ($1.9 < y/h < 3.1$) and in the immediate vicinity of the trough. A significant variation in the normalized values was observed in the region $0.5 < y/h < 1.5$ for each flow rate. It was found that the normalized magnitude of mean velocity increased monotonically with a decrease in the flow rates in this region. This implies that the heat addition has a stronger effect on the velocity magnitude at the lower flow rates. The location of the peak velocity magnitude was also seen to vary with the flow rate. At the highest flow rate (Case V), the peak velocity was located in the bulk flow region tending towards the construction wall side. However, as the flow rate decreases the peak shifts towards the corrugation wall to a well defined peak.

The mean velocity profiles at the three channel measurement positions across the length of the channel were also compared over the waveform. At a given condition, the velocity profiles collapsed into a very narrow band indicating that the flow was periodic over each waveform of the collector, in other words the flow structure and velocity repeat over each complete waveform down the channel length.

To study the impact of corrugation wall heating on the mean flow behaviour inside the channel, the mean velocity profiles at the middle section of the channel for the unheated and two heated cases are plotted in figures 3-3b and 3-3c at the lowest and highest flow rates (Cases I and V),

respectively. The plots show that the mean velocity profiles at both heating conditions and at all wave phases collapsed into a very narrow band, indicating that, comparing the given heat flux inputs, they do not have a significant impact on the magnitude or structure of the mean velocity field in the channel. Similar trends are observed at all examined flow rates. However, the plot shows that depending on the flow rate, the heat flux could influence the mean flow magnitude and structure. This effect is stronger at the lowest flow rate, but diminishes at the highest flow rate. At the lowest flow rate (figure 3-3b), the mean velocity in the absence of heat is relatively uniform throughout the channel height compared to the heated cases. The results show that wall heating not only increased the overall magnitude of the mean velocity but also altered the shape of the velocity profile. It was observed that the heating produced two enhanced mean velocity regions across the channel: A stronger and wider region of enhanced mean velocity near the corrugation wall, and another lesser enhancement region near the construction wall. This enhancement of velocity was due to the wall heating effects which occurred at both walls, however, the greater enhancement near the corrugation wall was a result of the higher corrugation wall temperature. It was observed that the mean velocity magnitude increased by a factor of 3 and 5 due to wall heating near the corrugation and construction walls, respectively for the lowest flow rate. It should be noted that in the absence of heating, the peak mean velocity was located closer to the construction wall [31]. As the flow rate increased, the relative enhancement of the mean velocity magnitude due to wall heating decreased and became almost negligible at the highest flow rate. This is likely due to the decrease in the wall temperatures with the flow rates (see Table 1).

Figure 3-4a shows the Root-Mean-Square (RMS) streamwise (u) turbulent velocity profiles at different wave phases for all flow rates (Cases I-V) at the high heat flux condition. The plot

shows that the RMS streamwise turbulent velocity magnitudes are higher in the vicinity of the corrugation wall compared to the construction wall with the largest peak enhancement above the crest. It was observed that the velocity magnitudes are relatively uniform in the bulk flow region. The most significant overall enhancement in the velocity magnitude was observed in the trough region. An interesting feature in the plot was that the normalized velocity profiles collapsed well in the bulk flow region at all flow rates except at the lowest flow rate (Case I), where, in general, the average RMS values were a factor of 2 greater than the higher flow rates across the bulk flow in the channel. The results also show that in the trough region within almost one wave height, the magnitude of the RMS streamwise velocity increased monotonically with a decrease in the flow rate. It is also observed that in general, the location of the peak velocity magnitude shifted towards the trough with a decrease in the flow rate. The peak velocity magnitudes in the trough region at the lowest flow rate (Case I) are 50% higher than the next highest at Case II. The average RMS streamwise turbulent velocity in the close vicinity of the corrugation waveform ($0 < y/h < 1.5$) is approximately 25% larger than that in the vicinity of the construction wall ($y/h > 3$).

When comparing the streamwise turbulent velocity profiles at the top, middle, and bottom locations along the channel length, they were well periodic over each waveform at any given condition.

The RMS streamwise turbulent velocity profiles at the middle section of the channel for the unheated and two heated cases are plotted in figures 3-4b and 3-4c at the lowest and highest flow rates (Cases I and V), respectively. In figure 3-4b, it can be seen that heating significantly increases streamwise turbulent velocities across the entire channel. Although there was very minimal change in streamwise RMS magnitude for this Case, there was a slight peak observed at

the height just above the waveform crest ($y/h = 1.2$), which then slightly decreases to a local minimum at the core of the bulk flow, and begins to increase again near the construction wall. The peak is more intense directly over the crest compared to over the trough. Streamwise RMS values also decrease from the peak in the trough region, but it was still apparent that there was enhanced streamwise turbulent velocities in this region with heating. Both heating conditions provided very similar streamwise RMS magnitudes, indicating that the relative increase in heating from the low to high condition enhanced streamwise turbulent velocities marginally. The streamwise RMS values were an average of 4.5 times larger in the heating cases versus the unheated condition. At the highest flow rate (Case V) shown in figure 3-4c, both heating conditions and the unheated condition collapse very well, signifying that heating contributes very little to streamwise turbulent enhancement at the higher flow rates. There are two peaks of approximately equal magnitude: the first located at $y/h = 3.4$ near the construction wall, and the other at $y/h = 1.1$ above the corrugation wave height. The streamwise RMS turbulent velocity from the first peak at the construction wall decreases relatively sharply in the bulk flow, and then gradually increases again to the second peak at the corrugation wave height. Streamwise RMS values then steadily decrease to near zero in the trough section. The peak streamwise turbulent velocity magnitude at the waveform crest was an average of 20% larger than the peak observed at the construction wall between $0 < x/\lambda < 0.7$, while over the other waveform section, both peak magnitudes were within 5% of each other.

Figure 3-5a shows the RMS cross-stream (v) turbulent velocity profiles at different wave phases for all flow rates (Cases I-V) at the high heat flux condition. The plot shows trends similar to that of the RMS streamwise turbulent velocity. The cross-stream turbulent velocity magnitudes are highest in the vicinity of the corrugation wall with a relatively uniform magnitudes in the

bulk flow region and slight enhancement in the trough region ($0.75 < y/h < 1$). Similar to the streamwise turbulent velocities, the normalized magnitudes of the cross-stream turbulent velocities are quite comparable at all flow rates except the lowest flow rate. In general, the RMS cross-stream magnitudes at the lowest flow rate were approximately 2.2 and 2.8 times higher, in the trough and crest respectively, than those at the higher flow rates. However, although the normalized magnitudes are comparable, there was larger region of local enhancement in the trough for cross-stream turbulent velocity profiles at as compared to streamwise turbulent velocities.

The RMS cross-stream turbulent velocity profiles at the top, middle and bottom locations along the channel length were also compared over the waveform at all flow rates and both heating conditions. It was observed that in general, the profiles at different waveforms collapsed relatively well however, in some cases, the RMS cross-stream velocity magnitude was higher in the trough region furthest downstream location, while the higher velocity magnitude was located in bulk flow region in the upstream section of the channel. These results indicate that the cross-stream turbulent velocity was not as periodic as the streamwise turbulent velocity.

The RMS cross-stream turbulent velocity profiles at the middle section of the channel for the unheated and two heated cases are plotted in figures 3-5b and 3-5c at the lowest and highest flow rates (Cases I and V), respectively. The impact of the incident heat flux was most apparent at the lowest flow rate; the cross-stream turbulent velocity magnitudes increased with the heat flux at the lowest flow rate. The enhancement of turbulence due to wall heating was also observed to be more profound in the trough region. The normalized magnitudes of the RMS cross-stream turbulent velocity were approximately 6 times higher in both the bulk and trough region due to

wall heating. The results also show that the relative increase in the cross-stream turbulent velocity magnitude at different incident heat fluxes is stronger above the crest.

Comparison of the magnitudes of the RMS streamwise and cross-stream turbulent velocities shows that overall the streamwise normalized turbulent velocity magnitudes are 50% and 20% higher than the cross-stream velocity magnitudes at the highest heating condition at the lowest and highest flow rates (Case I and V) respectively. In the trough region, the streamwise normalized RMS values are 8% and 45% larger than the cross-stream, and in the bulk region, they are 75% and 43% larger at the lowest flow rate and the highest flow rate respectively. The streamwise and cross-stream turbulent velocities have a relatively consistent difference at the highest flow rate in the trough and bulk flow regions partially because the shape of their profiles are very similar. The most comparable normalized RMS turbulent velocities between the streamwise and cross-stream flows were observed in the trough region at the lowest flow rate.

Figure 3-6a shows the Reynolds stress ($-\overline{u'v'}$) profiles at different wave phases for all flow rates (Cases I-V) at the high heat flux condition. The plot shows enhanced Reynolds stress in the trough region at all flow rates, which decreased to approximately zero in the bulk region as well as the trough boundary. However, this trend was different at the lowest flow rate; the Reynolds stress magnitudes are strongest in the trough region, which decreased away from the waveform and became negative in the bulk region. It then approached zero again towards the construction wall. Note that the negative Reynolds stress magnitude decreased with an increase in the flow rate and for Cases III to V the negative Reynolds stress magnitude was negligible. The observation of the negative Reynolds stress will be discussed in the following section.

A brief examination of the Reynolds stress profiles at the top, middle and bottom locations along the channel length over the waveform at both heating conditions showed that there was little to no negative Reynolds stress at the lowest flow rate towards the bottom of the channel length, but it became negative between $1 < y/h < 2.5$. By the highest flow rate there was little variation in the magnitudes of the Reynolds stress profiles, indicating that the flow became periodic across each waveform at the higher flow rates.

The Reynolds stress profiles at the middle section of the channel for the unheated and two heated cases are plotted in figures 3-6b and 3-6c at the lowest and highest flow rates (Cases I and V), respectively. Similar to earlier observations, the impact of wall heating on the Reynolds stress is profound at the lowest flow rate, which decreases with the flow rate to become almost insignificant at the highest flow rate. Figure 3-6b shows in the absence of heating, the Reynolds stress remains positive throughout the channel and the negative Reynolds stress is observed at both heating conditions. This indicates that the manifestation of the negative Reynolds stress is related to the heat addition from the corrugation wall. The plot in figure 3-6b also shows in the absence of heating, the location of the peak Reynolds stress was in the trough region at approximately one wave height. However, with the heat addition, the Reynolds stress peak shifted towards the trough wall up to the mid-trough location ($x/\lambda = 0.75$) and then it started to shift away from the wall.

3.5 Discussion

The presented results show that the heating from the corrugation wall could have a significant effect on the structure and magnitude of both mean and turbulent velocities depending on the air flow rate. It was observed that at high flow rates (Case IV and V), the structure and magnitude

of mean and turbulent velocities are quite comparable across unheated, low heating, and high heating conditions. However, as the flow rate was reduced, the applied heat flux not only produced greater velocities compared to the unheated flow but also affected the overall structure (figure 3-3b and 3-4b). Although the Reynolds number at this flow rate is well within the classical laminar range, Greig et al. [31] have shown that instabilities caused by the corrugation geometry led to the transition of the flow to turbulence. The results show that the turbulence became significantly stronger in the presence of heating at this flow rate, which was likely due to buoyancy-induced instabilities creating an additional source of turbulence. When the air parcels in the channel come in contact with the heated corrugation wall, they form thermal plumes because of the decrease in density. The interaction of these plumes with each other and with the bulk flow resulted in a complex flow structure comprised of vortices, shear layers and bursting and sweeping motions as depicted in figure 3-2. Bursting is referred to as the general motion of the turbulent flow ejecting from a surface, while sweeping is defined as the flow moving towards and into a surface. The channel flow is mixed convection, with the combination of natural convection from the heated wall and forced convection from the suction fan. As a result, both inertia and buoyancy forces contribute to the convection heat transfer. The relative contribution of inertia and buoyancy forces can be quantified in terms of the Grashof-to-Reynolds number ratio (Gr/Re^2). The buoyancy effects are dominant if $Gr/Re^2 > 1$ [35]. The values of Gr/Re^2 are presented in Table 2. As expected, this ratio grew with a decrease in the flow rate and was highest at the lowest flow rate. This implies that the flow is primarily driven by buoyancy for the lower flow rates; thus, the buoyancy-induced instabilities act as a major source of turbulence compared to that at the higher flow rates.

The results in figures 3-3b, 3-4b and 3-5b also show that the flow structure at the lowest flow rate was affected mainly in the vicinity of the corrugation, where the velocity magnitudes were relatively enhanced. The enhancement region where the thermal plumes were stronger and more frequent was observed in between $1 < y/h < 1.5$ above the crest, and between $0.5 < y/h < 1.2$ above the trough region. As the thermal plumes are also advecting in the same direction as the bulk flow, they contributed to the increase in the mean velocity. The construction wall also had a higher temperature relative to the flow, thus plumes were also generated from the plane wall as well, which locally increased the mean velocity magnitude near the construction wall as seen in figure 3-3b. The enhancement of turbulent velocities above the crest was likely due to the strong interaction between the plumes and the bulk flow. Similarly, above the trough, this region corresponds to the zone where interactions between the plumes originating inside the trough would be most intense and as a result, the turbulent velocities increase.

The comparison of the streamwise and cross-stream turbulent velocities at the lowest flow rate (figures 3-4b and 3-5b) shows, in general, the streamwise turbulent velocities are stronger and relatively uniform across the channel excluding the crest. The cross-stream turbulent velocity magnitudes were stronger in the trough of the corrugation and decreased gradually towards the construction wall. This is likely an effect of the source of the plumes and movement of the plumes relative to the corrugation geometry.

At the higher flow rates, the structure and magnitude of mean and turbulent velocities were comparable for unheated and both heated conditions, which demonstrates the incident heat flux did not contribute to the further enhancement of turbulence. These high flow rates fall in the classical turbulent flow regime based on their Reynolds number, which implies that the flow was turbulent regardless of the geometry. Greig et al. [31] have shown that the presence of the

corrugation waveform enhanced the magnitudes of turbulent velocities compared to that at a plane smooth wall. Thus, a plausible explanation for the observed trends is the contribution of buoyancy to the turbulence generation at high flow rates was not significant compared to the generation from the mean shear flow. This was confirmed by the Gr/Re^2 values in Table 2. At the higher flow rates (Case IV and V), Gr/Re^2 was significantly less than one, which implies that the inertial effects were dominant.

The relative magnitudes of the mean and turbulent velocities were also affected by a change in flow rate for a given incident heat flux condition (figure 3-3a, 3-4a, and 3-5a). It was also observed that increasing the flow rate shifted the location of the peak mean velocity away from the corrugation waveform. Greig et al. [31] have shown that in the absence of heat, the location of the peak mean velocity in the channel was located in the bulk flow closer to the construction wall. As previously stated, although the buoyancy-induced thermal plumes contributed to an increase in the mean velocity near the corrugation wall, these effects diminished with an increasing flow rate. Therefore, the normalized mean velocity close to the corrugation wall decreased and the location of the peak mean velocity shifted towards the construction wall to where the peak mean velocity will be in an unheated channel. In fact at the highest flow rate, the location of the peak velocity magnitude for the heated condition was almost identical as seen for the unheated condition [31].

When comparing the normalized mean velocities in Figure 3-3a, they are almost identical, excluding the lowest flow rate, which shows an interesting deviation. Case I at the high heating condition shows the largest relative velocities at both boundaries of the bulk flow with a slight decrease in velocity in the middle of the bulk region compared to the other normalized flow rates. It was noted, the thermal plumes contributed to the increase in the velocity near both walls due to

the higher wall temperatures relative to the flow. However, the local increase of mean velocity near the construction wall was not observed at other flow rates even with the higher wall temperature, but instead they decreased towards the construction wall such as the standard channel flows. The mean velocity enhancement near the construction wall at the lowest flow rate further supports that the buoyancy effects dominate this flow. In order to satisfy mass conservation, an increase in the velocity in one region must be balanced by a decrease in the velocity in another region. At high flow rates, the increase in the mean velocity magnitude near the corrugation wall is balanced by a decrease in the velocity at the construction wall. However at the lowest flow rate, the mean velocity increased at both walls; thus, to satisfy mass conservation, the mean velocity must decrease in the middle of the bulk region.

The plots in figures 3-4a and 3-5a show that the influence of the flow rate on turbulent velocity magnitudes is stronger in the vicinity of the corrugation wall ($0.5 < y/h < 1.5$) as compared to the bulk of the channel. In general, while the normalized RMS streamwise turbulent velocity was reasonably uniform across the channel, the cross-stream RMS magnitude was stronger near the corrugation wall and decreased towards the construction wall. Both normalized turbulent velocities had increasing magnitudes with a decrease in the flow rate with the relative increase in the turbulent intensity greatest at the lowest flow rate (Case I). This was likely due to the relatively large contribution of buoyancy-induced turbulence and it can be argued that this contribution of buoyancy to the turbulence generation is substantial when the flow rate falls within the conventional laminar range without heating.

Another common feature in both streamwise and cross-stream turbulent velocity plots (figures 3-4a and 5a) was the effect of the flow rate on changing the structure and magnitudes was greater in the trough region compared the crest. The flow above the crest was primarily inertia driven

and turbulence was produced by shear; the influence of thermal plumes originating from the crest surface (i.e. buoyancy-induced turbulence) was suppressed. The only exception was the lowest flow rate, which was primarily driven by buoyancy and, hence, the influence of the thermal plume was significant, as mentioned earlier. The flow separates off each crest and loses energy due to this separation. Thus the trough was of low-energy separated flow and the inertial effects, including shear-induced turbulence, were relatively weak. Thus, the relative influence of the inertial effects in the trough region was more distinct with respect to the flow rate compared to above the crest. Due to these weaker inertial effects, the buoyancy induced plumes and turbulence have a relatively strong contribution to the turbulent velocities in this region. Thus, the variation in the turbulent velocities in this region with the flow rate is more distinct.

The profiles in figures 3-6b and 3-6c show that wall heating also influences both the magnitude and structure of the Reynolds stress. Although there were noticeable affects of heating at the highest flow rate (Case V) than observed in the mean and turbulent velocities, the influence of heating was still relatively weak. The most substantial effect was again observed at the lowest flow rate. For instance, the Reynolds stress magnitude was increased by one to two orders of magnitude in the trough region. Another interesting observation at the lowest flow rate was the presence of negative Reynolds stress towards the corrugation side of the bulk domain. Note that the negative Reynolds stress was observed only at the lowest flow rate, which implies that its manifestation was related to strong buoyancy-induced effects. By convention, the positive Reynolds stress ($-\overline{u'v'}$) is responsible for the momentum transport by the turbulent velocity field [37]. The strong magnitudes of positive Reynolds stress in the vicinity of the corrugation wall indicates a strong momentum transfer by the turbulent velocity field, which resulted in an overall enhancement of turbulence across the channel. After comparing figures 3-3b, 3-4b, and

3-5b, the negative Reynolds stress was considered not to have a direct influence on the turbulent velocities in this region. A comparison of figures 3-3 and 3-6 shows that the region of negative Reynolds stress somehow coincides with the region of mean flow deceleration. Thus, a plausible interpretation of negative Reynolds stress would be that the turbulence momentum was utilized to reduce the mean velocity towards the middle of the bulk flow.

The surface temperatures of the transpired air collector for the given incident heat flux conditions were within the expected range for transpired air collectors under realistic conditions [30]. As the heat flux increased from 530 to 793 W, the corrugation surface temperature, bulk flow temperature and construction wall surface temperature increased on average by 19%, 11%, and 18%, respectively. The corrugation surface temperature decreased by a maximum of 8 degrees Celsius between lowest and highest flow rates.

As expected, the highest transpired air collector, bulk air, and construction wall surface temperatures were observed at the lowest flow rates (Table 1). At the lowest flow rate (Case I), when the air velocity is slowest, heat transfer was primarily through natural convection as previously discussed. While at the higher flow rates, where heating effects are minimal on the mean velocity, the heat transfer mode shifts to forced convection, evident by the Gr/Re^2 ratio in Table 2. The total heat removed from the channel walls by the air is also given in table 2, which shows that the rate of heat removal was slowest at the lowest flow rate resulting in higher corrugation wall, bulk air, and construction wall temperatures. Conversely, forced convection at the highest flow rate removed the most amount of heat and temperatures were at their lowest. Based on the estimated incident heat flux on the transpired air collector, the thermal efficiency was calculated. At the high heat flux condition, efficiencies ranged from 20% to 70%, at the lowest to highest flow rates, respectively. The efficiency range was lower at the low heat flux

condition, which was between 16% and 52% for the lowest and highest flow rates again, respectively.

There was a consistent trend of trough temperatures being slightly higher than crest temperatures at all flow rates. Although the trough sections were slightly closer to the radiation heat source, it is more probable that the increased temperatures in the trough region were due to the lower velocities in the trough section as compared to the crest section as seen in the mean velocity profiles (figure 3-3). The bulk flow was responsible for removing heat from the crest and thus the higher velocities above the crests removed more heat than the trough and decreased crest temperatures the most. The higher temperatures in troughs as compared to that at the crests were also observed by Paio [38].

The present study investigated the mean and turbulent airflow structure inside the transpired solar air collector channel and the associated heat transfer characteristics. The influence of the wall heating on the flow structure was heavily dependent on the airflow rate. In the trough sections and around approximately one wave height, the normalized magnitudes of mean and turbulent velocities were largest at the lowest flow rate, which decreased with an increase in the flow rate. This indicates that the relative enhancement of mean and turbulent velocities was higher at the lower flow rates due to the larger contribution of the buoyancy-induced flow. The results also showed that the corrugation waveform was a major source of turbulence, which played an important role in the heat transfer to the bulk flow. Another significance of the corrugation geometry is the increase in the surface area compared to the flat plate collector, which further contributes to the heat transfer. It can be concluded that the corrugation geometry plays an important role in influencing the overall thermal efficiency of the air collector.

3.6 Conclusion

A PIV experimental investigation on the air flow behaviour in a transpired air collector channel under different heating condition was conducted. Mean and turbulent velocities as well as Reynolds stresses were computed. The incident radiation heat flux, in general, enhanced the mean and turbulent velocities as compared to the unheated flow in the same channel. As the flow rate increases the structure and magnitudes of the mean and turbulent properties shift towards those observed in the unheated channel flow. At high flow rates, the flow is dominated by forced convection while, at the lowest flow rate, the effects of heating are greatest and flow is primarily buoyancy driven. The buoyancy induced instabilities are large at this flow rate and relative enhancement of mean and turbulent properties is large compared to the unheated flow. The influence of heating on the lowest flow rate did not only enhance the overall magnitudes of mean and turbulent velocities, but also the structure in the vicinity of the corrugation waveform, in particular in the trough section. The thermal plumes generated from both walls locally increased the mean velocity. The low velocities in the trough suggest that turbulence enhancement is primarily generated due to buoyancy, which is also responsible for the higher trough collector surface temperatures. There was radiation heat transfer from the heated corrugation wall to the construction wall that not only increased the construction wall temperature but also contributed 15-25% of the total heat gain of the air. Collector efficiencies were as high as 70%, which could be attributed to the corrugation surface geometry that not only enhanced turbulence but also provided a larger heat transfer surface area.

3.7 Acknowledgements

Authors would like to acknowledge Natural Sciences and Engineering Research Council of Canada (NSERC), the Canadian Solar Buildings Research Network (SBRN) and the University of Western Ontario for providing the support.

3.8 References

- [1] Organisation for Economic Co-operation and Development/International Energy Association. World Energy Outlook 2011, (2011).
- [2] M. A. Leon, S. Kumar, Mathematical modeling and thermal performance analysis of unglazed transpired solar collectors, *Solar Energy* 81 (2007) 62–75.
- [3] S. Motahar, A. A. Alemrajabi, An Analysis of Unglazed Transpired Solar Collectors Based on Exergetic Performance Criteria, *Int. J. Thermodynamics* 13 (4) (2010) 153-160.
- [4] C. F. Kutscher, C. B. Christensen, G. M. Barker, Unglazed Transpired Solar Collectors: Heat Loss Theory, *J. of Solar Energy Engineering* 115 (1993) 182-188.
- [5] C. Yildiz, I. T. Torgrul, C. Sarsilmaz, and D. Pehlivan, Thermal efficiency of an air solar collector with extended absorption surface and increased convection, *Int. Comm. Heat Mass Transfer* 29 (6) (2002) 831-840.
- [6] L. H. Gunnewiek, E. Brundrett and K. G. T. Hollands, Flow Distribution in Unglazed Transpired Plate Solar Air Heaters of Large Area, *Solar Energy* 58, (4-6) (1996) 221-237.
- [7] E. Bacharoudis, M. Gr. Vrachopoulos, M. K. Koukou, D. Margaris, A. E. Filios, S. A. Mavrommatis, Study of the natural convection phenomena inside a wall solar chimney with one wall adiabatic and one wall under a heat flux, *Applied Thermal Engineering* 27 (2007) 2266–2275.
- [8] L. Liao, A. K. Athienitis, L. Candanedo, K.-W. Park, Y. Poissant, M. Collins, Numerical and Experimental Study of Heat Transfer in a BIPV-Thermal System, *J. of Solar Energy Engineering* 129 (2007) 423-430.
- [9] M. N. Metwally, H. Z. Abou-Zian, and A.M. El-Leathy, Performance of Advanced Corrugated-Duct Solar Air Collector Compared with Five Conventional Designs, *Renewable Energy* 10 (4) (1997) 519-537.
- [10] N. Hatami, M. Bahadorinejad, Experimental determination of natural convection heat transfer coefficient in a vertical flat-plate solar air heater, *Solar Energy* 82 (2008) 903–910.

- [11] P.T. Tsilingiris, Heat transfer analysis of low thermal conductivity solar energy absorbers, *Applied Thermal Engineering* 20 (2000) 1297-1314.
- [12] N. M. Khattab, Evaluation of perforated plate solar air heater, *Int. J. Solar energy* 21 (2000) 45-62.
- [13] D. Njomo and M. Daguinet, Sensitivity analysis of thermal performances of flat plate solar air heaters, *Heat Mass Transfer* 42 (2006) 1065–1081.
- [14] K. M. Gawlik, A numerical and experimental investigation of heat transfer issues in the practical utilization of unglazed, transpired solar air heater, PhD thesis, Department of Civil, Environmental and Architectural Engineering, University of Colorado Boulder, 1995.
- [15] M. Breuer, N. Peller, Ch. Rapp, and M. Manhart, Flow over periodic hills – Numerical and experimental study in a wide range of Reynolds numbers, *Computers and Fluids* 38, (2009) 433.
- [16] J. D. Hudson, L. Dykhno, and T. J. Hanratty, Turbulence production in flow over a wavy wall, *Exp. Fluids* 20 (1996) 257.
- [17] N. Shaikh and K. Siddiqui, An experimental investigation of the near surface flow over air-water and air-solid interfaces, *Phys. Fluids*. 22 (2010) 025103.
- [18] J. D. Kuzan, T. J. Hanratty and R. J. Adrian, Turbulent flows with incipient separation over solid waves, *Exp Fluids* 7 (1989) 88.
- [19] R. J. Calhoun and R. L. Street, Turbulent flow over a wavy surface' Neutral case, *J. Geophys. Res.* 106 (2001) 9277.
- [20] N. Kruse, S. Kuhn, and P. R. V. Rohr, Wavy wall effects on turbulence production and large-scale modes, *J. Turbul.* 7 (31) (2006).
- [21] H. Stel, R.E.M. Morales, A.T. Franco, S.L.M. Junqueira, R.H. Erthal, M.A.L. Gonçalves, Numerical and Experimental Analysis of Turbulent Flow in Corrugated Pipes, *J. Fluids Eng.* 132 (2010) 071203.
- [22] S. Eiamsa-ard, P. Promvong, Numerical study on heat transfer of turbulent channel flow over periodic grooves, *Int. Comm. in Heat and Mass Transfer* 35 (2008) 844-852.
- [23] J.J.M. Sillekens, C.C.M. Rindt, A.A. van Steenhoven, Development of laminar mixed convection in a horizontal square channel with heated side walls, *Int. J. of Heat and Fluid Flow* 19 (1998) 270.
- [24] T.A.M. Versteegh and F.T.M. Nieuwstadt, Turbulent budgets of natural convection in an infinite, differentially heated, vertical channel, *Int. J. of Heat and Fluid Flow* 19 (1998) 135.

- [25] S. T. Gajusingh and M.H.K. Siddiqui, The influence of wall heating on the flow structure in the near-wall region, *Int. J. of Heat and Fluid Flow* 29 (2008) 903.
- [26] T. T. Chandratilleke, R. Narayanaswamy, and P. Wangdhamkoom, Convective heat transfer in airflow through a duct with wall thermal radiation, *Materials Science and Engineering* 10 (2010).
- [27] B. Moshfegh and M. Sandberg, Investigation of fluid flow and heat transfer in a vertical channel heated from one side by PV elements, *World Renewable Energy Congress* 248 (1996).
- [28] T. Yilmaz, S. M. Fraser, Turbulent natural convection in a vertical parallel-plate channel with asymmetric heating, *Int. J. Heat and Mass Transfer* 50 (2007) 2612–2623.
- [29] M. Belusko, W. Saman, F. Bruno, Performance of jet impingement in unglazed air collectors, *Solar Energy* 82 (2008) 389–398.
- [30] C. Gogakis, Theoretical and experimental analysis of Solarwall® technology, Master's Thesis, School of Construction Management and Engineering, The University of Reading, UK, 2005.
- [31] D. Greig, K. Siddiqui, and P. Karava, An experimental investigation of the flow structure over a corrugated waveform in a transpired air collector, *Int. J. Heat and Fluid Flow* (2012) Unpublished results.
- [32] M. H. K. Siddiqui, M. R. Leowen, C. Richardson, W. E. Asher, and A. T. Jessup, Simultaneous particle image velocimetry and infrared imagery of micro-scale breaking waves, *Phys. Fluids* 13 (2001) 1891.
- [33] E. A. Cowen, S. G. Monismith, A hybrid digital particle tracking velocimetry technique, *Exp. Fluids* 22 (1997) 199.
- [34] A. K. Prasad, R. J. Adrian, C.C. Landreth, and P. W. Offutt, Effect of resolution on the speed and accuracy of particle image velocimetry interrogation, *Exp. Fluids* 13 (1992) 105.
- [35] F. Incropera, D. Dewitt, T. Bergman, A. Lavine, *Fundamentals of heat and mass transfer*, sixth ed., John Wiley & Sons, 2007, pp. 402-532.
- [36] I. Martinez, *Heat Transfer and Thermal Radiation Modelling*, Universidad Politecnica Madrid (2012) 31.
- [37] S. B. Pope, *Turbulent Flows*, Cambridge University Press, 2000.
- [38] Y. Paio, Natural, forced and mixed convection in a vertical cross-corrugated channel, Master's thesis, Faculty of Mechanical Engineering, University of British Columbia, 1992.

3.9 Tables

Table 3-1: Position and time averaged temperatures for the solar wall system in degrees Celsius.

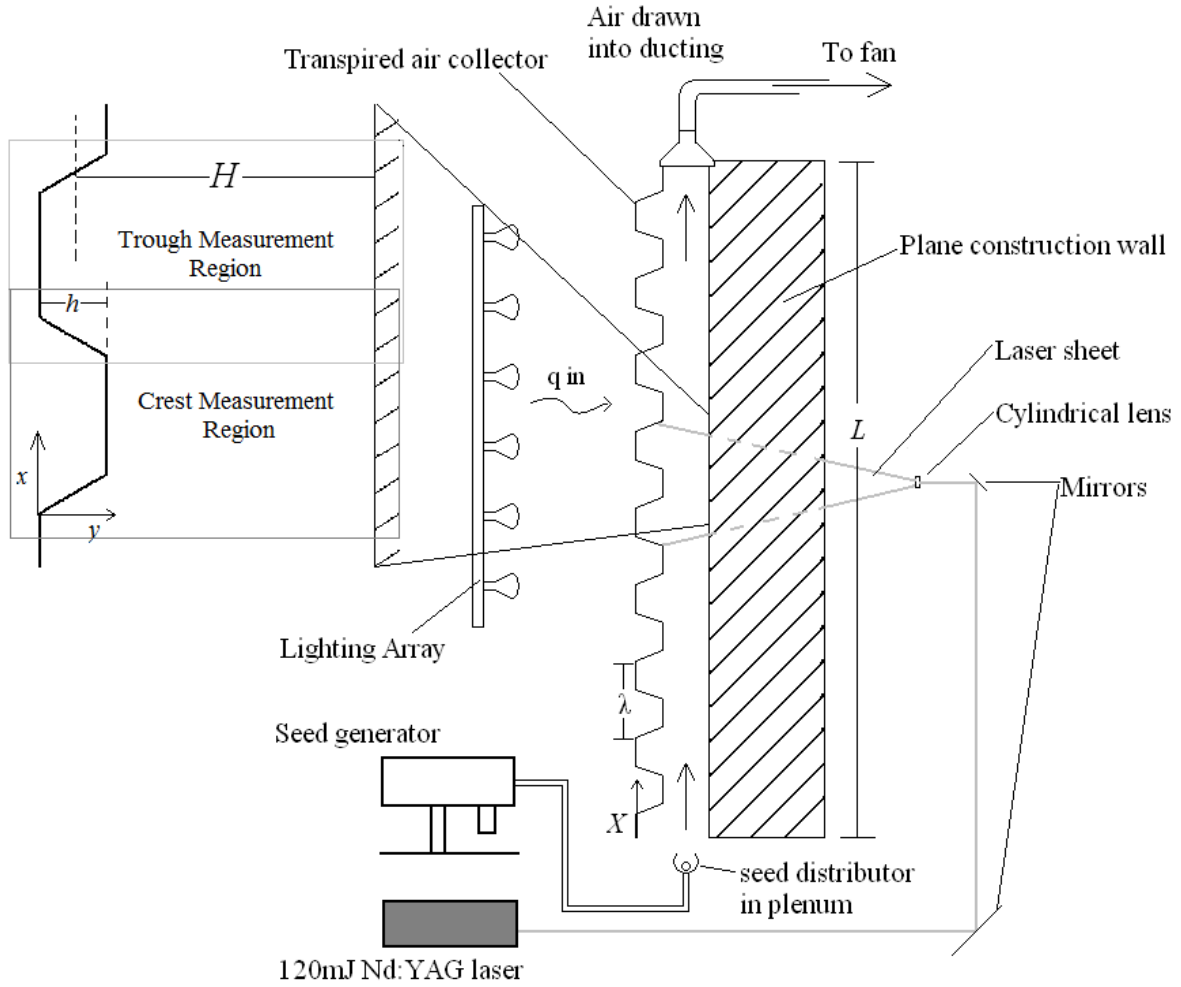
	Case	Solar Air Collector (°C)	Average Bulk Flow (°C)	Construction Wall (°C)
Low heating (530W)	I	44.70	28.09	32.38
	II	44.08	26.72	32.21
	III	43.48	26.93	32.51
	IV	41.38	26.35	30.90
	V	39.00	25.51	28.50
High heating (793W)	I	53.38	31.88	38.64
	II	52.98	29.93	38.65
	III	52.04	29.44	38.66
	IV	49.12	28.84	36.16
	V	45.44	28.22	32.92

Table 3-2. Calculated heat transfer values within the solar wall system.

Case	Low heat (530W)				High heat (793W)			
	Bulk Heat Removed Q_{flow} (W)	Construction Wall q_{conv} (W)	Grashof Number	$\frac{Gr}{Re^2}$	Bulk Heat Removed Q_{flow} (W)	Construction Wall q_{conv} (W)	Grashof Number	$\frac{Gr}{Re^2}$
I	88	17	2.81×10^6	1.93	146	23	3.46×10^6	2.24
II	125	33	2.94×10^6	0.60	182	43	3.83×10^6	0.89
III	162	41	2.80×10^6	0.29	229	63	3.75×10^6	0.39
IV	230	29	2.54×10^6	0.10	340	42	3.37×10^6	0.14
V	278	44	2.28×10^6	0.04	460	64	2.86×10^6	0.05

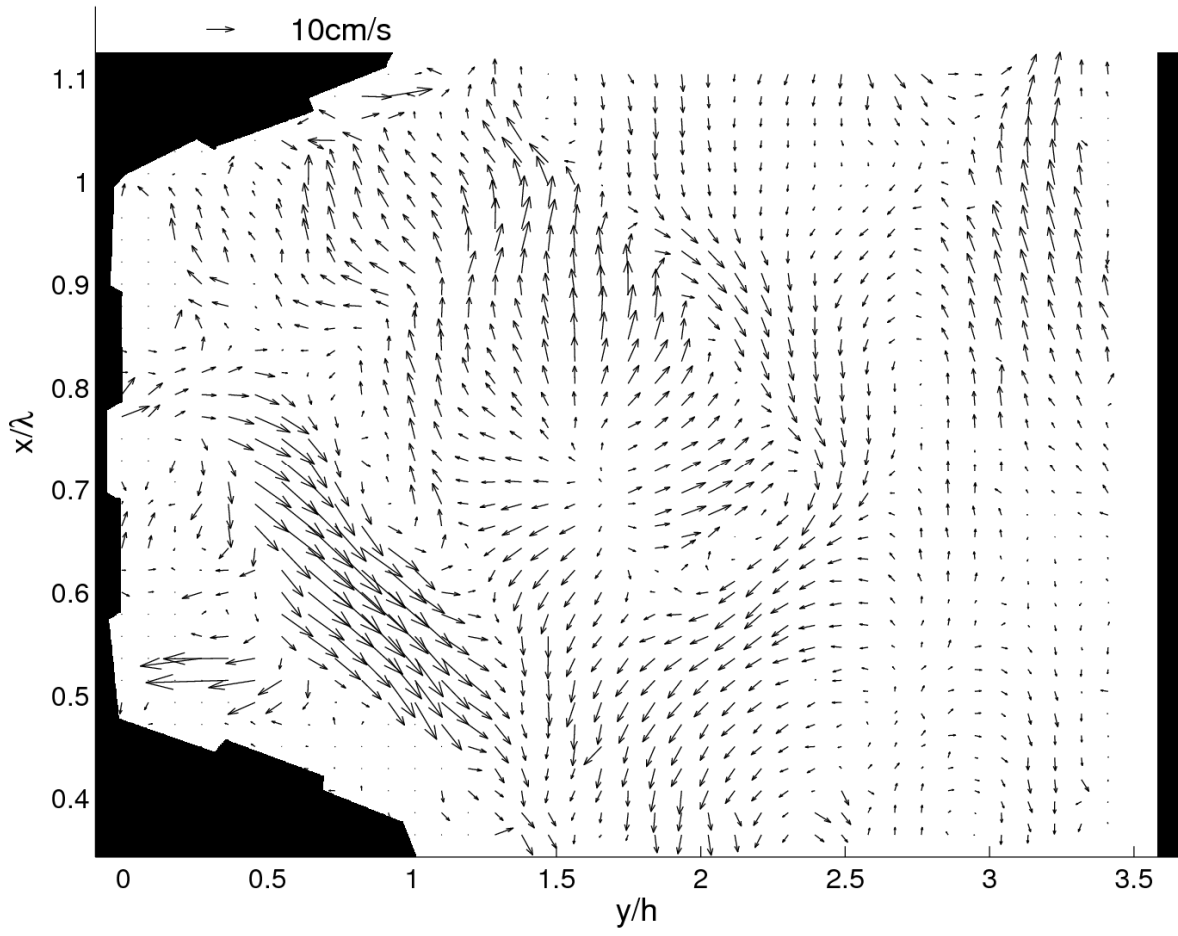
3.10 Figures

Figure 3-1

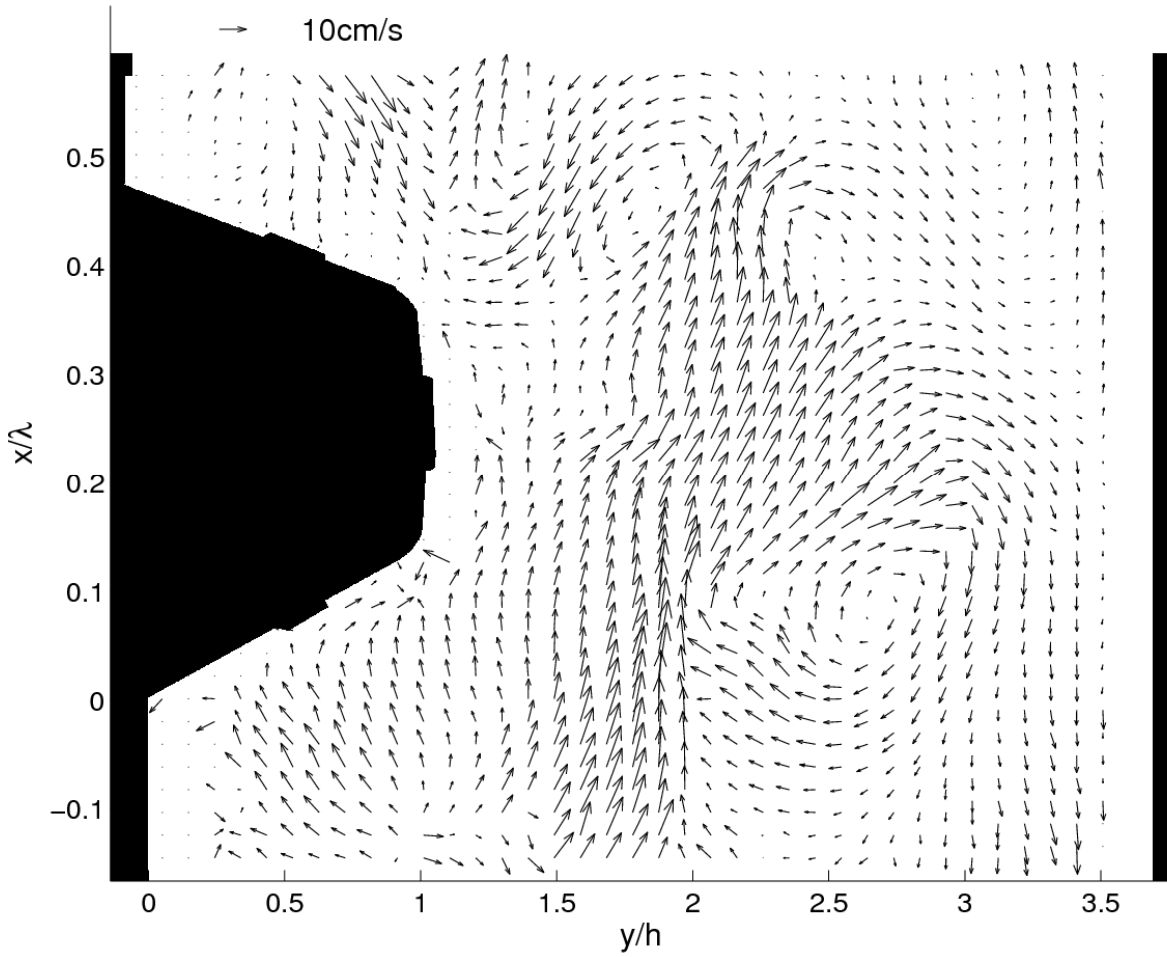


3-1: Schematic of experimental setup.

Figure 3-2



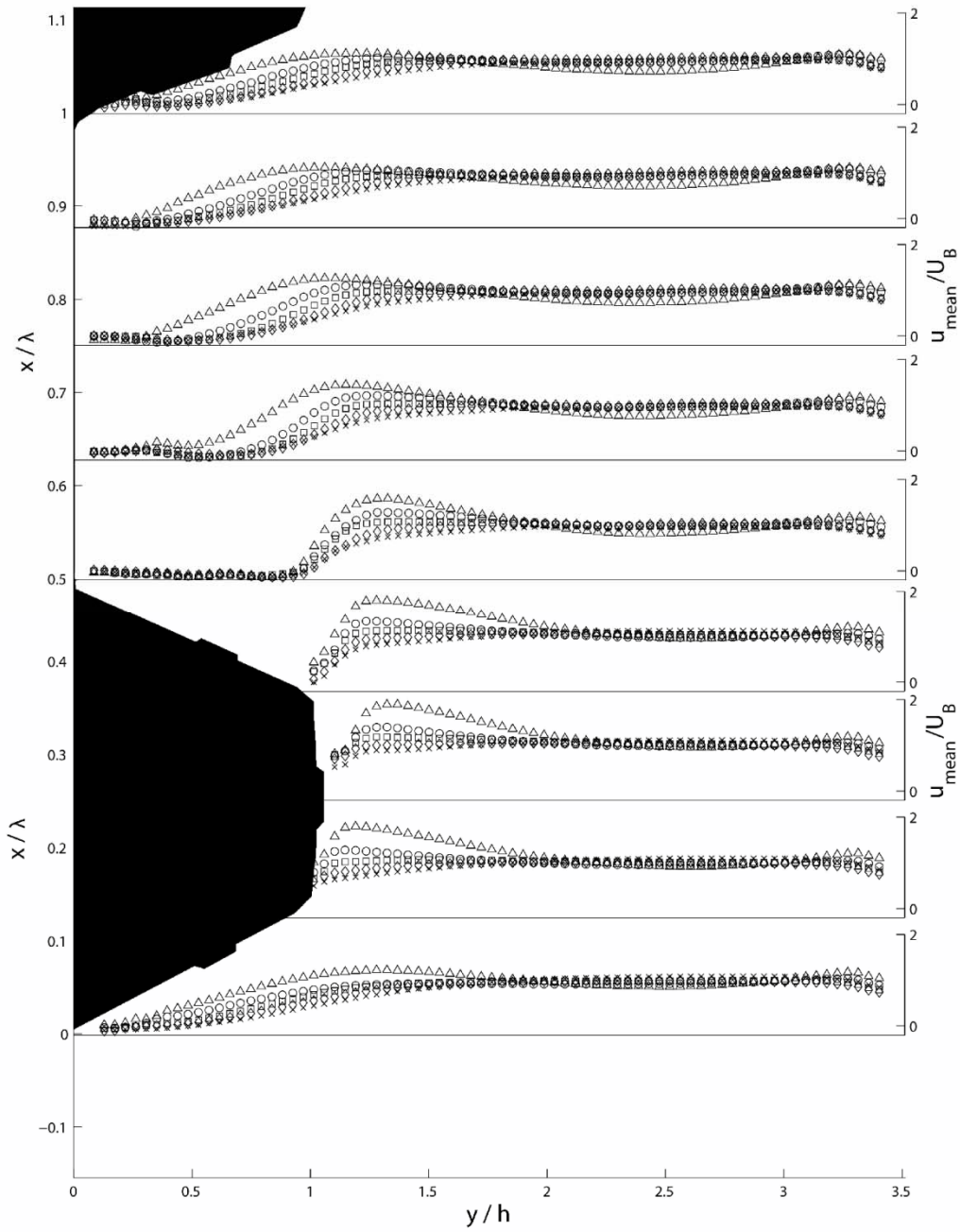
a)



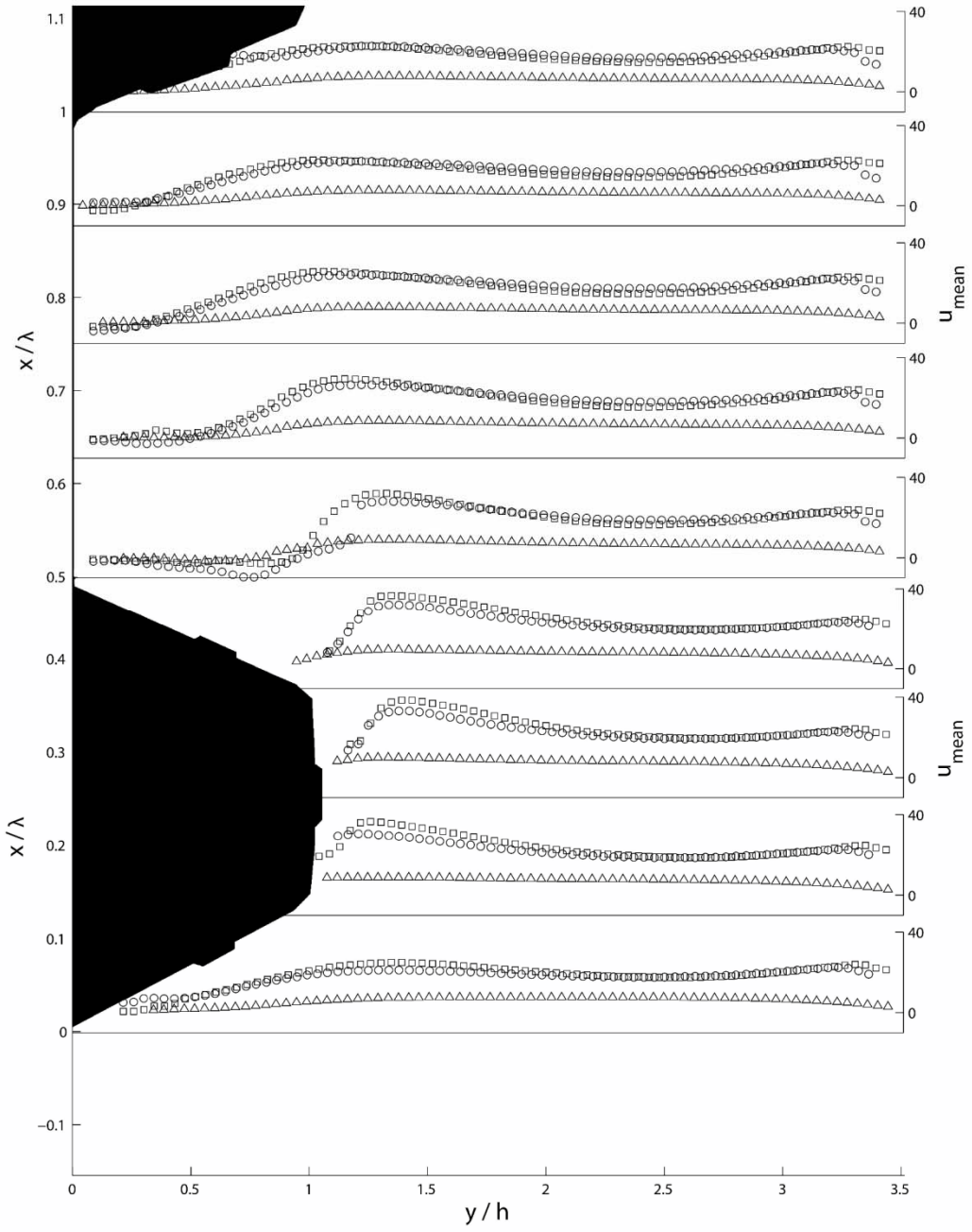
b)

3-2: Turbulent velocity vector fields with reduced resolution at the middle section of the channel ($X/L = 0.57$) at the lowest flow rate (Case I) for the high heating condition (a) over the trough section; (b) over the crest section.

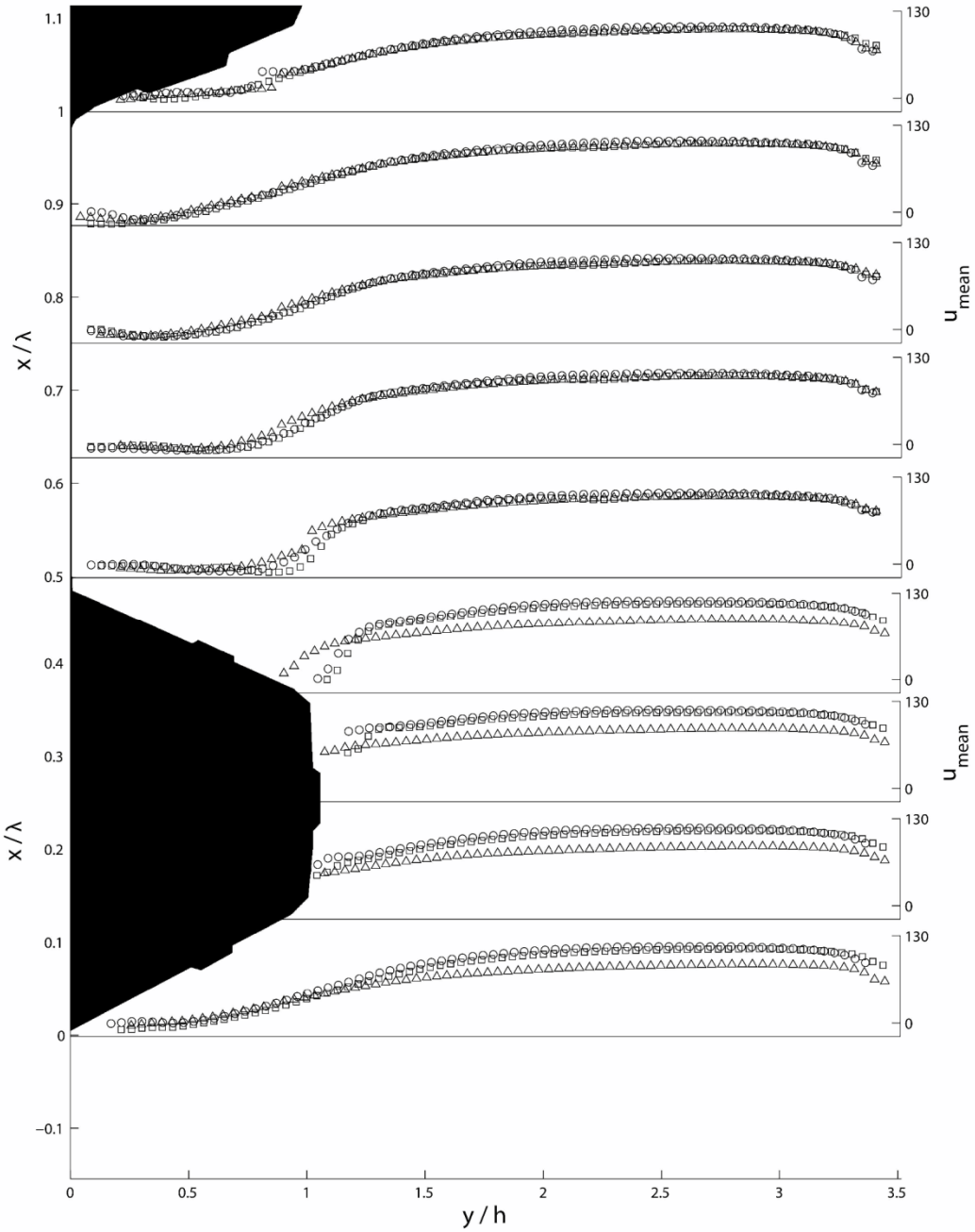
Figure 3-3



a)



b)

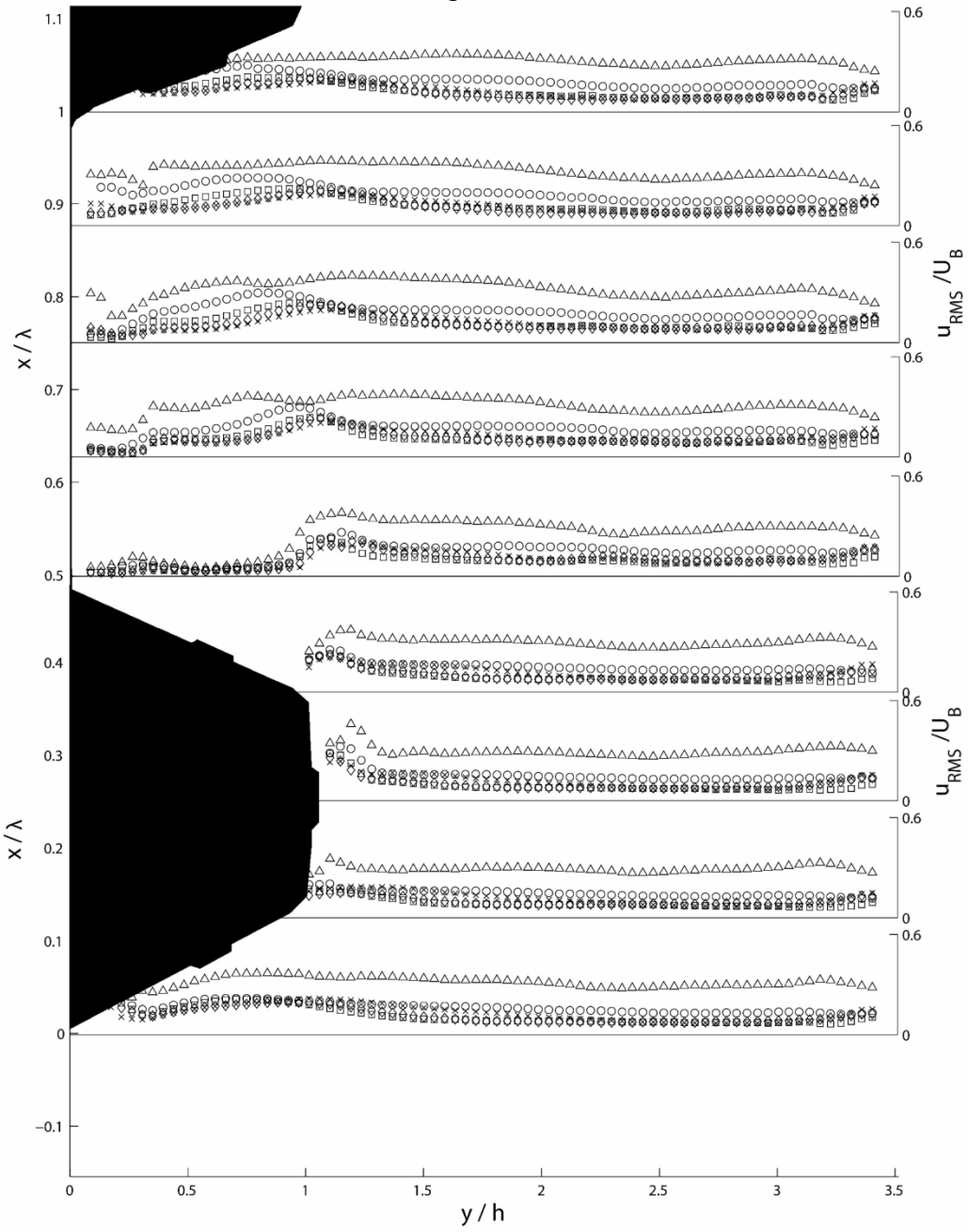


c)

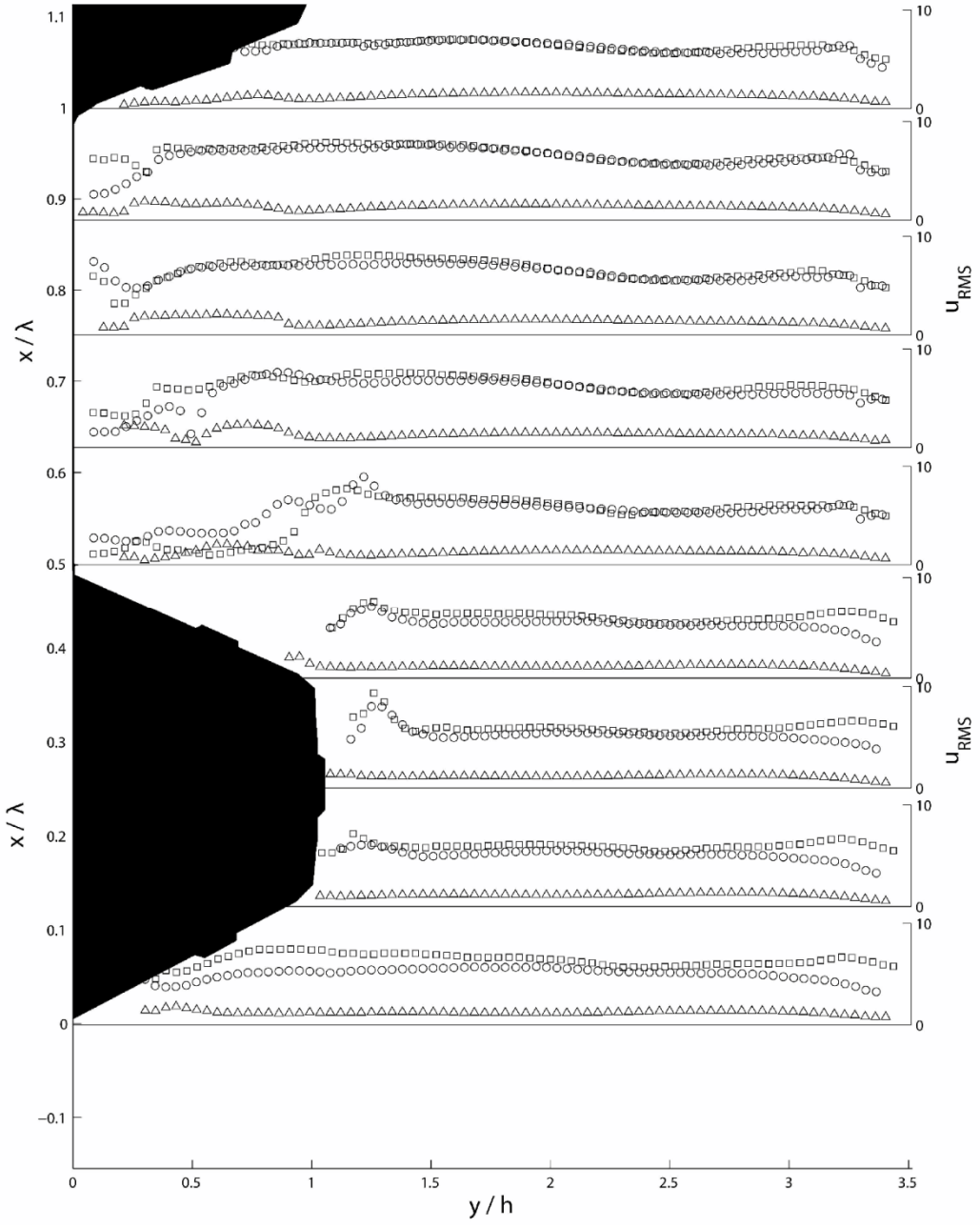
3-3: Mean velocity profiles at over the corrugation waveform at the middle height of the channel ($X/L = 0.57$) (a) at various flow rates normalized by the bulk velocity (U_B) at the high heating condition (Δ), Case I; (\circ), Case II; (\square), Case III; (\diamond) Case IV; (\times), Case V; (b) comparing profiles for different heat conditions at the lowest flow rate (Case I), (Δ), unheated; (\circ), low heating $q_{in} = 530W$; (\square), high heating $q_{in} = 793W$; (c) comparing profiles

for different heat conditions at the highest flow rate (Case V), (Δ), unheated; (\circ), low heating $q_{in} = 530\text{W}$; (\square), high heating $q_{in} = 793\text{W}$.

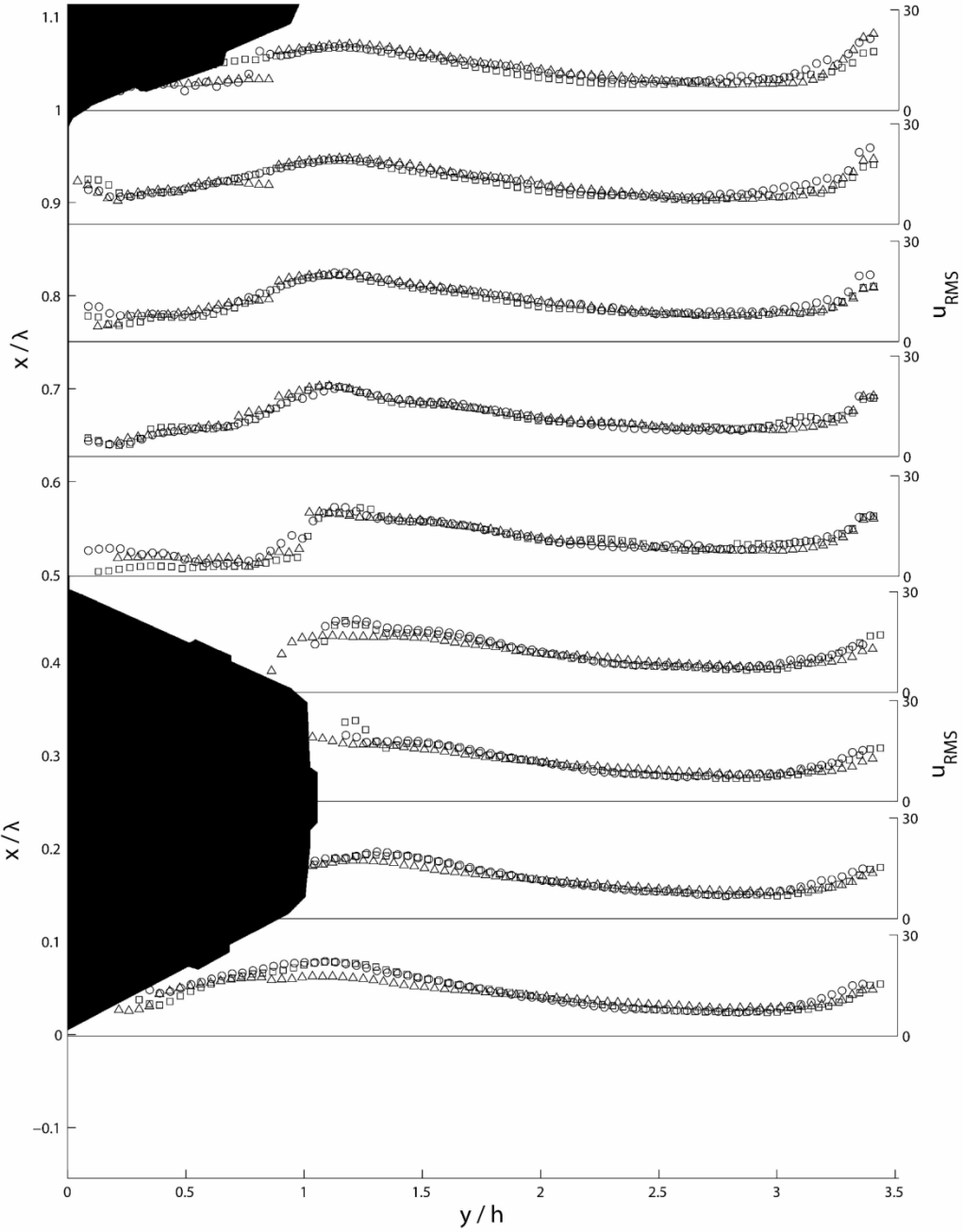
Figure 3-4



a)



b)

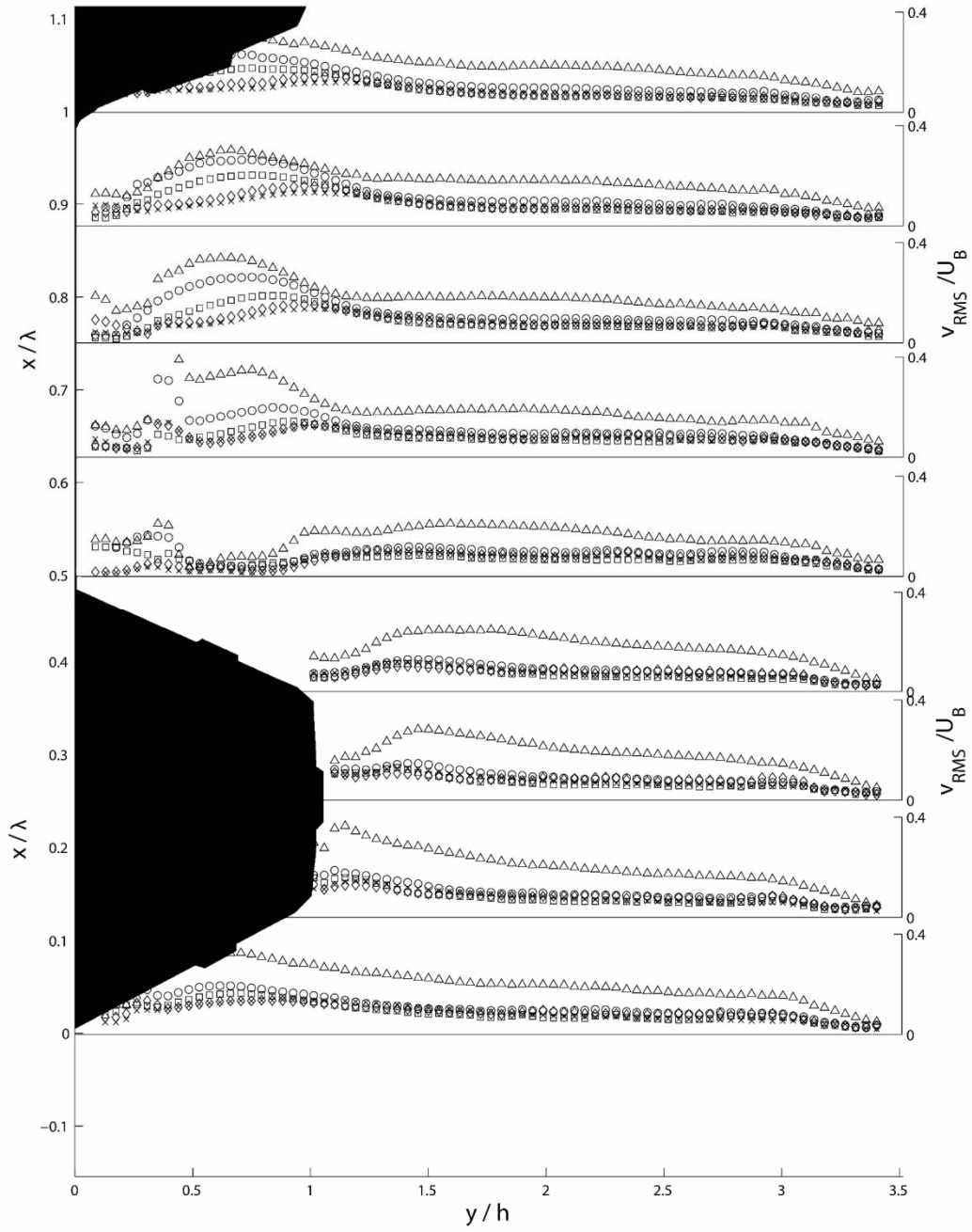


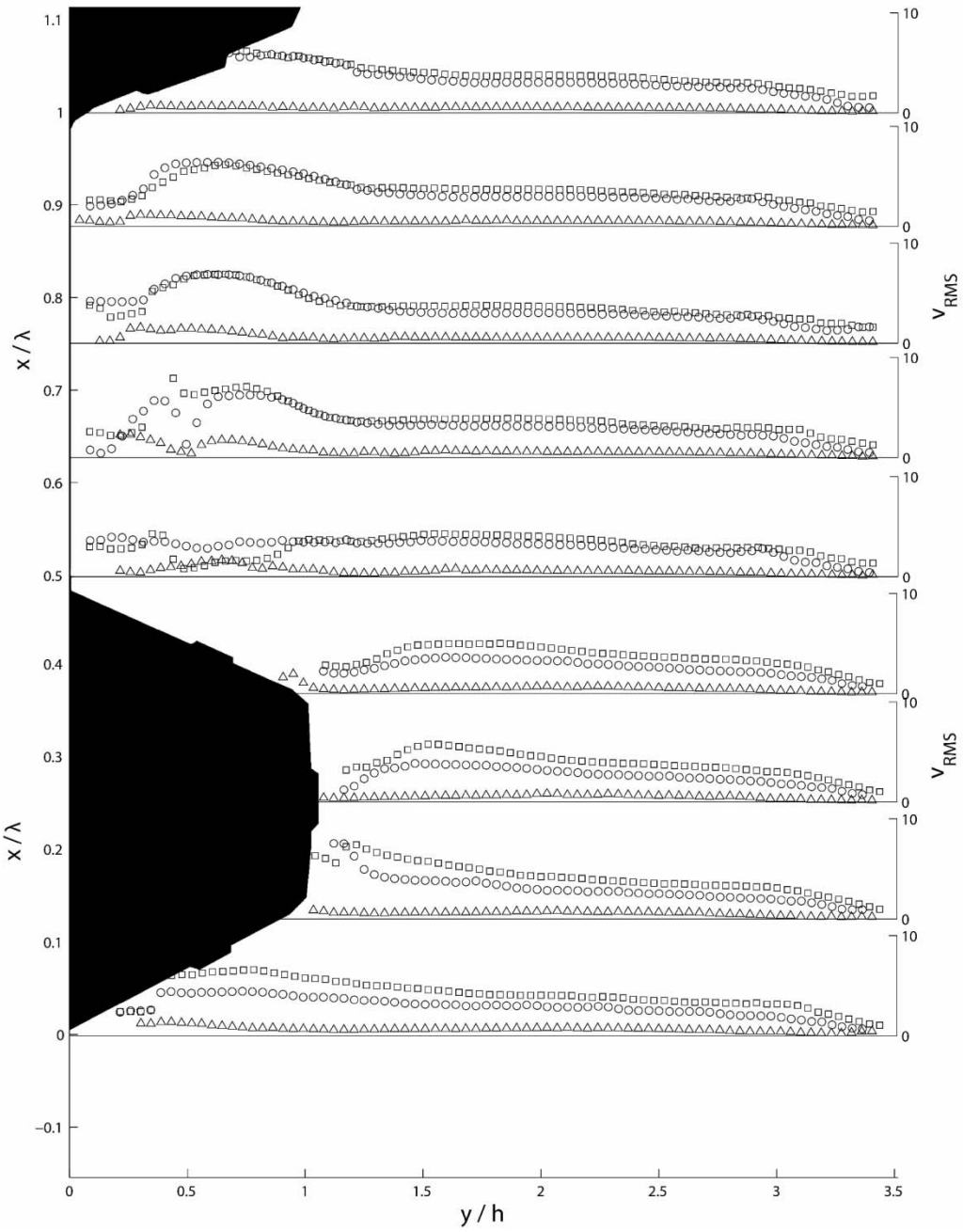
c)

3-4: Profiles of the streamwise (u) RMS turbulent velocity over the corrugation waveform the middle height of the channel ($X/L = 0.57$), (a) at various flow rates normalized by U_B (Δ), Case I; (\circ), Case II; (\square), Case III; (\diamond) Case IV; (\times), Case V; (b) comparing profiles for different heat conditions at the lowest flow rate (Case I), (Δ), unheated; (\circ), low heating q_{in}

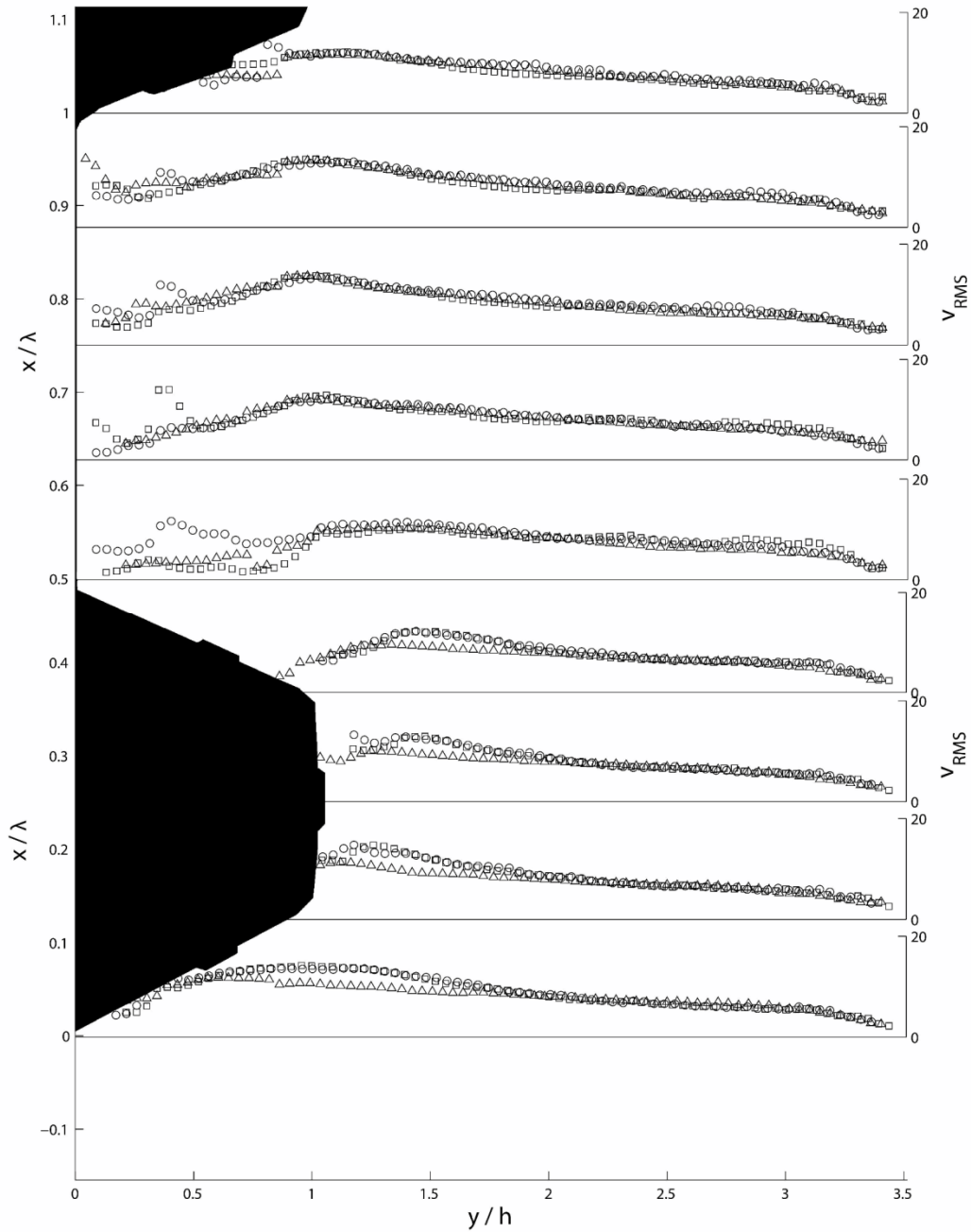
= 530W; (\square), high heating $q_{in} = 793W$; (c) comparing profiles for different heat conditions at the highest flow rate (Case V), (Δ), unheated; (\circ), low heating $q_{in} = 530W$; (\square), high heating $q_{in} = 793W$.

Figure 3-5





b)

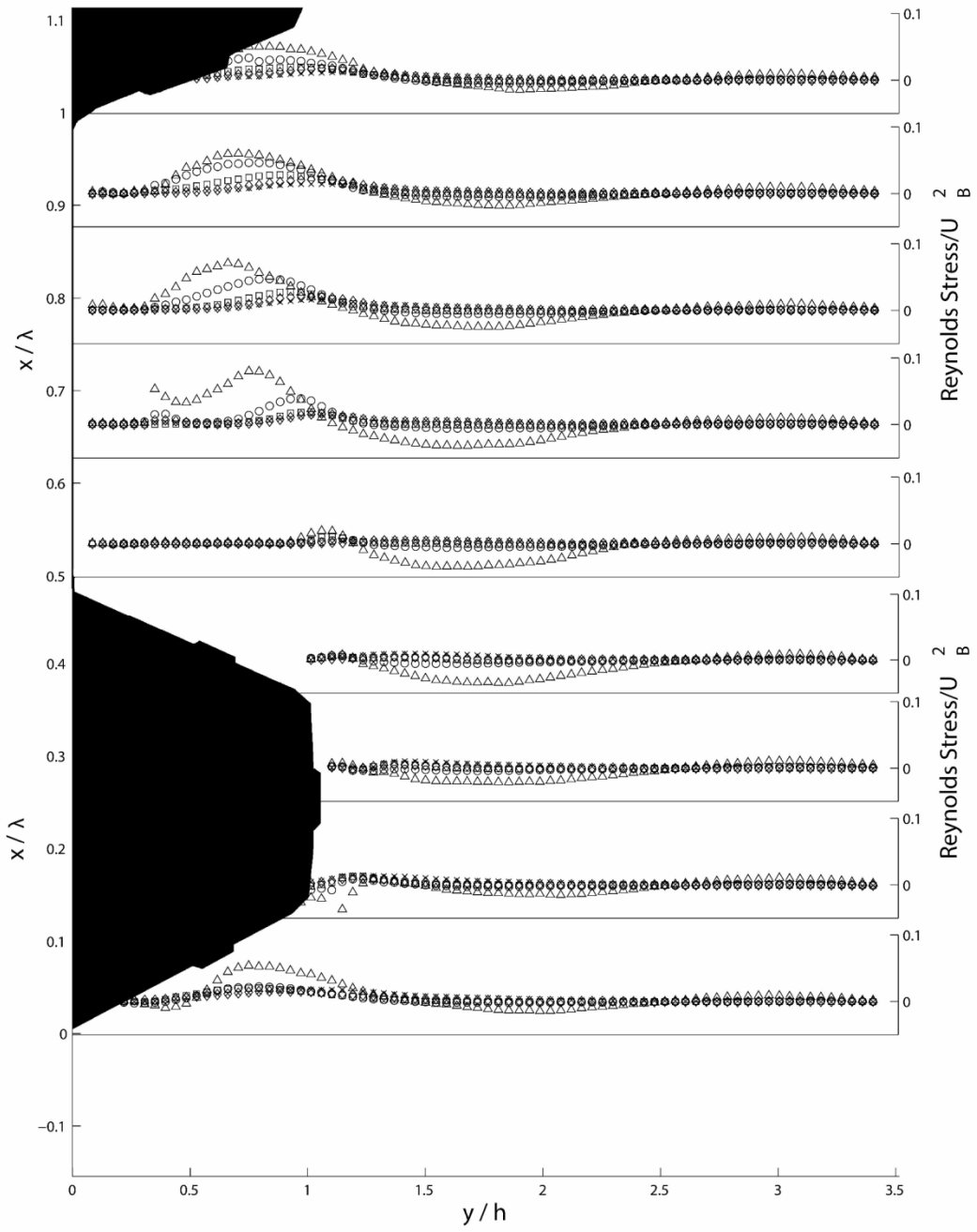


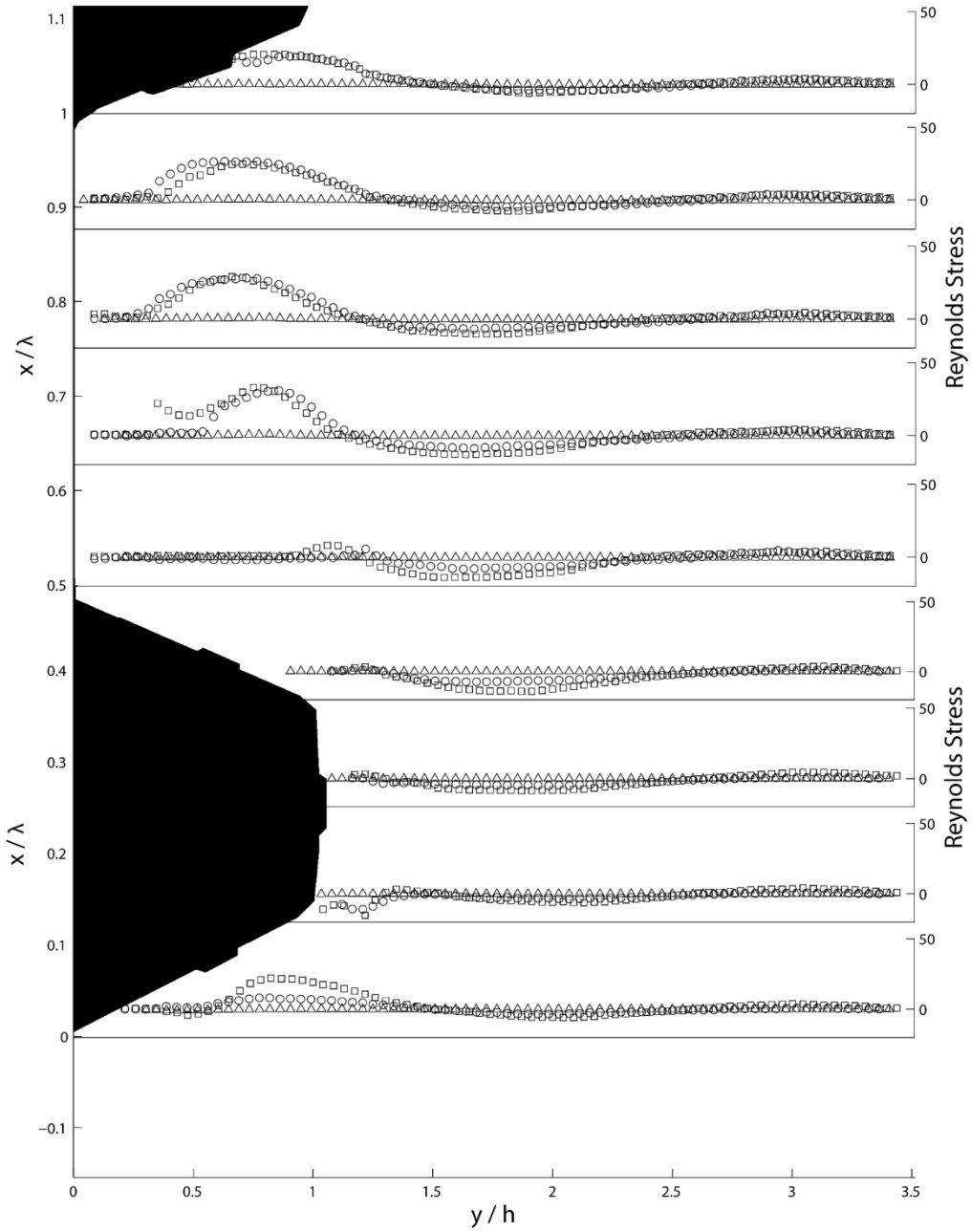
c)

3-5: Profiles of the cross-stream (v) RMS turbulent velocity over the corrugation waveform the middle height of the channel ($X/L = 0.57$), (a) at various flow rates normalized by U_B (Δ), Case I; (\circ), Case II; (\square), Case III; (\diamond) Case IV; (\times), Case V; (b) comparing profiles for different heat conditions at the lowest flow rate (Case I), (Δ), unheated; (\circ), low heating $q_{in} = 530W$; (\square), high heating $q_{in} = 793W$; (c) comparing profiles for different heat conditions at

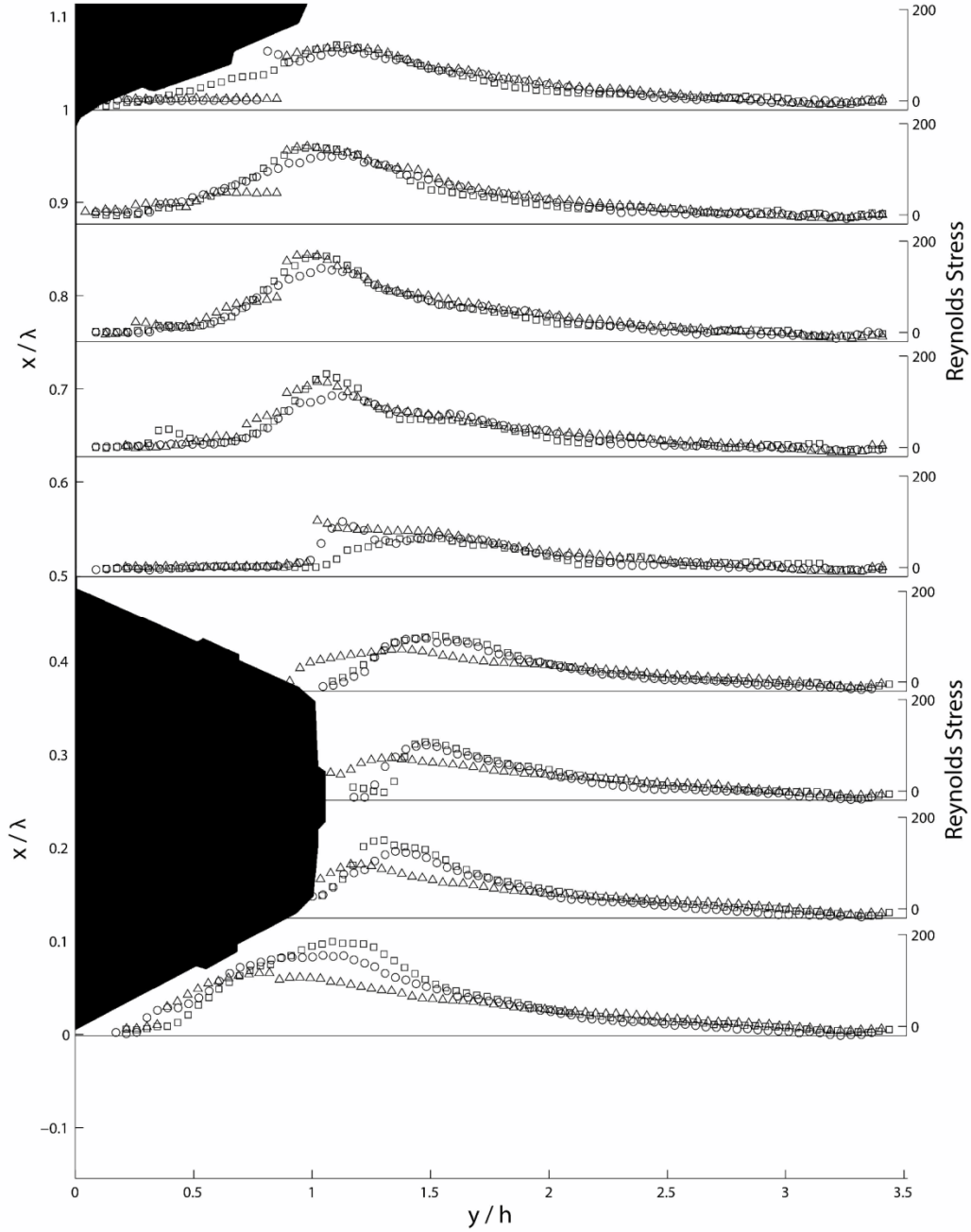
the highest flow rate (Case V), (Δ), unheated; (\circ), low heating $q_{in} = 530\text{W}$; (\square), high heating $q_{in} = 793\text{W}$.

Figure 3-6





b)



c)

3-6: Profiles of the Reynolds stress $(-\overline{u'v'})$ over the corrugation waveform the middle height of the channel ($X/L = 0.57$), (a) at various flow rates normalized by U_B (Δ), Case I; (\circ), Case II; (\square), Case III; (\diamond) Case IV; (\times), Case V; (b) comparing profiles for different heat conditions at the lowest flow rate (Case I), (Δ), unheated; (\circ), low heating $q_{in} = 530W$; (\square), high

heating $q_{in} = 793\text{W}$; (c) comparing profiles for different heat conditions at the highest flow rate (Case V), (Δ), unheated; (\circ), low heating $q_{in} = 530\text{W}$; (\square), high heating $q_{in} = 793\text{W}$.

Chapter 4

Investigation of fundamental flow mechanisms over a corrugated waveform using proper orthogonal decomposition and spectral analyses

4.1 Abstract

This report investigates the interactions between the underlying turbulent structures that together make up the complex flow behaviour observed in corrugated flows. A higher order analysis using proper orthogonal decomposition (POD) and a wave spectrum analysis were conducted on the turbulent velocity vector data on the heated and unheated air flow through a channel with a corrugated waveform. Results showed that turbulent flow energy was produced by the corrugation and transported into bulk flow at both heated and unheated conditions and a given flow rate. At low flow rates, the heated wall increased the total turbulent energy affected the energy distribution across most modes due to buoyancy. Strong energies were seen close to the corrugations, which contributed to sustaining structures at higher modes, while the flow energy was more evenly distributed for the unheated condition. At the highest flow rate, the energy strength and distribution was very similar for low modes and heating effects were most prominent at high modes with higher energies in small-scaled vortices. Overall, the addition of heat influenced the flow at different modes by generating additional structures, structures of greater strength, or by maintaining structures at higher modes at both low and high flow rates.

4.2 Introduction

Increasing the efficiency of heat exchangers is a desirable goal to reduce the energy consumption. A corrugated surface is a passive method suggested to increase thermal performance in channel flows by increasing turbulence and hence mixing [1]. Turbulence is generated over a wavy surface differently than that over a smooth wall because of the flow separation off the waveform crest and the generation of the shear layer. This turbulence then spreads into the following trough region. A common observation in studies conducted on the flow over a waveform is an asymmetric mean velocity profile, with a peak shifted away from the waveform surface, and an increase in the turbulent velocities, Reynolds stress, and turbulent kinetic energy in the vicinity of one wave height [2-7].

Breuer et al. [2] conducted a numerical and experimental study to characterize the flow behaviour over a series of hills for a range of Reynolds numbers. They observed the flow reattachment position varied non-monotonically with the Reynolds number, which was considered to be due to the recirculation flow on the windward side of each hill.

Kruse et al. [3] studied the turbulent flow over sinusoidal waves of three amplitude-wavelength ratios in a channel using particle image velocimetry (PIV) technique. They found that the surface roughness does not have a significant impact on Reynolds stress and energy production approximately one wavelength away from the wall. They also conducted a proper orthogonal decomposition (POD) analysis and observed that the normalized streamwise scales of structures were independent of the waveform amplitude and wavelength at low modes. They also suggested the possibility that at higher modes the streamwise size of structures may be related to the wall curvature.

There are very few studies that examined the relationship between the flow structure and the heat transfer over the waveform. Eiamsa-ard and Promvonge [4] studied the effectiveness of heat transfer over a square waveform with variable spacing. Their results indicate that at sufficiently high Reynolds numbers, the Nusselt number become almost independent of the spacing to wave height ratio. Additionally, at a given Reynolds number, as the spacing between crests increases, the turbulent kinetic energy becomes stronger and spreads wider. Yang and Chen [9] conducted a numerical analysis on the heat transfer effectiveness in a channel flow between two sawtooth corrugated surfaces. By varying the sawtooth angle, they observed that an increase in the corrugation angle increased flow recirculation in the corrugation troughs which resulted in an increased Nusselt number.

The mean velocities and turbulent properties of the flow within a corrugated transpired air collector channel for both a heated and unheated collector have been examined by Greig et al. [7]. For the unheated flow the maximum mean velocity was shifted towards the plane construction wall and peaks of turbulent properties for an unheated flow were located at a channel height of one corrugation waveform. The turbulence produced by the waveform was found to advect and dominate the whole channel, especially at high flow rates. There were instabilities at the lowest low flow rate within the trough sections that produced significantly larger turbulent velocities. This was argued to be the factor that caused the low flows to become turbulent [7]. Greig et al. [8] investigated the influence of heat transfer from the corrugation wall on the mean and turbulent flow structure. It was found that the mean velocity and turbulent property magnitudes were largely enhanced at the low flow rates compared to an unheated flow. At the lowest flow rate, the flow over the heated corrugated wall was primarily buoyancy driven and turbulent instabilities in the trough section were large. As the flow rate was increased, the mean velocity

and turbulent property structures and magnitudes became very comparable to those observed for the unheated flow as forced convection became the dominant flow mode.

The results reported by Greig et al. [7,8] suggest there are mechanisms involved at different scales within the corrugated channel flow that are not fully understood, especially at the highest and lowest flow rates. This report investigates the interactions between the underlying turbulent structures that together make up the complex flow behaviour observed by Greig et al. [7,8]. No reports have been found on the underlying physics of the turbulent structures inside a solar air collector. This investigation specifically looks at the scales of turbulent structures and the energy transfer between these scales comparing the influence of heating and flow rate. It is important to characterize these interactions to utilize results to not only improve the efficiency of the heat transfer in the transpired air collector but results can also be applied to contribute to the understanding of the different layers that comprise the turbulent corrugated flow.

4.3 Experimental Setup

Experiments were conducted to measure the air flow in a two-dimensional channel bounded between a rough corrugation waveform and a plane wall. The channel was 1.83 m long (L), 1.22 m wide and the height of the channel based on the mean corrugation height (H) was 10.95cm. The corrugation amplitude (h) and wavelength (l) are 3.5 cm and 15 cm, respectively. Radiation heat was supplied to the exterior of the corrugation wall by an array of 6×6 60W Sylvania halogen light bulbs spaced evenly 20 cm apart. The experiments were conducted for two heating cases and a non-heating case at five flow rates. Two dimensional instantaneous velocity fields over a complete waveform were obtained at three locations along the channel length, $X/L = 0.41, 0.57, 0.80$, where X was measured from the inlet of the channel (see Fig 4-1). However, the

results presented in this paper are for non-heating and high heating (793 W) cases and at the middle channel location ($X/L = 0.57$). The field of view of the camera was about $15.3 \text{ cm} \times 11.5 \text{ cm}$. For each measurement, 3000 eight bit images were acquired, using an image acquisition system (CoreView, IO Industries), to obtain 1500 velocity fields. Images were captured for the crest and trough regions separately to maintain high resolution, consequently there was about a 20% overlap of these measurement domains. For each position, measurements were taken in the mid cross plane where the flow was two-dimensional. Since the air density and viscosity varies with temperature, the Reynolds number for each flow rate could not be used as the reference parameter when comparing cases. The five flow rates will be referred to as Cases, I, II, III, IV and V; where Case I represents the lowest flow rate while Case V represents the highest flow rate.

The uncertainty in the PIV velocity measurements was computed at the highest flow rate and the high heat case, which has the largest velocity gradients of all cases. Example error calculations are given in Appendix 1. It was estimated based on the criteria and data presented in Cowen and Monismith [10] and Prasad et al. [11] which was produced an error of $\pm 0.29 \text{ cm/s}$ which was less than 1% of the bulk flow velocity.

In the present study high order analyses were utilized to conduct an in-depth investigation of the underlying physical mechanisms associated with the dynamical flow structures and their interactions. These include spectral analysis in the wavenumber domain and proper orthogonal decomposition (POD) analysis. The turbulent velocity data from Greig et al. [7,8] were used for these analyses.

4.3.1 Proper Orthogonal Decomposition Scheme:

A POD analysis in fluid dynamics represents the distribution of flow energy content at different orthogonal modes, thus one is able to determine the locations and energy associated with different turbulent structures. The first mode contains the largest mode energy and the most dominant and energetic structures within the flow. As the mode increases the total mode energy decreases and the size and energy of structures in general, tend to decrease. The primary mode is first determined as the component with the largest variance, and each subsequent mode is determined based on the eigenvectors of the turbulent velocities [12]. POD decomposes a turbulent flow from a data set to derive the orthogonal modes or basis functions, $\phi(\bar{x})$. These modes can be combined to describe different turbulent coherent structures as they are highly correlated with the turbulent flow field. For the present study, the snapshot method was used with planar PIV turbulent velocity data using the algorithm developed by Doddipatla [13]. In this algorithm, the velocity is first expanded into a sum of spatial and temporal components [14]:

$$\bar{u}(\bar{x}, t) = \sum_{n=1}^N a^n(t) \phi^n(\bar{x}) \quad (\text{Eq. 4.1})$$

where $\phi^n(\bar{x})$ is the spatial component known as the basis function and $a^n(t)$ is the temporal coefficient. The eigenvalues can then be obtained from [14]:

$$\int \langle \bar{u}(\bar{x}, t) \bar{u}^*(\bar{x}', t) \rangle \cdot \phi^n(\bar{x}') d\bar{x}' = \lambda^n \phi(\bar{x}) \quad (\text{Eq. 4.2})$$

The eigenvalue λ^n represents the energy of the velocity associated with mode n . Since the POD modes are orthogonal [14-17]:

$$\int \phi^n(\bar{x}) \phi^m(\bar{x}) d\bar{x} = \delta_{mn} \quad (\text{Eq. 4.3})$$

Using the POD modes, temporal coefficients, $a^n(t)$, are obtained by projecting the velocity field onto the POD modes [14-17]:

$$a^n(t) = \int \bar{u}(\bar{x}, t) \cdot \phi^n(\bar{x}) d\bar{x} \quad (\text{Eq. 4.4})$$

Note that the temporal coefficients have a mean of zero.

The algorithm to conduct POD analysis can be validated by comparing the original turbulent velocity fields obtained from the PIV data against the turbulent velocity fields reconstructed by combining all POD modes with their temporal coefficients (Eq. 4.1). Figure 4-2 shows the comparison of an original turbulent velocity with the one reconstructed from the POD modes. The comparison shows that both the structure and magnitudes of the turbulent velocities are almost identical, which validated the POD scheme used in the present study.

4.4 Results and Discussion

Results are presented and discussed based on the turbulent flow data of the unheated and high heating condition at the lowest and highest flow rates presented by Greig et al. [7,8].

4.4.1 Proper Orthogonal Decomposition (POD) Analysis:

The fractional energy distribution averaged over a complete waveform at all POD modes is presented in figure 4-3 for the heated and unheated conditions at the lowest and highest flow rates. In general, the energy decreased with an increase in the POD mode for all cases, as expected. It was observed that at the highest flow rate, the energy magnitude was almost the same at lower modes (up to mode 20) for both heated and unheated cases; however, the energies for the heated flows became larger at higher modes. At the lowest flow rate, almost all modes have higher energy levels for the heated case compared to the unheated case excluding the first

mode. Furthermore at the lowest flow rate, the energy decay was greater between mid and high modes in the presence of heating. These results indicated that the wall heating influenced both the total energy content and its distribution across POD modes. This effect was more dominant at the lowest flow rate and diminishes as the flow rate increases. Greig et al. [7,8] showed at the lowest flow rate, the buoyancy effects dominated the flow in the channel and with as the flow rate was increased, the buoyancy contribution diminished and the flow became primarily inertia driven. Thus the higher energy at the lowest flow rate is due to the presence of strong buoyancy-induced flow.

Comparing the heated and unheated flows at the highest flow rate, the almost identical energy distribution in the lower modes indicates that inertial effects dominate the lower modes up to mode 20. The energy contribution from the buoyancy-induced flow was mainly restricted to the higher modes with low relative energy differences. An interesting observation was that at the first POD mode, the energy of structures was higher for the unheated cases compared to the heated case. Consequently, the first 20 modes for the unheated case constitute about 63% of the total energy, while the first 20 modes in the heated flow account for 45% of the turbulent flow energy. The first mode typically represents the bulk flow structure with the highest energy, representing the overall flow dynamics. This implies that when heat is added from a wall, buoyancy influences the flow and contributes to the growth of instabilities at higher modes.

The turbulent velocity fields provide a general description of the turbulent velocity structure; however, they do not offer insight into the underlying flow features and instabilities that comprise the turbulent velocity fields. The POD analysis decomposes the turbulent velocity field into different modes to obtain an understanding of the structure and dynamics of these underlying interactions. The flow structures at different POD modes are presented in figure 4-4

at the highest flow rate without heating. These POD modes presented were plotted with both the streamwise and cross-stream turbulent velocity energies. All presented POD vector plots use the same scale. POD vector plots at low modes were plotted at half the vector resolution to provide a high quality and clear representation of the energies. POD vector plots at high modes that contain structures of smaller scales were plotted using the full vector resolution in order to depict their interactions.

Figure 4-4a shows the first mode, which contains a very large structure larger than the image frame, with strong streamwise and cross-stream energies closer to the corrugated surface. These energies gradually decrease towards the plane wall. Similar features were observed at the first mode for all cases. This indicates that most of the turbulent flow energy resides near the corrugation wall. As the first mode represents the bulk effects with the largest energy content, it can be argued that the corrugation waveform is the primary source of turbulent flow energy for both a heated and unheated flow, and is then transferred towards the channel core and the plane wall.

Figure 4-4b shows the flow structure at mode 5 and it indicates that the bulk structure observed at mode 1 divided into two distinct structures in the close vicinity of the waveform and the rest of the channel. A large vortex encompassing the channel core is present while the corrugation waveform shows two different features: a vortex on the leeward side of the crest and strong energy burst on the windward side. The structures in the waveform were seen to feed-in to the main vortex in the channel core. The plot also shows that the windward side of the waveform is the dominant source of turbulent flow energy. The flow structure in mode 10 (figure 4-4c) showed further bifurcation, with an overall similar behaviour as seen in mode 5 where the vortices in the channel core have energy supplied to them by structures near the corrugation.

The single vortex seen at mode 5 was split into smaller vortices with the same cross-stream scale. Figure 4-4c also shows a line-source pattern near the windward face of the waveform. This pattern indicates the energy transfer from the out of plane turbulent velocity component. Greig et al. [7,8] have shown that the turbulent velocity field in this channel has three-dimensional effects. This implies that although the channel is primarily two-dimensional, the corrugation waveform induces three-dimensional effects that contribute to the overall turbulent flow energy in the channel.

Mode 20 (figure 4-4d) showed the further structure bifurcation in the channel core as well as in the corrugation waveform, and vortices near the plane wall began to emerge. The windward side of the crest still had the strongest turbulent flow energy and the vortices in the channel core maintained their larger scales compared to those near the waveform. All vortices are further divided into smaller scales with an increase in the mode as depicted in figure 4-4e at mode 50. As seen in the figure, scales of vortices in the channel core and the corrugation wall are almost equal and uniformly distributed throughout the channel. Additionally, the turbulent flow energy appears to be more uniform across the channel, although some regions of strong energy are still observed near the corrugation crest.

Figure 4-4f shows the flow structure at mode 80. The vortices at this mode were primarily located in the vicinity of the corrugation waveform and the strongest among these vortices were the ones that occur within the flow separation zone. It was also observed that the series of vortices along the waveform were comprised of pairs of counter-rotating vortices. The plot also shows the advection of vortices towards the channel core, but they appear to decay as they propagate. The flow structure at mode 150 is depicted in figure 4-4g. Although there are more flow structures, they appear to be smaller and weaker. Similar to mode 80, most of the vortices

are present near the corrugation wall. As the modes increased, the flow became less organized and it was difficult to discern any coherent flow structure.

The plots in figure 4-4 provide a clear depiction of the underlying flow mechanisms that contributed to the turbulent velocity field. The results show that strong vortices are produced along the corrugation waveform particularly in the flow separation zone (figure 4-4f). These vortices serve as the source of turbulence. The vortices advect into the channel core and thereby transport the turbulent flow energy (figure 4-4e). The strong flow energy generated near the corrugation waveform at low modes supplies energy to sustain primary vortices in the channel core (figures 4-4 b-d). These observations are consistent with the profiles of turbulent properties reported in Greig et al. [7]. They observed strongest turbulent velocities and Reynolds stresses within one wave height from the corrugation wall, which was due to the strongest turbulent flow energy and vortices in the vicinity of the waveform as observed in figure 4-4. Furthermore, they also observed a relatively uniform distribution of turbulent intensities in the channel core. This was due to the transport of the turbulent flow energy and its uniform distribution into the channel core by the vortices as observed in figure 4-4.

The results in figure 4-4 provide a general overview of the underlying flow mechanisms associated with the turbulent flow in the given domain. The following will discuss the influence of heating and flow rate on these processes.

Figure 4-5 compares the flow structure in the crest and trough regions since the geometry of the wall is different in both cases. The plots show that the turbulent flow energy along the trough boundary varies significantly. The flow energy adjacent to the leeward side and the trough base is very small, which increases considerably along the windward side. The low energy in this

region could be due to the flow becoming almost stagnant after the flow separation. The strong energy on the windward side could be due to the flow reattachment; this interaction could induce strong instabilities and velocity gradients, resulting in high turbulence. The core of the trough region shows strong vortices that transport energy to the channel core. Comparison of the flow structure above the crest and trough shows that the overall flow structure is quite similar and the vortices have similar strengths and scales. Similar trends were observed at different modes for all cases.

Figure 4-3 shows that at high flow rate, the energy distribution at lower modes is almost identical in the presence and absence of heating while the higher modes have larger energy magnitude in the presence of heating. Figure 4-3 only provides information about the overall mode energy. To understand the influence of wall heating on the flow mechanisms, the flow structures at different modes are compared in the presence and absence of heating. Figure 4-6 shows these structures at low and high modes at the highest flow rate at both heated and unheated conditions. The comparison of POD mode 12 at both conditions (figures 4-6 a & b) show that although the overall energy fraction at both conditions is similar, the structure and distribution of turbulent flow energy within the mode is different in the presence and absence of heating. Most of the flow energy was concentrated near the corrugation wall and the flow structure comprised of larger scale for the heated flow. Conversely, the flow structures had relatively smaller scales under no heat influence and the energy was more uniformly distributed across the channel. For mode 70 (figures 4-6 c & d), although both conditions show a focus of vortices near the corrugation, the energy of the structures near the corrugation was approximately equal to those in the bulk flow for the unheated condition. The turbulent flow energies with the heated surface produced vortices of greater energy towards the corrugation and weaker vortices in the channel

core. The scales of structures for both the heated and unheated conditions were approximately the same in the bulk flow, as well as close to the waveform. When comparing the turbulent flow energy of the heated and unheated conditions at high flow rates (figure 4-3), it was seen that the relative energy of the heated flow is greater than those in the unheated flow at the same mode. These higher energy levels most likely exist in the vortices near the corrugation wall as described earlier.

At the lowest flow rate, the comparison of the flow structures at the lower mode shows that the scales are comparable at both heated and unheated conditions (figures 4-7 a & b). The turbulent flow energy in the channel core is also comparable at both conditions, however, strong flow energy is observed in the vicinity of the corrugation wall in the presence of heating. The energy distribution profiles in figure 4-3 shows that at the lowest flow rate, the fractional energy is higher in the presence of heating. Based on the inspection of the detailed flow structure, it can be concluded that the higher fraction energy at the heating condition is mainly contributed by the strong energy magnitudes in the vicinity of the corrugation wall. As mentioned earlier, at the lowest flow rate, the buoyancy effects were dominant. Buoyancy induces thermal plumes into the flow. Greig et al. [8] showed that these thermal plumes interact with the mean flow and enhanced the magnitudes of mean and turbulent velocities and the Reynolds stress in the vicinity of the corrugation wall. At higher modes (figures 4-7 c & d), it is still apparent that there are higher turbulent flow energies for the heated condition compared to the unheated, which is consistent with figure 4-3. Unlike the lower modes, the energy for both conditions was more evenly distributed across the channel instead of focusing in the vicinity of the corrugation. The structures were more distinguishable and organized in the heated flow, while the unheated flow had weaker energies producing fewer organized structures. For the unheated flow, the only

source of turbulence was that produced by the waveform, yet the flow was visibly still generally organized. Thus the majority of the energy was in lower modes where the larger structures were more prominent in the flow. However when heating was introduced, the thermal plumes created additional sources of turbulence when interacting with the mean flow; consequently, the turbulent flow energies are higher. These higher energies resulted in stronger energies around the waveform at low modes, and also maintained structures at higher modes in the core of the channel.

4.4.2 Spectral Analysis:

The POD analysis provides a deep insight into the energy and structure of the flow at different modes and gives an understanding of the underlying flow mechanisms. Another analysis that also offers detailed information about different turbulent scales and their energy transfer process is the spectral analysis. In the present study, the spatial spectral analysis is performed to obtain a clear understanding of the fundamental energy transfer processes and their corresponding scales created by the corrugation waveform as well as the wall heating. The one dimensional wavenumber spectra were computed for both streamwise and cross-stream components of turbulent velocity. For each case, the spectrum was computed all streamwise locations along the waveform in the cross-stream direction for each turbulent velocity field and then averaged. The spectra wavenumbers are scaled by the spatial resolution of the frame and energies are normalized based on the bulk flow velocity and average channel height (H).

The POD analysis has shown that the corrugation waveform has an impact on the turbulent flow energy for both flow rates and heating conditions. To investigate the impact of the waveform on the energy content and energy transfer process, the wavenumber spectra of the streamwise

turbulent velocity component are plotted in figure 4-8 at different locations along the waveform at the lowest and highest flow rates for the unheated case. The plot in figure 4-8a shows the shape of the spectra are quite similar at the lowest flow rate, but the spectral energy over top of the crest is lower than those in the upstream and downstream troughs. Similar trends are observed at the highest flow rate (figure 4-8b). A plausible explanation for this trend could be that the spectra in the troughs correspond to the locations where the influence of flow separation is most intense and the POD analysis has shown the presence of strong vortices in those regions. Therefore, the turbulent kinetic energy is expected to be the largest in those regions. This is further confirmed by the turbulent intensity profiles in Greig et al. [7] which show significant enhancement of both streamwise and cross-stream turbulent intensities in the middle of trough as compared to the crest. At the highest flow rate, all spectra exhibit a slope of $-5/3$ which indicates the presence of the inertial subrange. The $-5/3$ slope describes the dissipation of energy due to viscosity as derived by Kolmogorov [21]. At the lowest flow rate for the unheated condition, the spectra exhibit two different slopes: in the low wavenumber range the spectra follow a -3 slope, and in the high wavenumber range, they follow the conventional slope of $-5/3$ [18]. The -3 slope implies a higher rate of energy transfer. In typical turbulent flows, the energy transfer rate in the inertial subrange is constant and equal to the dissipation rate [19]. However, in this study the lowest flow rate corresponds to a Reynolds number of approximately 530, which falls well within the laminar regime for the plane wall geometry. The corrugation geometry and the wall roughness forced an earlier transition to turbulent flow at this flow rate [7]; however, the viscous effects are still relatively significant. A possible reason behind the steeper slope in the low wavenumber range could therefore be that the energy transfer rate was influenced by viscosity and resulted in a faster decay. In the inertial subrange (slope $-5/3$), the energy transfer rate does

not depend on viscosity and is typically located in the mid wave numbers. However, the lowest flow rate exhibited the inertial subrange at higher wavenumbers, which was unusual since the viscous effects were expected to be more significant in this range. As mentioned earlier, at the lowest flow rate, the flow transitions to turbulent flow due to the presence of the corrugation; therefore, a plausible explanation for this spectral trend could be the complex interaction between the viscous and inertial forces during transition. This was consistent with the finding of low uniform turbulent flow energies observed for the same case depicted by figure 4-7c.

To study the impact of wall heating on the spectral energy distribution and the energy transfer, the wavenumber spectra of both streamwise and cross-stream turbulent velocities were plotted at the mid-crest and mid-trough locations at the lowest and highest flow rates for heated and unheated conditions in figure 4-9. A common observation in all spectra was that the spectral energies at the highest flow rate were comparable in general. The low wavenumber range ($k \sim < 40$ rad/m) showed larger energies in the unheated flow while the high wavenumber range ($k > 40$ rad/m) the heated flow energies were generally larger. This indicated that the wall heating primarily strengthened the smaller-scale structures. This trend was consistent with the POD energy distribution plot (figure 4-3) that showed the higher modes contained relatively more energy in the presence of heating. The plots in figure 4-9 also showed that, overall, the spectra follow the slope of $-5/3$ at some range of scales for both the streamwise and cross-stream scales of energies. There were some steeper slopes at higher wavenumbers observed in the trough region. It is observed that in general the trends of streamwise and cross-stream spectra are similar, however, the energy transfer rate to higher wave numbers for streamwise velocity spectra was relatively larger than those in the cross-stream direction.

At the lowest flow rate, the spectra of the heated flow exhibited higher energies at all given wavenumbers compared to the unheated flow. This trend is also consistent with the POD energy distribution in figure 4-3. As previously indicated, the lowest flow rate showed spectra that exhibited the -3 slope in the low wavenumber range while the -5/3 slope at higher wavenumbers. This, again, was probably due to the greater influence of viscous effects at low flow rates that dissipated energy at a greater rate. In the presence of heating, the -3 slopes covered almost all the scales, including the inertial subrange, thus the spectra energy decayed faster. In the presence of buoyancy-induced flow, Turner [20] proposed the existence of a buoyancy-subrange, where turbulence is utilized in working against buoyancy forces resulting in a rapid energy transfer, which is manifested as a steeper slope of about -3 in the spectrum [20]. The results suggest the same trend and buoyancy forces dampen the turbulence for the heated condition at the lowest flow rate.

The plots in figures 4-8 and 4-9 show that in the low wavenumber range ($k < 20$ rad/m), the spectral energy is either constant or decreased indicating that this range is associated with energy containing eddies. This wavenumber range corresponds to the length scales of 30 cm or higher. These scales are quite comparable to the large eddies observed at the lowest POD modes that occupied the entire channel domain and extended over a corrugation wavelength or more (for example figure 4-4b).

Combining the details from the POD and spectra analyses, it was found that heating provides a more significant amount of additional energy at the lowest flow rate, while the energy levels and transfer rates between the unheated and heated conditions were comparable at the highest flow rate. The energies created by heating the corrugated surface are present in the higher modes and smaller scaled structures for higher flow rates (Figures 4-3 and 4-9). At the lowest flow rate,

heating generally increases the turbulent energies at all modes and scales, however the rate of energy transfer to smaller scales is very comparable to the rates observed for the unheated flow (figure 4-9). As previously stated, heating greatly affects the lowest flow rate by producing thermal plumes. These thermal plumes interact with the bulk flow and create more structures concentrated around the corrugation. The structures have higher energies than those in the unheated flow and are able to be sustained to higher modes. The corrugation waveform induces turbulence for Reynolds numbers as the lowest flow rate examined with and without the presence of a heated wall. The structures created by turbulence were large at low modes and originated in the core of the channel, while at higher modes these structures bifurcated and were concentrated in the vicinity of the waveform for both flow rates and heating conditions. This was the primary influence on the high turbulent velocities and Reynolds stresses seen in the same vicinity by Greig et al. [1,2].

4.5 Conclusions

Proper orthogonal decomposition and wave spectra analyses were conducted on the heated and unheated flow of turbulent air over a channel with a corrugated waveform at a low and high flow rate. It was found that turbulent flow energy was generated by the corrugation and that energy was transported into the channel core for both heated and unheated conditions at both flow rates. The energy contribution due to heating was evident in both flow rates, however, at different modes. At the lowest flow rate, the heated wall increased the total turbulent energy and its distribution at all modes (excluding the first) due to the flow being buoyancy dominated. Inertia induced turbulence created by the waveform were dampened by these buoyancy forces resulting in a larger energy transfer rate. The flow energy at the lowest flow rate was more evenly distributed for the unheated condition, while the heated condition produced strong energies close

to the waveform that contributed to sustaining structures at higher modes. At the highest flow rate, the energy strength and distribution was very comparable at low modes and the heating was only evident at high modes with higher energies in smaller scaled vortices. Heating has been found to either produce additional structures, structures of higher strength, or maintain structures within the flow over a corrugated waveform at both low and high flow rates. The results contribute to the explanation of the turbulent velocity and Reynolds stress profile trends within the corrugated channel at high and low flow rates.

4.6 Acknowledgements

The authors would like to acknowledge Natural Sciences and Engineering Research Council of Canada (NSERC), the Canadian Solar Buildings Research Network (SBRN) and the University of Western Ontario for providing the support.

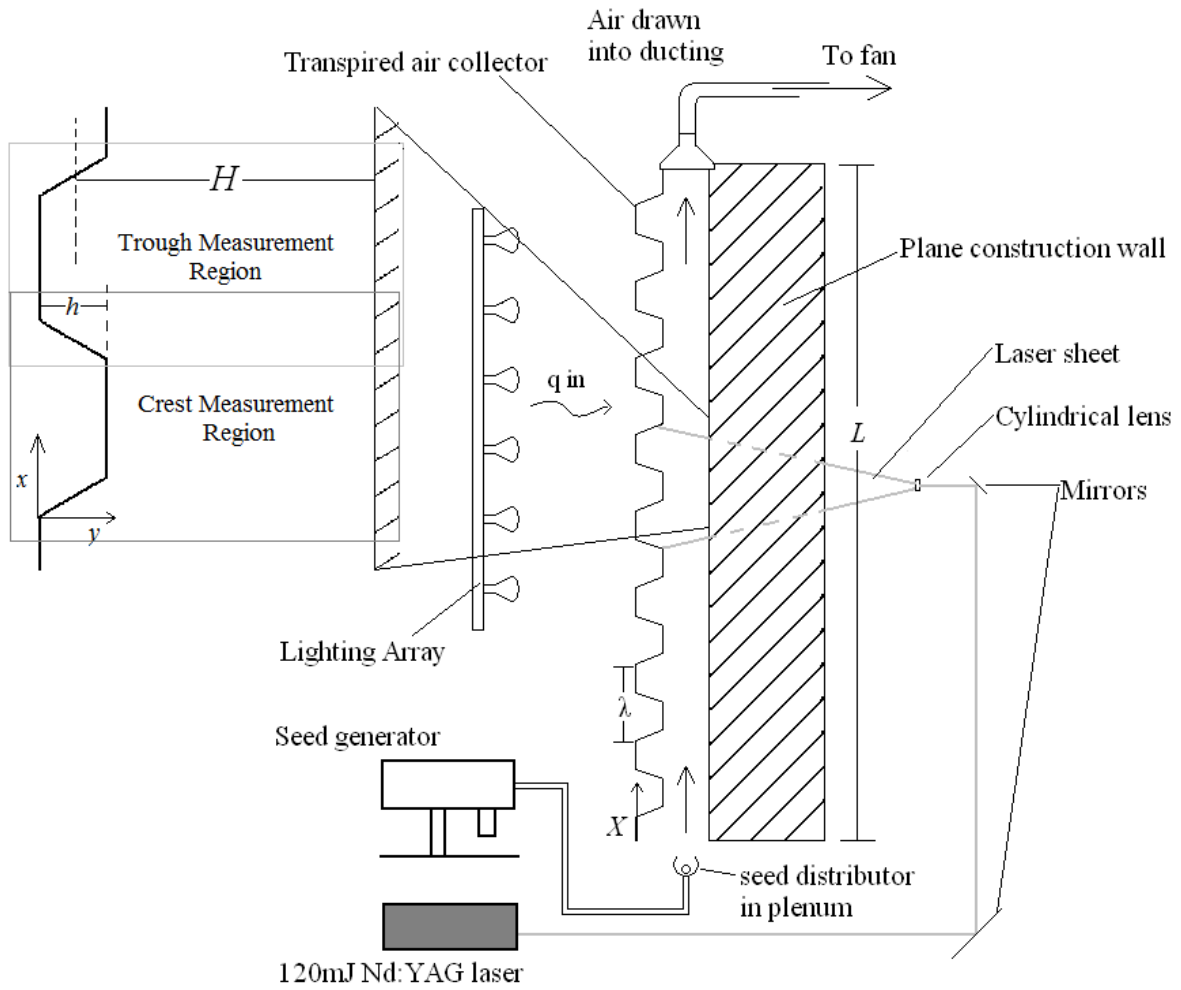
4.7 References

- [1] R. L. Webb, and N. H. Kim, Principles of enhanced heat transfer, London, UK: Taylor & Francis. 2005.
- [2] M. Breuer, N. Peller, Ch. Rapp, and M. Manhart, Flow over periodic hills – Numerical and experimental study in a wide range of Reynolds numbers, *Computers and Fluids* 38, (2009) 433.
- [3] N. Kruse, S. Kuhn, and P. R. V. Rohr, Wavy wall effects on turbulence production and large-scale modes, *J. Turbul.* 7 (31) (2006).
- [4] S. Eiamsa-ard, P. Promvong, Numerical study on heat transfer of turbulent channel flow over periodic grooves, *Int. Comm. in Heat and Mass Transfer* 35 (2008) 844-852.
- [5] J. D. Hudson, L. Dykhno, and T. J. Hanratty, Turbulence production in flow over a wavy wall, *Exp. Fluids* 20 (1996) 257.
- [6] R. J. Calhoun and R. L. Street, Turbulent flow over a wavy surface' Neutral case, *J. Geophys. Res.* 106 (2001) 9277.
- [7] D. Greig, K. Siddiqui, and P. Karava, An experimental investigation of the flow structure over a corrugated waveform in a transpired air collector, *Int. J. Heat and Fluid Flow* (2012a) Unpublished results.

- [8] D. Greig, K. Siddiqui, and P. Karava, The influence of surface heating on the flow dynamics within a transpired air collector, *Int. J. Heat and Mass Transf.* (2012) Unpublished results.
- [9] Y.-T Yang, and P.-J Chen, “Numerical simulation of fluid flow and heat transfer characteristics in channel with V corrugated plates.” *Heat Mass Transf.* **46**, 437 (2010).
- [10] E. A. Cowen, S. G. Monismith, A hybrid digital particle tracking velocimetry technique, *Exp. Fluids* 22 (1997) 199.
- [11] A. K. Prasad, R. J. Adrian, C.C. Landreth, and P. W. Offutt, Effect of resolution on the speed and accuracy of particle image velocimetry interrogation, *Exp. Fluids* 13 (1992) 105.
- [12] J. Kostas, J. Soria, and M.S. Chong. A comparison between snapshot POD analysis of PIV velocity and vorticity data, *Exp. Fluids* 38, (2005) 146.
- [13] L.S. Doddipatla, Wake dynamics and passive flow control of a blunt trailing edge profiled body, PhD Thesis, Department of Civil and Environmental Engineering, University of Western Ontario, 2010.
- [14] P. Holmes, J.L. Lumley, and G. Berkooz, *Turbulence, Coherent Structures, Dynamical System and Symmetry*. Cambridge, 1st ed. (1996).
- [15] P.G. Cizmas, A. Palacios, T.O. Brien, and M. Syamlal, Proper-orthogonal decomposition of spatio-temporal patterns in fluidized beds. *J Chem. Engg. Sci.* 58 (19), (2003), 4417-4427.
- [16] S. Maurel, J. Boree, and J.L. Lumley, Extended Proper Orthogonal Decomposition: Application to Jet/Vortex Interaction. *Flow Turb. Combust.* 67, (2001), 125-136
- [17] T.R. Smith, J. Moehlis, and P. Holmes, P. Low-dimensional modeling of turbulence using the Proper Orthogonal Decomposition: A Tutorial. *Non-linear Dynamics* 41, (2005) 275-307.
- [18] J. O. Hinze, *Turbulence*, McGraw-Hill, New York, 1975.
- [19] S. B. Pope, *Turbulent Flows*, Cambridge University Press, 2000.
- [20] J. S. Turner, *Buoyancy Effects in Fluids* Cambridge University Press, Cambridge, 1973.
- [21] H. Tennekes and J.L. Lumley, *A First Course in Turbulence*, The MIT Press, USA, 1972. pp 262-286.

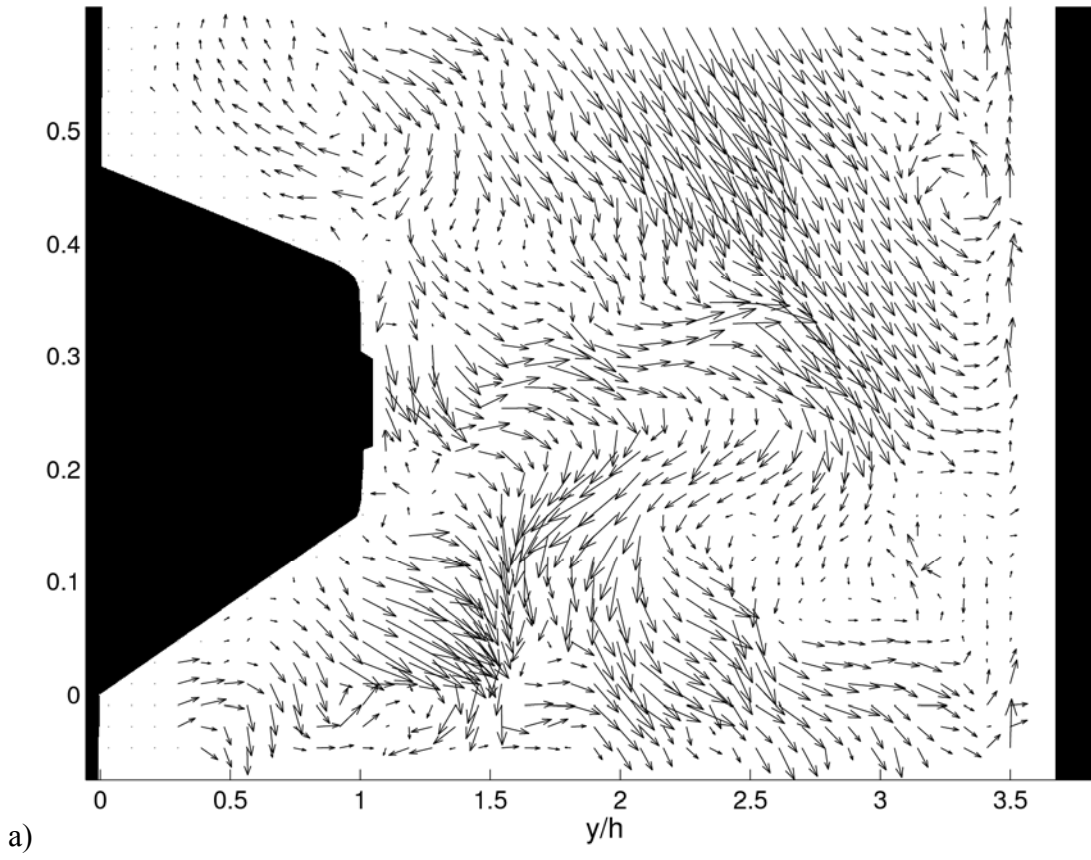
4.8 Figures

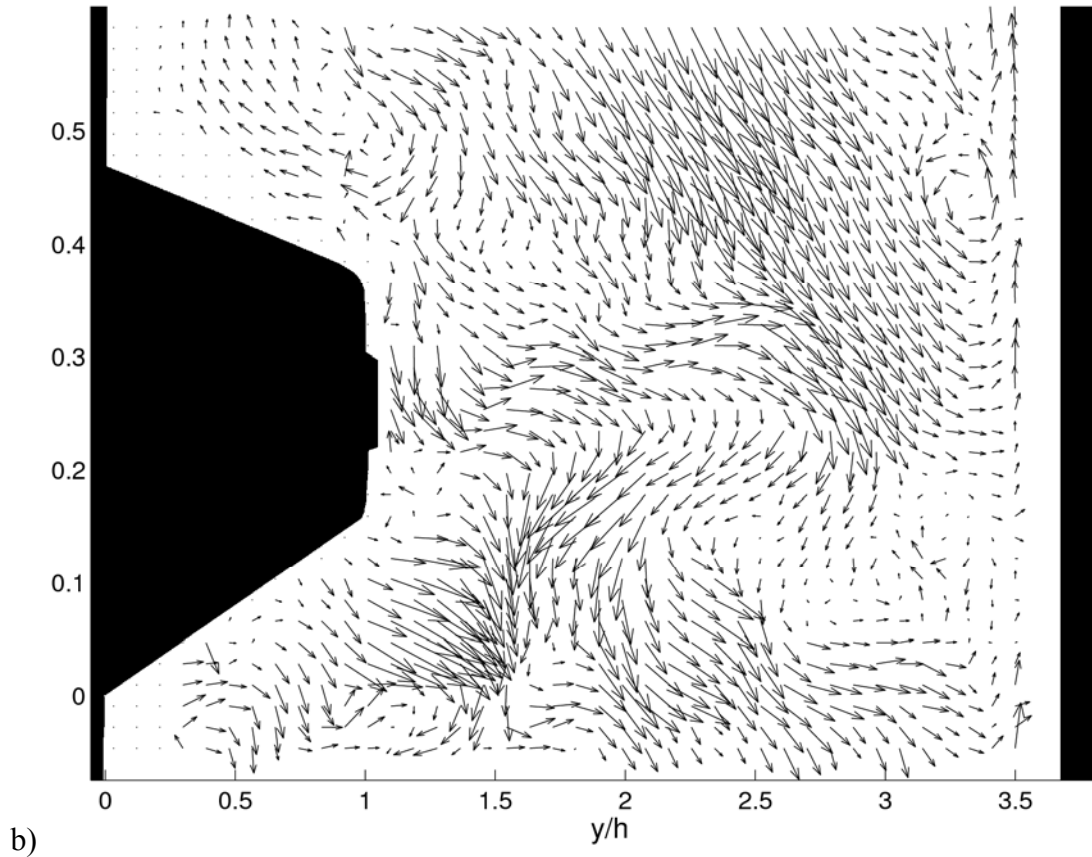
Figure 4-1



4-1 Schematic of setup.

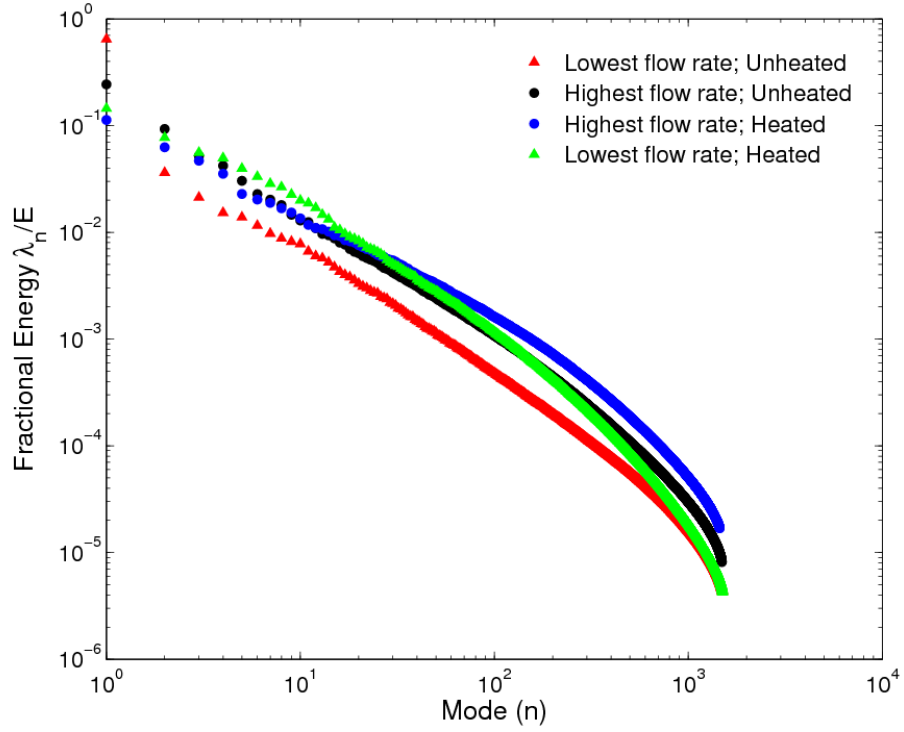
Figure 4-2





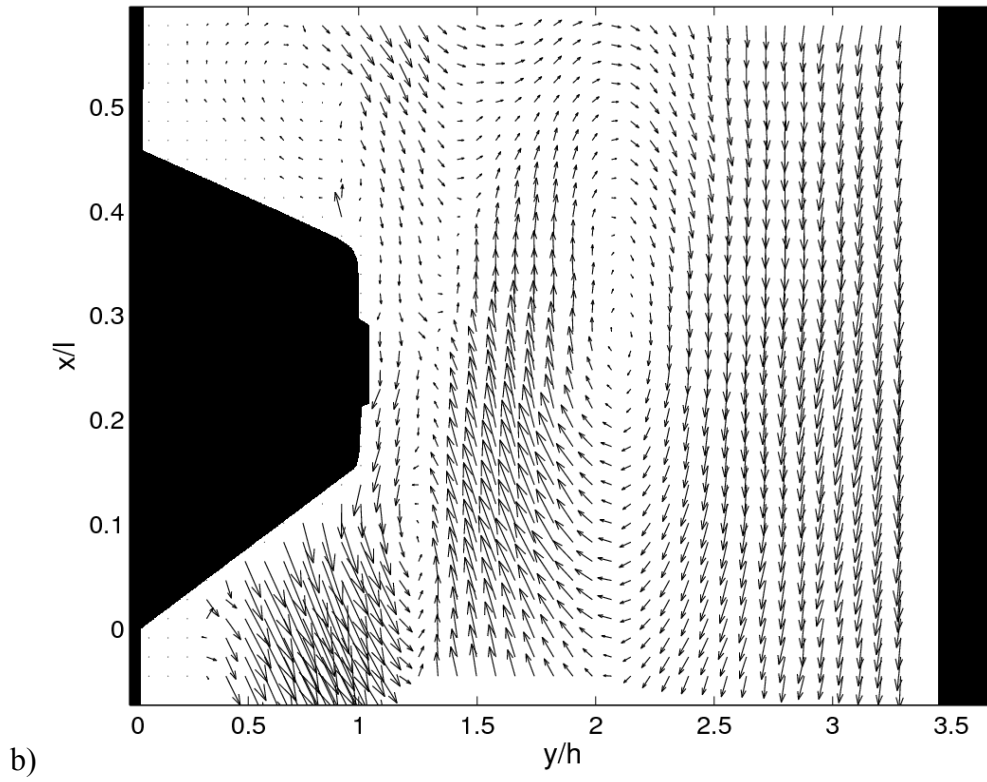
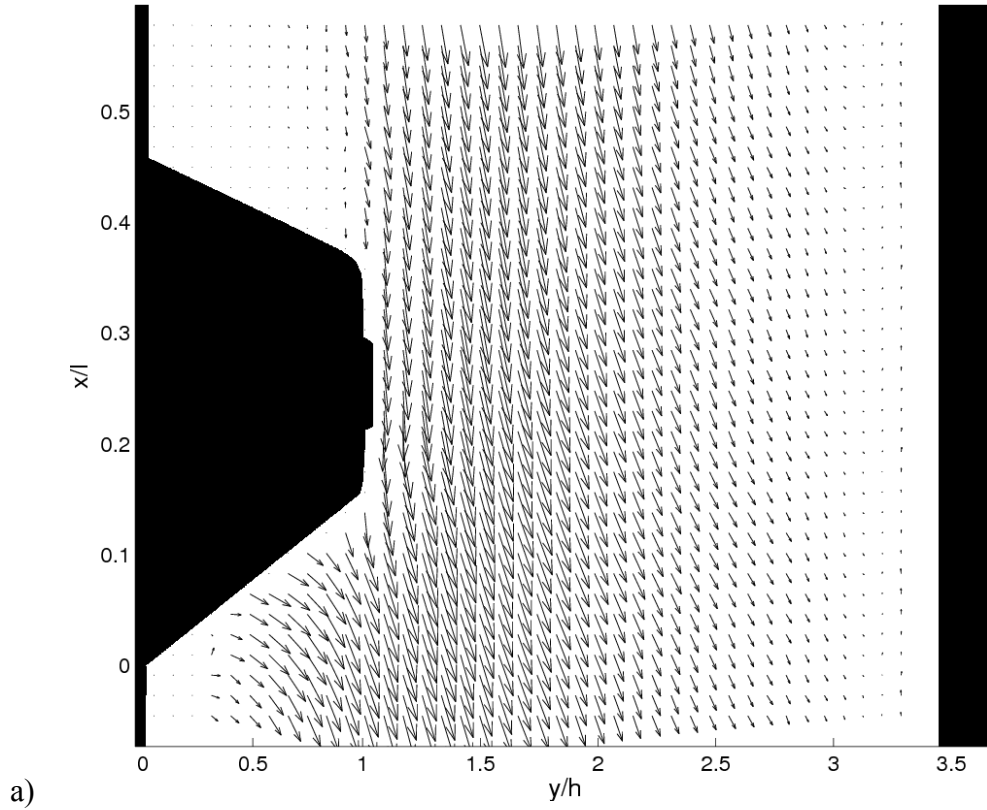
- 4-2 a) Turbulent velocity vector field of frame 47 at the crest in the middle of the channel ($X/H = 0.57$) at half resolution to clearly visualize the directions of the vectors at higher quality;
- b) Reconstructed POD energy vector field up to mode 47 at the crest in the middle of the channel ($X/H = 0.57$) at half resolution to clearly visualize the directions of the vectors at higher quality.

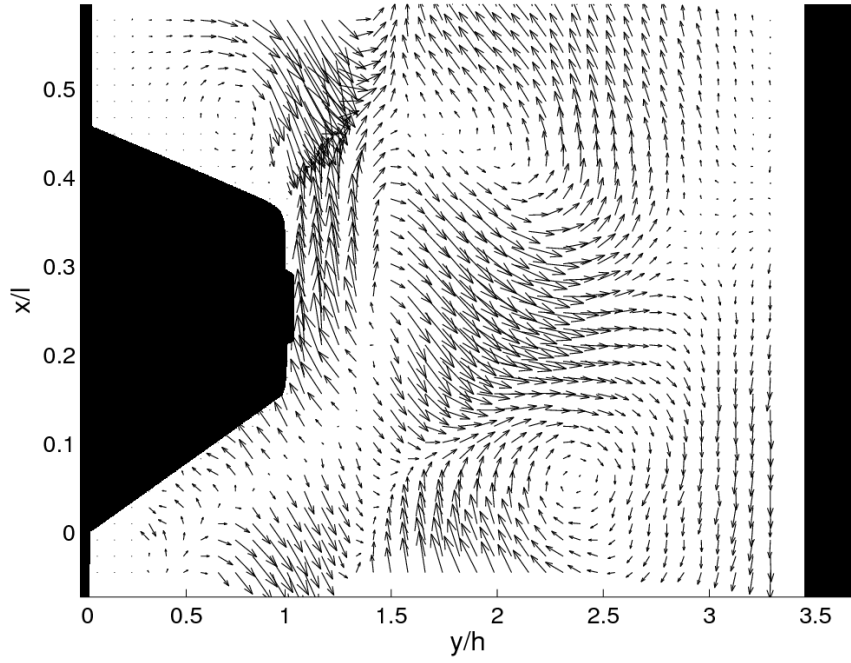
Figure 4-3



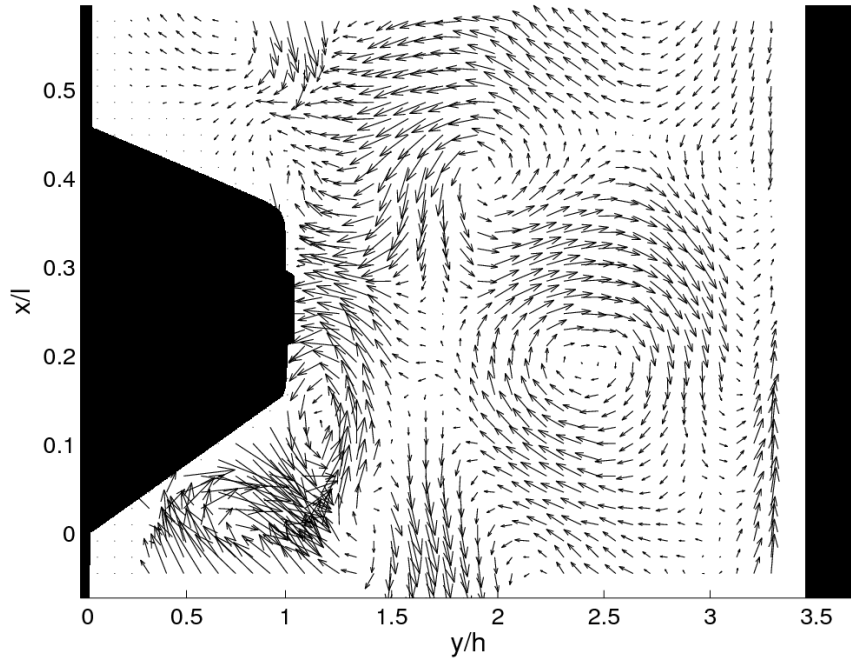
4-3 POD fractional energy (λ_n/E) distribution across all modes for the lowest flow rate, unheated (Green ▲); highest flow rate, unheated (Black ●); highest flow rate, heated (Blue ●); and lowest flow rate, heated (Red ▲) cases.

Figure 4-4

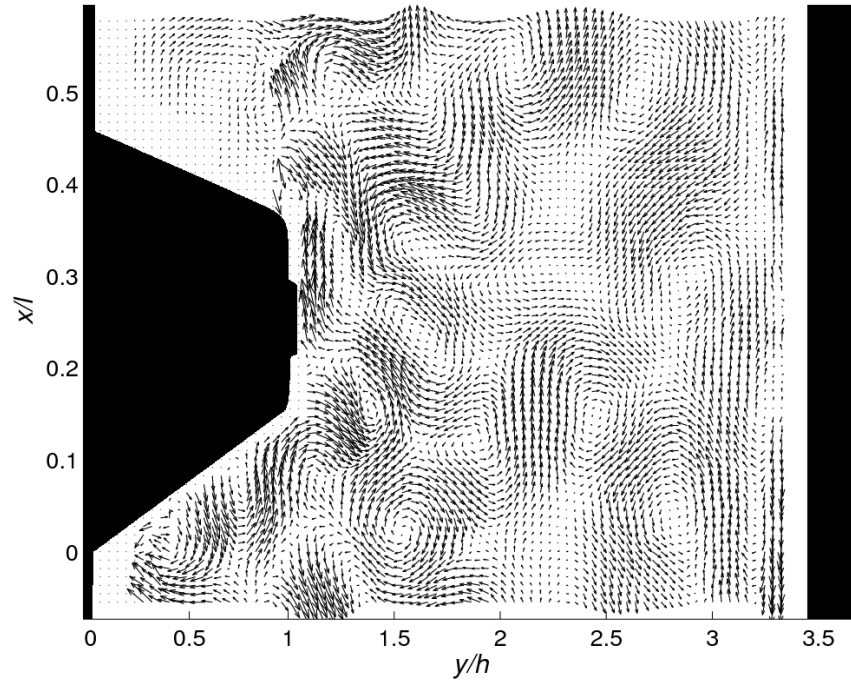




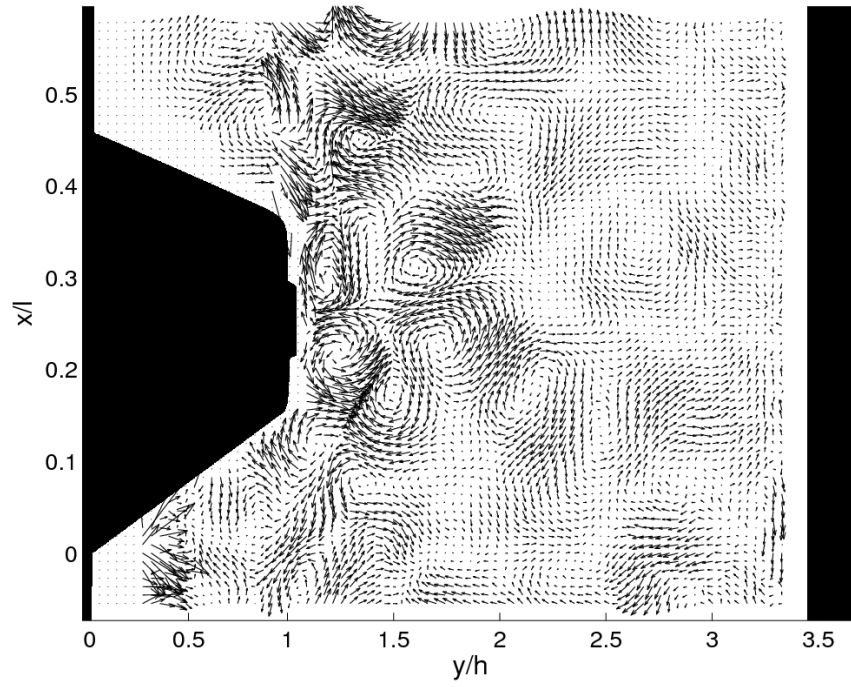
c)



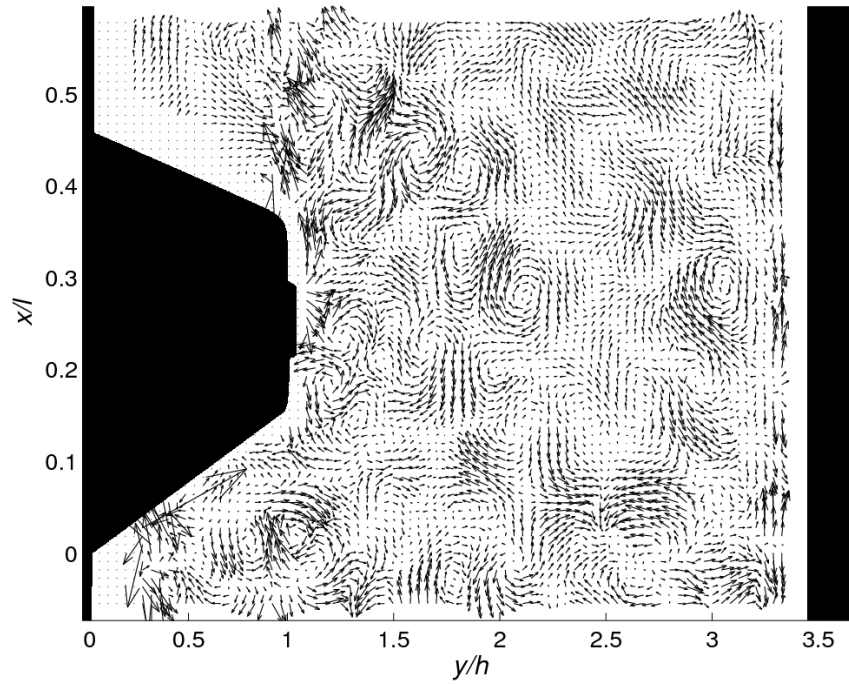
d)



e)

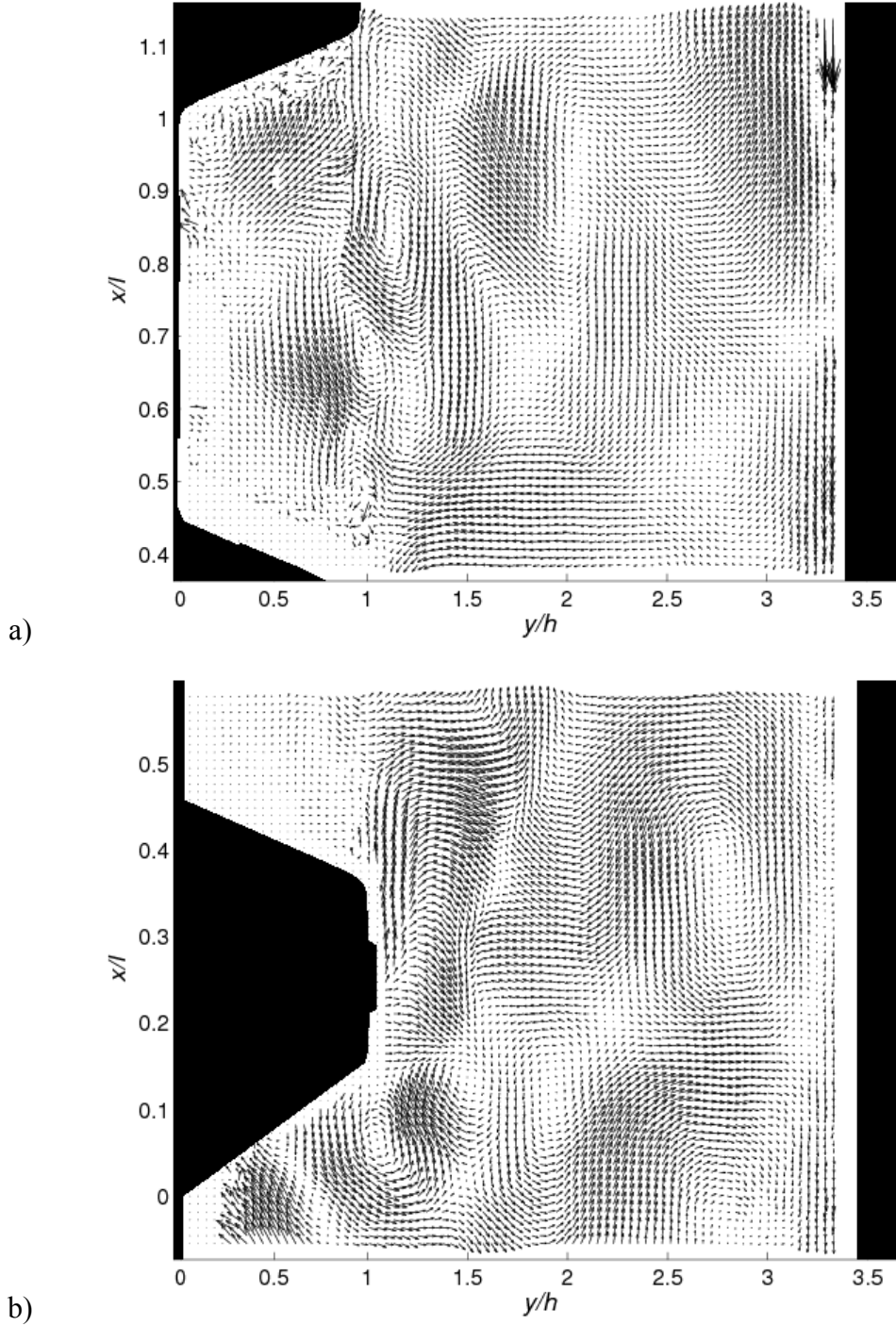


f)



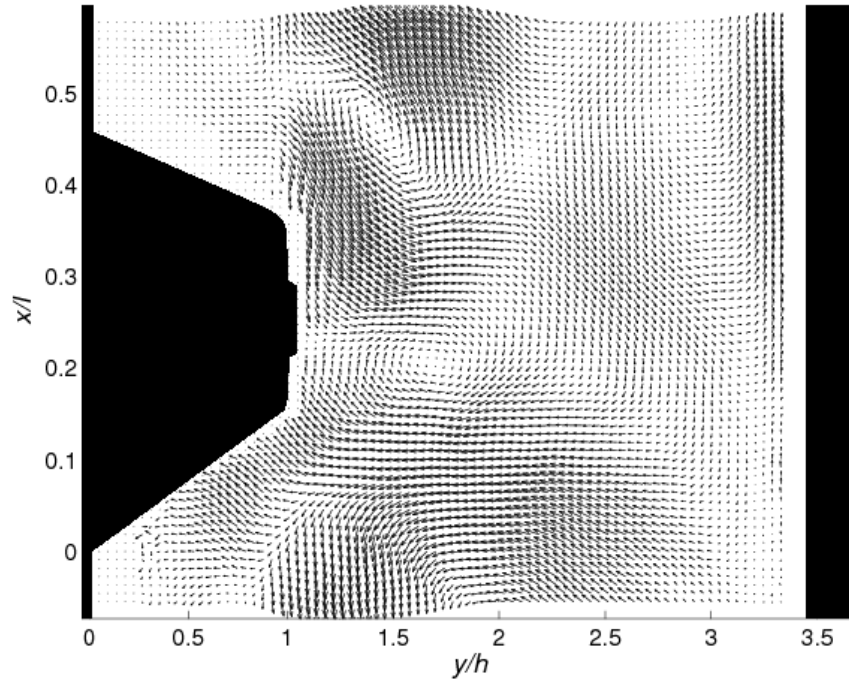
4-4 POD crest turbulent flow energy vector fields at the middle of the channel ($X/H = 0.57$) for the highest flow rate at a) mode 1, half vector resolution; b) mode 5, half vector resolution c) mode 10, half vector resolution; d) mode 20, half vector resolution, e) mode 50, full vector resolution; f) mode 80, full vector resolution; g) mode 150, full vector resolution.

Figure 4-5

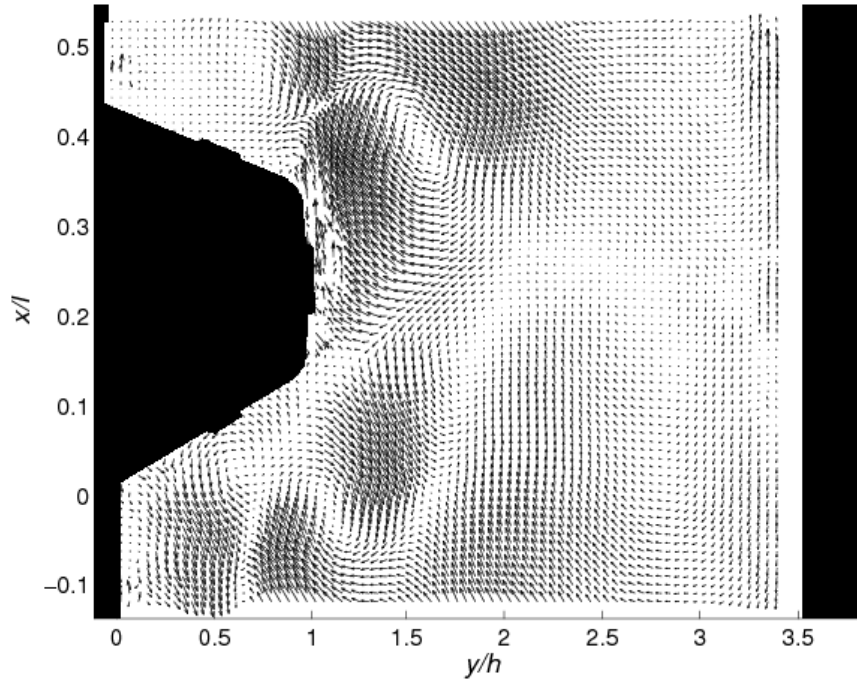


4-5 POD turbulent flow energy vector fields at the middle of the channel ($X/H = 0.57$) for the highest flow rate at mode 25 using full vector resolution in the a) trough section; b) crest section.

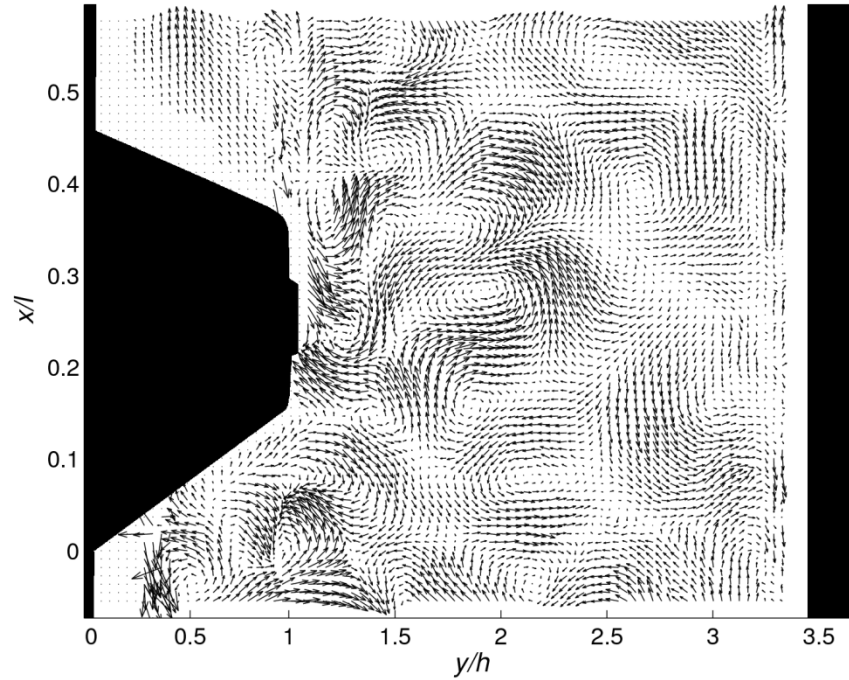
Figure 4-6



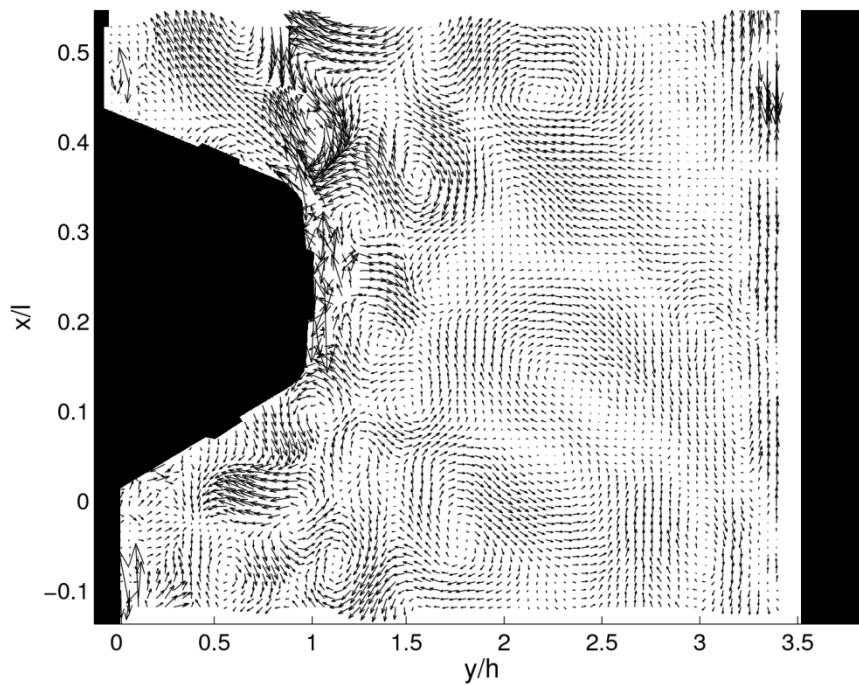
a)



b)



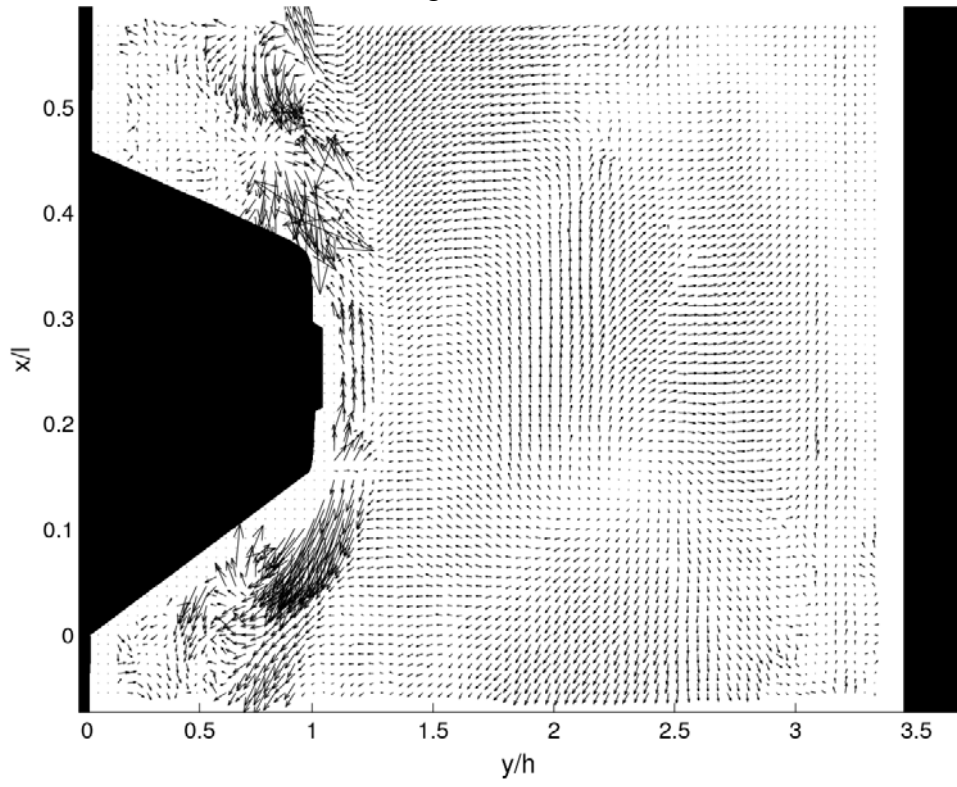
c)



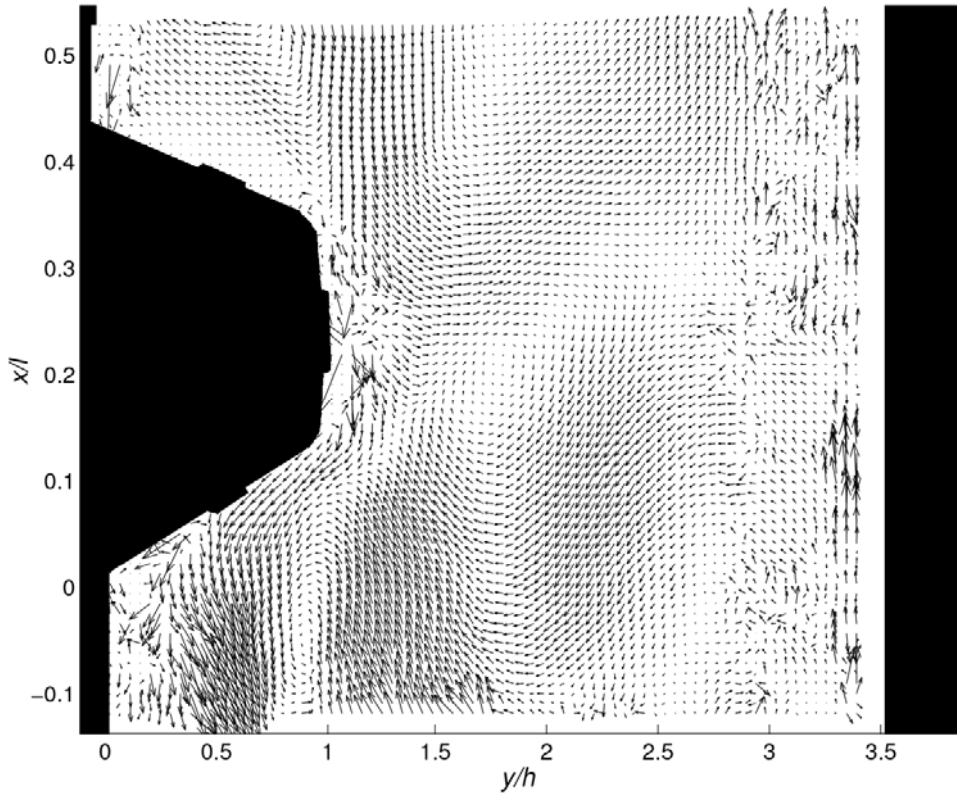
d)

4-6 POD turbulent flow energy vector fields comparing heat and no heat at the middle of the channel ($X/H = 0.57$) at the highest flow rate; a) POD mode 12 for the unheated condition; b) POD mode 12 for the heated condition; c) POD mode 70 for the unheated condition; d) POD mode 70 for the heated condition.

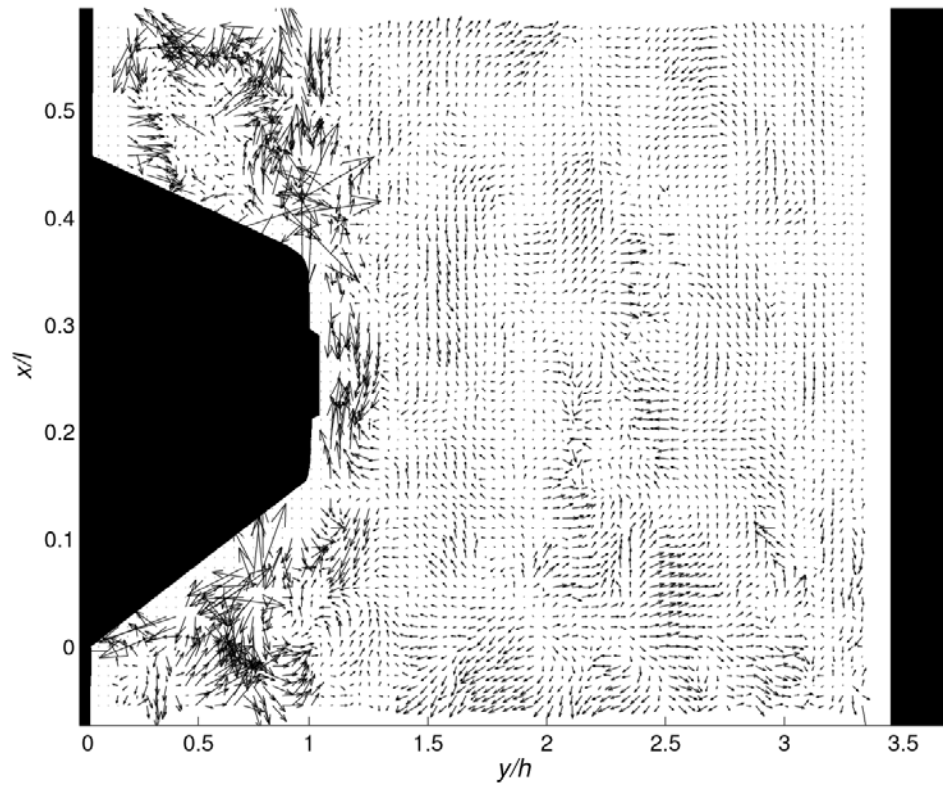
Figure 4-7



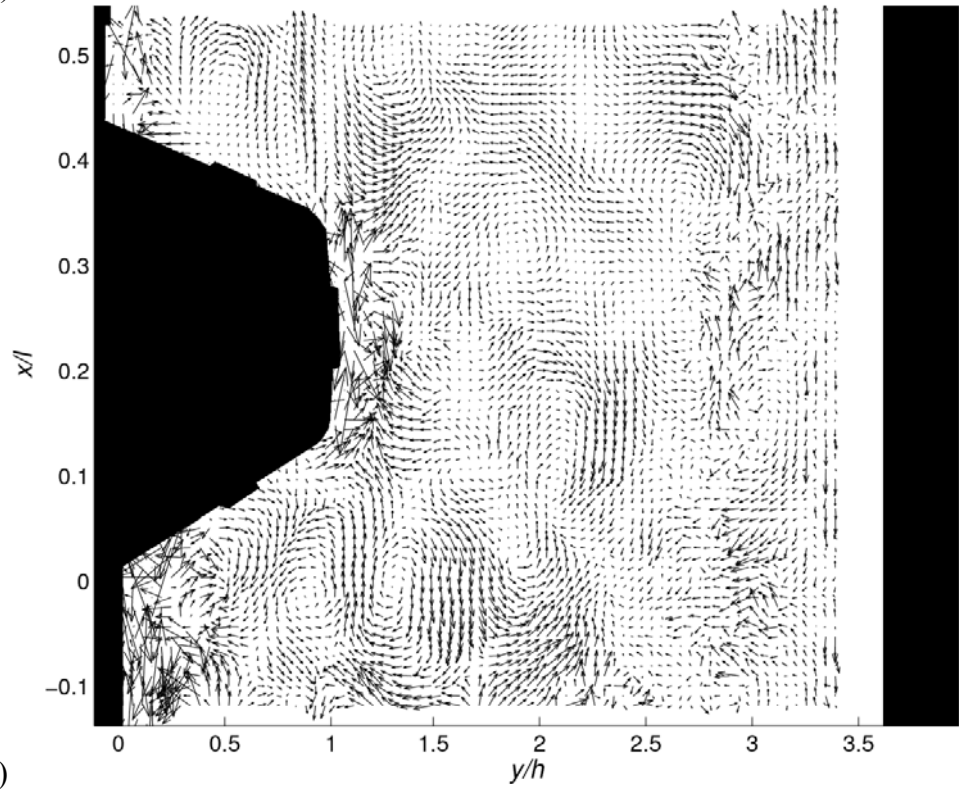
a)



b)



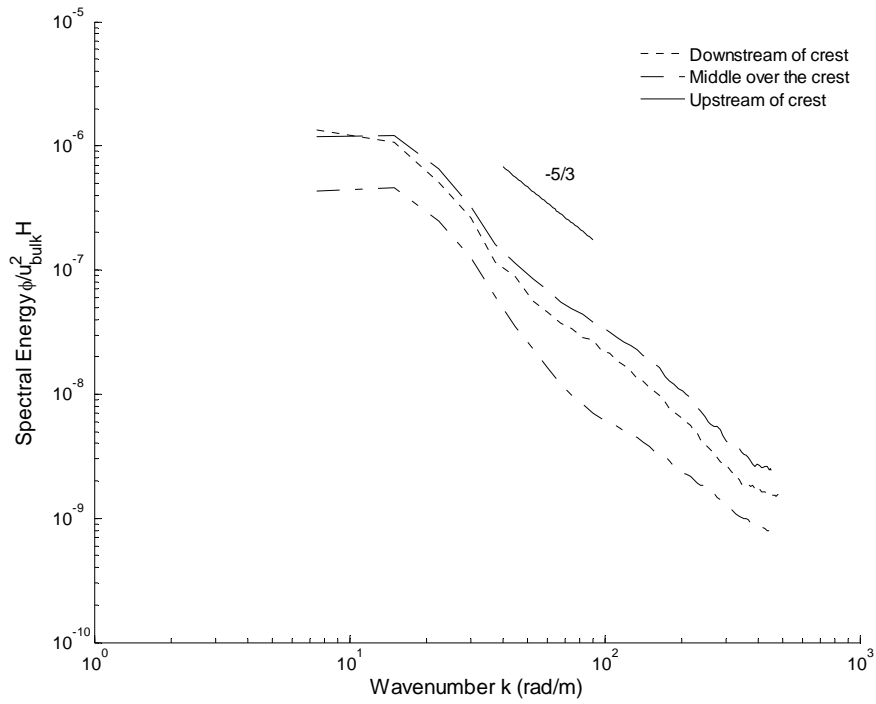
c)



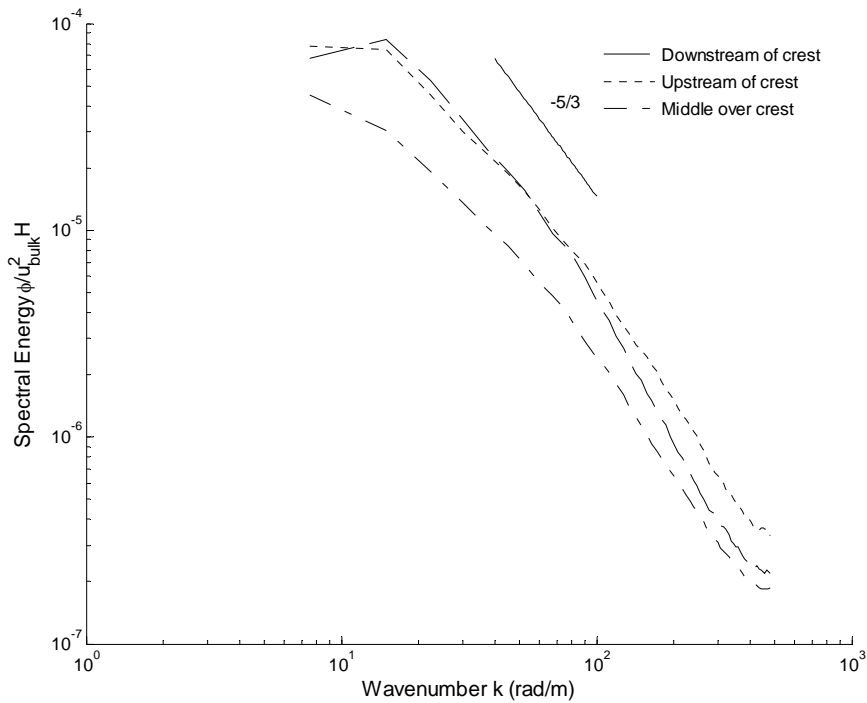
d)

4-7 POD turbulent flow energy vector fields comparing heat and no heat at the middle of the channel ($X/H = 0.57$) at the lowest flow rate; a) mode 15, unheated; b) mode 15, heated; c) mode 78, unheated; d) mode 78, heated.

Figure 4-8



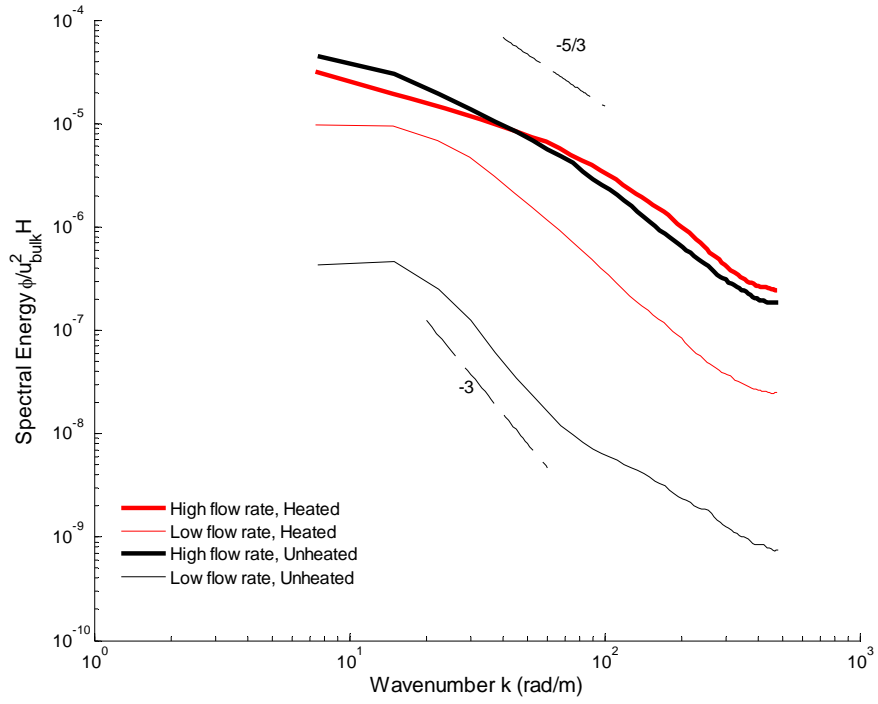
a)



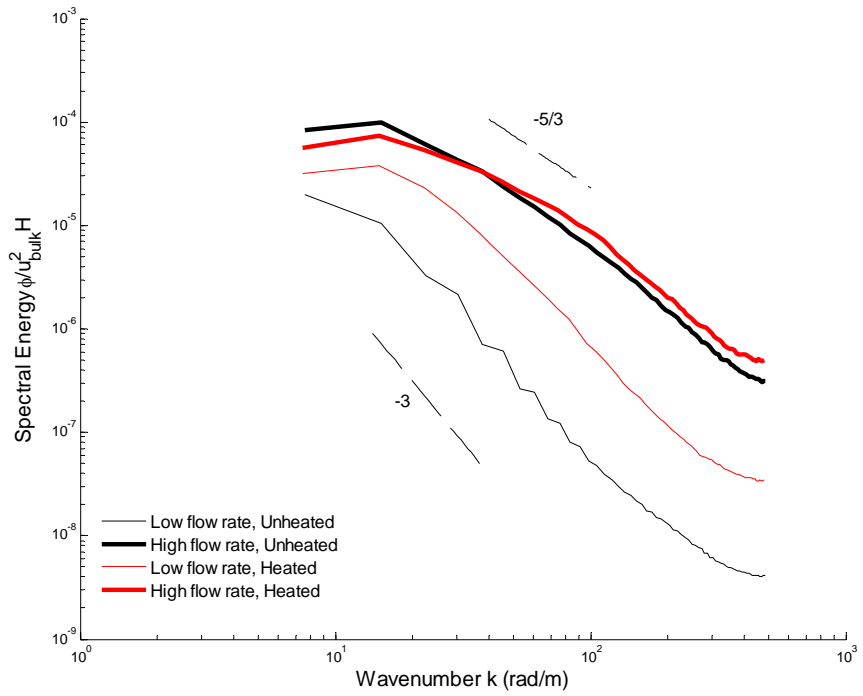
b)

4-8 Wave number spectrum plots for the development of energy across a waveform located in the middle of the channel ($X/H = 0.57$) over the crest for the unheated condition a) at the lowest flow rate; b) at the highest flow rate.

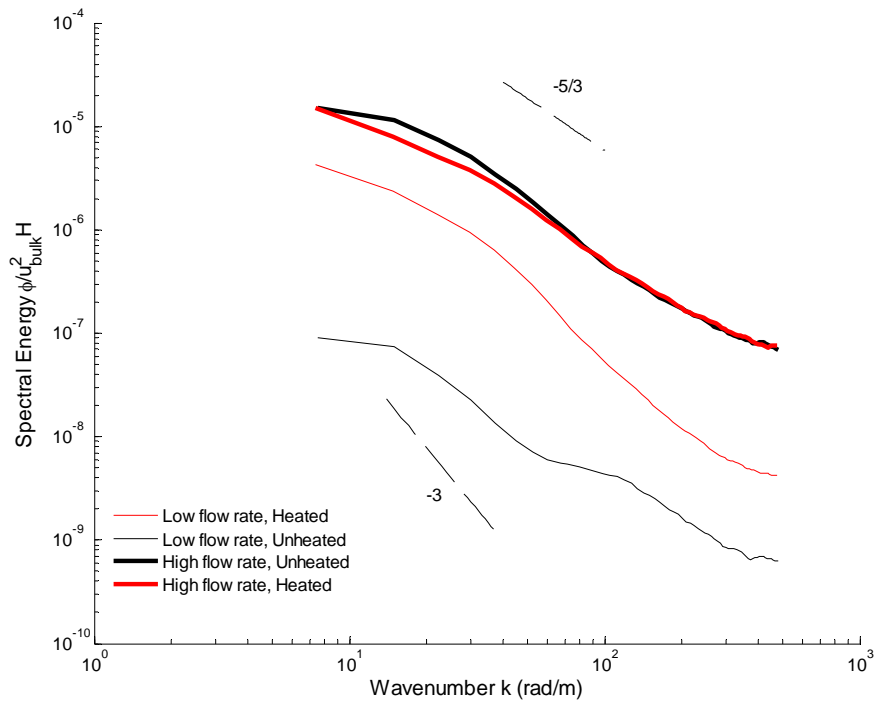
Figure 4-9



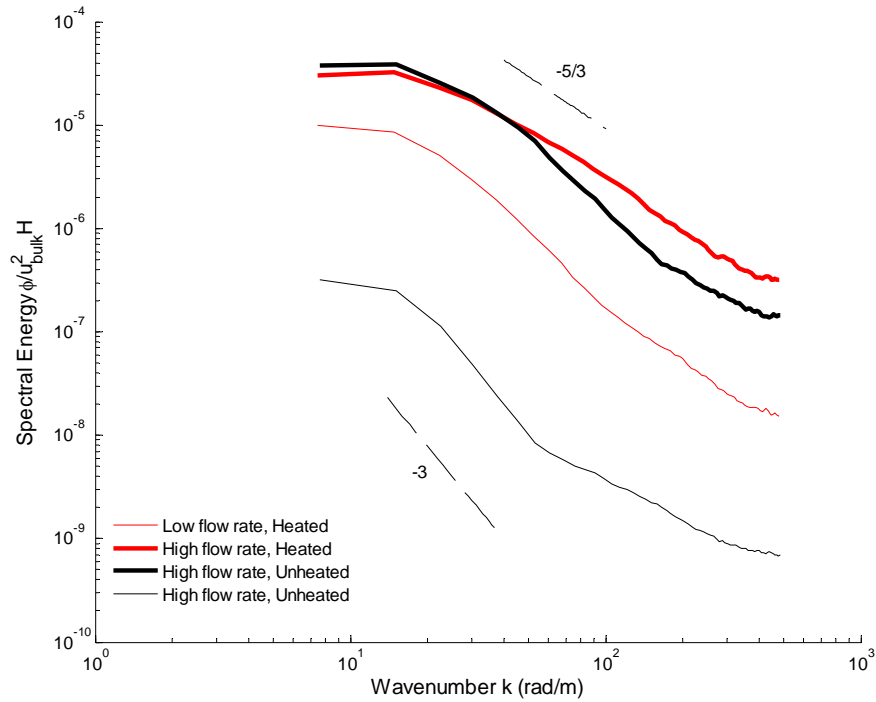
a)



b)



c)



d)

4-9 Wave number spectrum plots comparing the energy transfer located in the middle of the channel ($X/H = 0.57$) for the low and high flow rates at both heated and unheated conditions; a) streamwise energies located over the crest section; b) streamwise energies

over the trough section; c) cross-stream energies located over the crest section; d) cross-stream energies located over the trough section

Chapter 5

Conclusions

Results are given from an experimental study conducted to investigate the air flow behaviour in a vertical channel bounded by a transpired air collector corrugated surface and a plane construction wall. PIV measurements obtained two dimensional velocity fields at three channel positions and five Reynolds numbers. The flow rates considered included the classical range of laminar, transition, and turbulent flow regimes. The results were then compared for further experiments on the channel under different heating conditions. Mean and turbulent velocities as well as Reynolds stresses and the turbulent energy production were computed. Both the heated and unheated flows were further investigated using POD and wavenumber spectrum analyses in order to describe the small-scale interactions of turbulent structures within the corrugation channel.

5.1 Discussion Summary, and Conclusion

The first set of results on the unheated flow over the corrugation waveform show that the geometry substantially modified both the mean and turbulent flow structure across the channel. The presence of the corrugation generated turbulence at all studied flow rates, including the lowest flow rates that would be considered laminar flow over a plane wall. The bulk flow moving through the core of the channel would form a separation layer off of each waveform crest, which would then expand into the corrugation trough and bulk flow. Instantaneous velocity fields demonstrated that the shear layer at the boundary of the bulk and separated flows oscillates in time and influences the size and strength of separation vortices. The rate and

amplitude of the shear layer oscillations increased with the Reynolds number resulting in a stronger bulk and separated flow interaction. Turbulence would then extend further into the bulk flow. The turbulent flow contained bursting flow originating from the trough moving into the bulk flow, as well as sweeping flow from the bulk region. There was weak mean flow in the separation zone in the waveform troughs and relatively uniform mean flow in the bulk region. The combination of the trough flow with the bulk flow created a shear layer and the interaction produced rolling vortices. There was also vortex shedding off each crest. The interactions of these flows created complex three-dimensional structures that moved into the core of the channel. The mean velocity gradients near the corrugation wave height were small, and almost negligible in the bulk region. This implies there was a strong diffusion of the shear. It was found that the mechanism of shear generation at the corrugation wave was almost independent of the flow rate. All turbulent properties were enhanced at approximately one wave height within the channel region $1 < y/h < 1.5$. However, the relative enhancement of turbulence was greater in the trough regions as compared to those at one wave height. The profiles of the Reynolds stress indicated a significant momentum transfer from the corrugation wall by the turbulent velocity field into the bulk flow. The results demonstrated that the turbulence produced by the corrugation waveform dominated the entire channel.

The comparison of the flow behaviour at different positions along the channel length showed that the flow was generally periodic with regards to the waveform. This, however, excludes the bottom measurement position, which was close to the inlet of the channel and discrepancies were attributed to the inlet effects creating stronger three dimensional effects.

As the flow rate increased, the magnitudes of the turbulent properties increased, however the relative enhancement was largest for the lowest flow rate. Although the Reynolds number for the lowest flow rate would typically produce a laminar flow in a flat wall channel, the corrugation waveform was seen to induce strong instabilities in the flow that led to the transformation into turbulence.

With the addition of the radiation heat flux, in general the mean and turbulent velocities, as compared to the unheated flow, were enhanced. As the flow rate increased the structure and magnitudes of the mean and turbulent properties shifted towards those observed in the unheated channel flow, since forced convection was becoming increasingly dominant. Conversely, at the lowest flow rate, the effects of heating were greatest since flow was primarily buoyancy driven. The buoyancy induced instabilities were large at this flow rate thus the relative enhancement of mean and turbulent properties were greatest compared to the unheated flow. The influence of heating on the lowest flow rate also affected the structure close to the corrugation waveform, in particular in the trough. The low velocities in this section were responsible for the higher trough surface temperatures, and it also suggests that turbulence enhancement was primarily generated from buoyancy. Thermal plumes were generated at this flow rate from both walls, which locally increased the mean velocity.

The underlying structures and their interactions at smaller scales were resolved for the highest and lowest flow rate at both high heating and no heating conditions. For all flow rates and heating conditions, the turbulent flow energy was generated by the corrugation and transported into the channel core that fed into the larger scaled structures. At the lowest flow rate, the heated wall increased the total turbulent energy and its distribution at all modes excluding the first. The unheated flow at this flow rate was found to have a very large percentage of its total energy

within the first mode and largest structure because of high dissipation rates produced by viscosity. Consequently, the turbulent flow energy at the lowest flow rate was weaker and more evenly distributed for the unheated condition at a given mode. The heated flow at the lowest flow rate was primarily buoyancy driven and thermal plumes generated strong energies close to the waveform. These energies assisted in maintaining structures at higher modes. Inertia induced turbulence created by the waveform was diminished by these buoyancy forces resulting in a larger energy transfer rate. When comparing the mean and turbulent profiles of the heated and unheated flows at highest flow rate, the effect of heating was not always prominent. The POD and spectra analyses showed that the heating influences these flows at higher modes. Although the energy strength and distribution were very comparable at low modes, heating influences were apparent at high modes and produced larger energies in smaller scaled vortices. In general, heating produced additional structures, structures of higher strength, or maintain structures within the flow over a corrugated waveform at both low and high flow rates. The results contribute to the explanation of the turbulent velocity and Reynolds stress profile trends within the corrugated channel at high and low flow rates.

There was radiation heat transfer from the heated waveform to the construction wall that not only increased the construction wall temperature but also contributed approximately 15-25% of the total heat gained by the air. Collector efficiencies were as high as 70%, which were attained due to the corrugation surface geometry, which not only increased turbulence and mixing, but also provided a larger heat transfer surface area.

The influence of the wall heating on the flow structure was heavily dependent on the airflow rate. The corrugation waveform generates turbulence even at relatively low flow rates, which implies an effectively heat transfer at low flow rates compared to those over a flat wall. It can be

concluded that the strong production of turbulence by the corrugation waveform and its effective diffusion throughout the channel would significantly enhance the heat transfer from the corrugation wall and hence would enhance the thermal performance of a transpired air collector.

5.2 Significance of Findings

The fundamental physics describe the interactions of mean and turbulent flow structures that constitute the overall heat transfer to the air. The significance of broad conclusions from experimental results and how they influence considerations for the solar air collector system can be summarized with the following:

1. In heat transfer systems, it is desirable to have turbulence, because turbulence means increased mixing. With more mixing, thermal boundary layers decrease in thickness or are broken up and heat is transferred easier between a surface and fluid and across the fluid.
2. There is a large amount of turbulence being generated due to the corrugation waveform. This means that where there would be a thermal boundary layer close to the heated corrugated solar collector, the turbulence is breaking up the thermal boundary layer and increasing mixing, resulting in larger heat transfer from the collector to the air.
3. There is enhanced turbulence throughout the entire channel, thus the turbulence generated at the shear layer moves into the bulk flow. This indicated that the heat gained by the air close to the corrugation is easily transported into the bulk flow such that the energy gain is well distributed.
4. The addition of heat to the flow increased the overall flow energy. These energies can be transferred into turbulent structures of scales smaller than those experienced in an

unheated flow. These structures can then be sustained longer rather than dissipating out quickly, which means that turbulence throughout the channel can be maintained longer.

5. Although higher flow rates are desirable to maximize thermal efficiency, enhanced turbulence existed for all examined flow rates, thus the geometry is responsible for mixing rather than the flow rate.

5.3 Future Recommendations

The current experiments presented the first sets of data on the air flow behaviour and thermal performance of a cross-corrugated transpired air collector. The system was designed to be modular and there is a large potential for more measurements to be taken for different configurations as well as for comparing different solar collectors used in application. Since there are many different types of solar collectors and multiple methods for their installation, each of these can be studied using the current experimental frame, such that standards can be created to maximize the performance of each setup. Variables that can be changed are the channel depth, the type (flat plate, different types of corrugation, etc...) and material of solar collector, the orientation of the solar collector, and the angle of the entire solar system with horizontal. Each will modify the air flow within the channel either do to geometry change or by having an effect on heat transfer.

There is also discussion on conducting studies on the air behaviour in a solar air collector with the channel inlet sealed, such that the primary intake of the flow is through the perforation holes. Although this setup is expected to have larger pressure drops for the same flow rate as an open inlet, the effects on turbulence and heat transfer may be desirable to obtain higher air

temperatures. Additionally, there can be enough information obtained to estimate the local heat transfer coefficients along the inside surface of the solar collector.

Although there is a great potential for the wide spread application and use of solar air collectors, standards for their development and installation are still only implemented by convention rather than optimization. Further studies on the available collectors and their configurations to examine not only the thermal performance but also the air flow characteristics, will lead to an improved understanding on the proper installation considerations to optimize heat transfer. This will eventually result in the increased manufacturing and implementation of solar collectors to reduce the overall world energy demand.

APPENDIX 1: PIV Error Calculation

The total error in Particle Image Velocimetry can be estimated as the sum of the errors calculated for the particle diameter, seeding density, out of plane motion, velocity gradient, dynamic range, peak locking, and Adaptive Gaussian Window interpolation [1]. The corresponding errors in this study were calculated based on figures 5 a–f in Cowen and Monismith [1]. These figures were created based on a gradient of $0.03 \text{ pixels/pixel}$, thus linear interpolation was used to correct for the different in error for the gradients in this report. The same tracer particles were used for all experiments with approximately equal size of field-of-views and same range of velocities as all measurement positions. Thus the maximum error across all runs was computed. The total error is the sum of the mean and the root mean square (rms) errors for each of the above error sources.

The PIV velocity error was calculated based on the largest average velocity gradient across both velocity directions. This was found to be $0.0503 \text{ pixels/pixel}$ in the streamwise direction at the highest flow rate in the middle measurement position of the channel for the unheated flow. The following procedure was carried out using the largest velocity gradient for the unheated flow condition.

The gradient error was calculated from figure 5e in Cowen and Monismith [1] by summing the differences in error between the $0.03 \text{ pixels/pixel}$ gradient used in the figure and this study's velocity gradient of $0.0503 \text{ pixels/pixel}$ for both the mean and rms values.

$$(0.14 - 0.08) + ((-0.05) - (-0.03)) = 0.04 \text{ pixels}$$

The average size of the particle diameter was $1\mu\text{m}$. Since this tracer particle is smaller than the size of one pixel, and the resolution of the image cannot capture particles smaller than one pixel, the particle size was simply set to 1 pixel. The associated error from figure 5a [1] is:

$$(-0.03) + 0.095 = 0.065 \text{ pixels}$$

Figure 13 in Prasad et al. [2] was used to determine the error of peak locking. Although particle diameter error was estimated to be 40 percent larger than the error associated with a particle of 1 pixel in diameter, the authors used a center of mass cross-correlation procedure, which is susceptible to peak locking. This report uses the three point Gaussian estimation, which has a reduced peak locking error. Instead, the additional error in particle diameter was estimated to be 30 percent. Thus the final error for particle diameter is:

$$0.065 \times 1.3 = 0.0845 \text{ pixels}$$

And the total associated error for both velocity gradients and particle diameter is:

$$0.0845 + 0.04 = 0.1245 \text{ pixels}$$

The error attributed to out of plane motion was calculated from the total displacement of vectors in the transverse direction summing the mean and standard deviation.

$$\Delta z = \overline{\Delta z} + \sigma_{\Delta z} = 1.16 \text{ pixels}$$

Using the spatial resolution for this flow case, 1.16 pixels correspond to 0.075 mm . This displacement was considered negligible since the thickness of the laser sheet was less than 2 mm .

Thus there was no additional error for out of plane motion.

The Adaptive Gaussian Window interpolation error was calculated from figure 5f in Cowen and Monismith [1], which was 0.08 pixels for 1500 vector fields and brings the total error to:

$$0.1245 + 0.08 = 0.2045 \text{ pixels}$$

The largest velocity gradient produces equal errors in both the streamwise and cross stream directions; thus it can be assumed that the total error overall is the square root of the sum of twice the streamwise error component:

$$E_{total} = \sqrt{2E_u^2} = 0.2892 \text{ pixels}$$

This final error is divided by the time between each captured image, 0.009 s, and also divided by the spatial resolution of the image for the corresponding flow rate, 154.0 pixels/cm, to produce a total velocity error of 0.208 cm/s.

The largest error was calculated for the largest instantaneous velocity gradient in the unheated flow was at the highest flow rate. This produced an uncertainty in velocity less than 1% of the average bulk velocity for the same condition. The velocity errors for the other measurement positions and flow rates produce results smaller than this calculation.

References

- [1] E. A. Cowen, S. G. Monismith, A hybrid digital particle tracking velocimetry technique, *Exp. Fluids* 22 (1997) 199.
- [2] A. K. Prasad, R. J. Adrian, C.C. Landreth, and P. W. Offutt, Effect of resolution on the speed and accuracy of particle image velocimetry interrogation, *Exp. Fluids* 13 (1992) 105.

Curriculum Vitae

David Greig

dgreig4@gmail.com

Post-secondary Education and Degrees:

The University of Western Ontario
London, Ontario, Canada
2005-2009 B.E.Sc

The University of Western Ontario
London, Ontario, Canada
2009-present M.E.Sc

Honours and Awards:

Honours Student
The University of Western Ontario
2005-2006, 2006-2007, 2007-2008.

Related Work Experience

Engineering Faculty Orientation Week Leader
The University of Western Ontario
2006-2008

Created activities and was involved with the welcoming and guiding of first year students entering University.

Research Assistant (USRA)
The University of Western Ontario
2008
Tested a new sensor, analysed results, and presented conclusions

Teaching Assistant
The University of Western Ontario
2009-2011

Developed and maintained the laboratory component to the mechanical engineering second year course MME2285 Selected Experiments.

Publications:

D. Greig, K. Siddiqui, and P. Karava, An experimental investigation of the flow structure over a corrugated waveform in a transpired air collector, Int. J. Heat and Fluid Flow (2012), In review.

D. Greig, K. Siddiqui, and P. Karava, The influence of surface heating on the flow dynamics within a transpired air collector, Int. J. Heat and Mass Transfer (2012), In review.